Molecular Dynamics simulations of strongly correlated mesoscopic and macroscopic Coulomb systems

Dissertation

zur Erlangung des Doktorgrades

der Mathematisch-Naturwissenschaftlichen Fakultät

der Christian-Albrechts-Universität zu Kiel

vorgelegt von

Volodymyr Golubnychiy

Kiel

2004

Referenten:_____Prof. Dr. Michael Bonitz_____

Koreferenten:_____Prof. Dr. Holger Fehske_____

Tag der mündlichen Prüfung:____13 July 2004_____

Zum Druck genehmigt: Kiel, ____14 July 2004_____

Der Dekan:_____Prof. Dr. Jürgen Grotemeyer_____

Contents

Chapter 1

Introduction

Among all physical objects, observed in nature, almost 90% exists in ionized form. Examples include relatively cold and dilute interspace gas and also very hot and extremely dense star and planet cores. On the other hand, many modern experiments with short laser or ion beams also create dense plasmas. Matter in such conditions consist of many particles, which strongly interact with each other.

In these systems the structure of matter differs from states of nearly independent elementary particles, which are often used in theories. The matter is subject to much disturbance from other matter and fields. If there are only stationary processes or the external excitation is small enough, we have an equilibrium system or a system in linear response regime. For example, kinetic theory or linear response theory are applicable for weakly correlated systems. However, in case of strongly correlated quantum systems, these methods fail or become inefficient. This phase region contains all collective phenomena and correlation effects. This is one of the interesting class of objects: many particles systems with strong correlations.

Here, it is often advantageous to use computer simulation methods.[1] Computer simulations in physic science pursue a two-fold goal. The first is to understand (and, as a long-term goal, even reliably predict) the properties of the real matter based on the details of physical structure. Secondly, there are still a number of unsolved questions (for example, the influence of correlation on collision effects and vice versa) which are not related to specific materials, but rather of a quite general and fundamental nature, and whose solution is, to our minds,

[1] We use the notation "computer simulation" for particle-based simulation in contrast to statistical theory simulation based on probability density distributions.

indispensable for real progress in our ability to predict the properties of these many particles strongly correlated systems.

In general, there are two types of computer simulation algorithms, Molecular Dynamics (MD), based on the solution of Newton's equations of motion, and Monte Carlo (MC), based on a Markov process in configuration space. There is no general answer to the question which method is "better"; to a large extent, this depends on the system under consideration, and, even more so, on the scientific question which one would like to answer.

As the name implies, molecular dynamics enable us to obtain the dynamic properties of the system. Unlike MC simulation, MD is totally deterministic and chance plays no role. Another important distinction between MC and MD methods is that MD uses interparticle forces to evolve the system in time whereas MC simulation primarily involves the calculation of the changes in total system energy to compute the equilibrium or ground state properties. Today both simulation techniques are used widely by researchers in many disciplines. The choice between the two alternatives depends on the properties being investigated.

History of computer simulation methods goes back to the middle of the last century, when most scientific efforts in physics were stimulated by military goals to increase the power of the nuclear weapons or creation of a relative compact nuclear source of energy[2] and the necessity of deeper understanding of processes, taking place in nuclear reactions.

There is evidence, that the idea of using computer devices for solving problems in Statistical Mechanics goes back to Enrico Fermi. Here is a citation from the book "From x-rays to Quarks" of Serge' [2]: "... I know that Fermi had invented, but of course not named, the present Monte Carlo method when he was studying the moderation of neutrons in Rome. He did not publish anything on the subject, but he used the method to solve many problems with whatever calculation facilities he had, chiefly a small mechanical adding machine." The developing Monte Carlo (MC) scheme itself was catalyzed by the war efforts during that time when Von Neumann, Ulam and Metropolis employed stochastic numerical methods to neutron diffusion problems in Los Alamos. The pioneer paper was published in 1953 by Metropolis et al. [3], which treated computations of a hard-sphere liquid via the Metropolis Monte Carlo method. B.J. Alder and T.E. Wainwright made

[2]for example, Aircraft Nuclear Propulsion development program (ANP), started in 1951 [1]

the next major step, when they published the first results obtained by molecular dynamics, also on a hard-sphere liquid [4, 5]. Then W.W. Wood and F.R. Parker introduced continuous potentials, treated a Lennard-Jones fluid with MC [6]. The next major advance was in 1964, when Rahman carried out the first simulation using a realistic potential for liquid argon [7]. The first molecular dynamics simulation of a realistic system was done by Rahman and Stillinger in their simulation of liquid water in 1974 [8].

Today molecular dynamic simulation has evolved into one of the most powerful and most frequently used methods applied to investigate thermodynamics and a lot of time dependent processes. Very good reviews can be found in Refs. [9–12]. The method is applied in many fields of science and to a large variety of objects, beginning from macrosystems in astronomy (for example simulation of the dynamics of the collision and merger of two galaxies [13], evolution of a stellar disk in a satellite merger [14]), microsystems in chemistry (polymers [15], solution of salts [16] and biochemistry (study protein stability, conformational changes, protein folding, drug design by program CHARMM [17] (Chemistry at HARvard Molecular Mechanics)) up to strongly coupled and heated matter in nuclear physics.

The first applications of computer simulation, and molecular dynamic in particular, were highly secret, but now it is used as a normal and sometimes standard investigation scheme. The simulation itself is the modern realization of an old, essentially old-fashioned idea in science; namely, the behavior of a system can be computed if we have for the system's parts, a set of initial conditions plus all forces of interaction. From the time of Newton to the present day, this deterministic mechanical interpretation of Nature has dominated science. Nevertheless, such a simple model of the physical world can be very successfully applied to systems like atoms and molecules, where concept and presentment of the macroworld are changing to new level - the level of micro and nano scales. Of course this approximation can be used only under some restrictions: one can always keep in mind that we are using a *classical* approach to *quantum* objects.

Our main aim was time-dependent dynamic properties of the two and three-dimensional nano systems and macroscopic plasma. For this reason molecular dynamic strategy is required. MD is now almost one possibility to get dynamic properties. As other methods classical MD has its own limitations:

- we consider point particles;
- particles move on the classical trajectories, obeying Newton's equations of motion;
- there is a collision problem between opposite charged particles in classical cases, because a divergence of Coulomb potential at zero interparticle distance.

It is clear that correct description of system properties will be observed for systems where interparticle distance is bigger than the De Broglie wave length $r_{ij} > \lambda$, $T > T_F$ or $kT > E_B$, where T_F is temperature Fermi, E_B is binding energy.

There are other variants of computer simulations in which limitations on classical MD are trying to overcome. In Wave Packet Molecular Dynamics (WPMD) [19–21] many-particles wave function is presented as a product of one-particle wave functions, which supposed have a Gauss form. So in this way every electron can be described using variation parameters: position, impulse and their complex widths. At first stage all energies and their derivatives are calculated and then one performs a propagation of variation parameters. The propagation can be done by either Monte Carlo or real Molecular Dynamics schemes. Nevertheless, till now only static properties were calculated using WPMD methods.

Car-Parrinello method (CPMD) [22, 23] merges two different fields, density functional theory and Molecular Dynamics. It describes the energy of electrons in the field of protons in Born-Oppenheimer approach using density functional. For simulation of many electron atoms the interaction region divides on the core and the region of valence electrons. The core is represented by pseudo wave functions, constructed in a form simplified for numerical calculation. The ground state configuration is looked for and dynamics are performed. There are drawback that leads to some limitations. The modeled systems are very small compared with classical MD, because of the method scales as $O(N^3)$, N is the number of particles, whereas classical MD scales as $O(N^2)$.

A quantum dynamics in combination with MC proposed in Ref. [24, 30] is a superposition Path Integral MC [25,26] which uses Wigner presentation of density matrix to calculate a many-dimensional density matrix of the canonical ensemble, and classical dynamics with jumps in impulse space.

All of these techniques are very time-consuming, so at present they are limited by computer calculation power and use in present paper semiclassical MD (SCMD) is used to get dynamic properties which were the main focus of our work. SCMD when used in our work tries to involve some quantum effect by using extension of micropotential with quantum diffraction effects. Spin effects are also included in the description as well as formation of the bound states.

The present work is divided by three parts, which differ in the type of simulated systems. In our work we deal with such essential quantum systems as the one component electron gas, hot ionized hydrogen plasma matter or electrons confined in traps. Particles in all these systems have some common properties - they are strongly correlated quantum systems. Under the term 'correlated' we imply that the mean potential energy and the mean kinetic energy are of the same order of magnitude. Under such conditions the interparticle interaction plays a crucial role and determines many system properties.

The first part is devoted to studying a finite number of ions or electrons in traps. These traps are created, for example, by imposing an artificial confining electrical potential. Examples are radio-frequency traps [31, 32] for ions, electrons, charged dust particles, etc. Such systems form atom-like shell structures, which can be observed in real experiments. In our work we have considered a classical mesoscopic two dimensional system consisting of a finite number of electrons which are laterally confined by a parabolic potential and which are held at low temperatures. At the chosen parameters the system is highly correlated and can form, for example, a Wigner(Coulomb) crystal. In contrast to Wigner crystals in an infinite unconfined system here, the system possesses special spatial properties, which strongly depend on the precise number of particles. In particular, it is found that there exists different crystal-like phases. We investigate by MD simulations the orientational melting process on the examples of clusters with N =12, 19 and 20 particles. Different methods for calculation of the intershell angular barriers are developed and compared. The new properties of such clusters give the possibility to construct micro devices, which can be operated by introduction or removal of a single additional particle. We demonstrate the principal possibility of such a device on the example of the singe-electron controlled system with $N = 19$.

In the second part of our work we use Molecular Dynamics simulation to in-

vestigate thermodynamic and dynamic properties of a one-component plasma. The one component electron plasma (OCP) is a simple model of systems with Coulomb-like interparticle interaction; in an OCP we can avoid the electron-ion collision problem and concentrate on the influence of other physical parameters on the properties of the system. Moreover, there are theoretical predictions for OCP systems, which together with simulation provide valuable insights into systems with long-range interparticle potentials. We obtain the density-density correlation functions and structure dynamic factors for several wave vectors. The quantum nature of the particles is incorporated in form of effective quantum potential - the Kelbg potential [27, 28]. To correctly treat the long range character of the Coulomb force, the Ewald summation is applied. Of special interest is the influence of quantum effects on the dispersion of Langmuir waves which is studied by comparison of the results of MD simulation with the Kelbg and pure Coulomb potential, respectively. Finally, an analytical approximation for the Langmuir plasmon dispersion which takes into account correlation and quantum effects is derived. The influence of the coupling parameters, degeneracy parameter and the form of the pair potential on the plasmon dispersion in OCP as well as improved analytical approximation for the dispersion of Langmuir waves is presented.

In the third part, simulations of hydrogen were performed using improved effective two-body potentials for a two-component plasma. The Kelbg potential (used in the second part), capturing the basic quantum diffraction effects is exact in the weak coupling limit. However it fails for strong and moderate coupling. The improved potential is obtained from accurate Path Integral Monte Carlo (PIMC) results for the binary density matrix [29]. We use the improved "quantum potential" which applied also to a plasma with intermediate coupling. Moreover, we use different potentials for the interaction of electrons with opposite and same spin projections. This set of improved potentials is used for simulations of hydrogen beginning from the fully ionized plasma to the region of strong atom formation. With the improved potentials the properties of the partially ionized hydrogen plasma can be studied. Excellent agreement with PIMC results for the total energy is found. Further, pair distributions and plasmon spectra are compared with the OCP model. In addition, the first results for spin-spin density fluctuations are obtained for a nonideal hydrogen plasma.

Chapter 2

Investigation of classical 2D Coulomb clusters

2.1 Physical parameters and problems of interest

In this chapter we will investigate thermodynamic and dynamic properties of small ($N = 5 \dots 20$) two dimensional systems of electrons, confined in a spherically symmetric harmonic potential. In such systems the motion of the particles is restricted in all spatial directions. One such possibility of his restriction is the applying of a confinement potential. The confining potential can be created by external electromagnetic fields. A similar situation can exist in semiconductor multi-layered structures.

During the past few decades considerable attention has been paid to the study of the physical phenomena occurring in mesoscopic systems of charged particles: quantum dots, wires, rings, etc. There is also a new class of investigated objects - exciton bilayers, see Ref. [36]. The interest in these systems has several causes. First, development of microelectronic devices required more detailed investigation and understanding of processes, proceeding on the surface and in near-surface layers of different materials. The main characteristic of such devices - speed of operation, reliability, energy consumption - depends in particular on diffusion processes near surface. So, future progress in microelectronics in many aspects is defined by developing of theoretical insight into the properties of mesoscopic systems.

The second important factor is connected with developing of precise meth-

ods of realization for different microelectronics systems. It has become possible to create with previously unachievable precision thin-layer structures like metal-dielectric-semiconductors, different heterostructures and complicated superlattices. Special new test structures have appeared in research laboratories is giving rise to new experimental results. To these new results belong measurements in quantum dots with a prescribed number of particles [37]. In experiments it is now possible to control the number of particles in such artificial 'atoms' and 'molecules' and investigate the properties depending on adding or removing one particle. In particular, in the paper [37] a strong dependence of chemical potential is dependent on the number of particles in the quantum trap.This was discovered using one-electron capacity spectroscopy. This dependence can be explained by many particle interactions and correlations, which have significant influence on the energy spectrum. Changing the controlled parameters in artificial atoms, like density, particle charge, external potential strength, temperature etc., the experimentalists can control the state of the system and study the system in the classical regime.

Another important reason why there is growing interest in finite systems in the confinement potential is that it is possible to directly observe, for example using an electron microscope, ordered structures, reminiscent atoms - particles are distributed over shells with different symmetry elements relative to the center of the confinement potential. In a real experiment or computer simulation one can investigate the properties of the ground state of an artificial atom 'cluster' - the order of shell filling, the number of particles on every shell in the system (leading to an analogy of the periodic table of Mendeleyev). For example, in Ref. [41] formation of the particle configurations as well as phase transition in 2D systems in a circular parabolic and hard-wall well using classical Monte Carlo simulations for N= 1-300. Depending on the type of confinement field, the electrons are arranged into shells with an average inter-electron distance which depends on both the radius (shell number) for a particular structure and on the total number of electrons. Some of these ground state configurations for the case of a parabolic confinement potential are depicted in Fig. 2.1. It was found that for large systems the structure of the inner shells is very close to the one of a triangular lattice. Namely, almost all those electrons are sixfold coordinated, whereas outer shells consist of lower-coordinated electrons. Thus there is a competition

between two-types of ordering: ordering into triangular-lattice structure (Wigner lattice) and ordering into a shell structure. The triangular-lattice structure is the ordered configuration for an infinite 2D system of point particles while the shell structure is imposed by the circular symmetry of the confinement potential. In large systems ($N > 40$), particles inside the clusters have less of a restriction on the confinement potential and therefore, build a hexagonal lattice, which is energetically the most favored for continuous system. Radial distribution functions $g(r)$ of electrons on the inner shells show a two-peak structure whereas the outer shells have quite narrow peaks reflecting a well-defined shell radius.

The classical model used below describes quite well the behavior of ions and dusty plasma particles in radio-frequency traps (Paul trap) or Penning traps [31, 32] as well as systems of electrons on helium films [33,34] and semiconductor layers of different forms (superlattice, resonant tunneling device, 2D lateral superlattice) [35]. For two-dimensional systems of electrons, a classical model can be applied if the mean interparticle distance in the cluster, $\overline{r} = (\pi\rho)^{-1/2}$ is larger than the characteristic size of particle wave function in the harmonic potential, $l_0 = (\hbar/m\omega_0)^{1/2}$ (in a macroscopic system the characteristic size is defined by the De Broglie wave length $\lambda = \sqrt{2\pi\hbar^2/m\,k_BT}$). These conditions are fulfilled in systems of electrons (holes) in heterostructures, for example in GaAs/AlGaAs or in quantum dots with densities $\rho < 10^7 - 10^8 cm^{-2}$ and temperatures T $>$ 1K. For higher densities or lower temperature a quantum model has to be used (i.e. example quantum MC methods [39, 40].

In this chapter we deal with classically modeled systems. One of the systems which will be described in Section 2.5, is connected with constructing of micro devices, based on the difference of angular properties of clusters with $N = 19$ and $N = 20$ particles [38]. Here we used electrons as the simulated particles, but obviously we can apply our consideration to systems of other charged particles.

2.2 Structural transitions during melting

During an increase of the temperature in artificial 'atoms' there are two possibilities of disorder. The first one is so-called 'orientational melting'. The orientational melting becomes apparent as different parts of the cluster (shells, in our case) rotate as a whole in relation to each other and lose the orientational

order. The temperature of orientational melting strongly depends on a cluster's symmetry and may vary over many orders of magnitude [40, 44]. If one heats the cluster further, then 'radial melting' can be observed, and particles begin to jump from one shell to another. One should underline that even in the state of radial melting the shell structure in the cluster can still be observed - peaks of the radial distribution function are still sharp in the "liquid phase". These peaks are corresponds to shells on the appropriate distances.

The melting process of small clusters has some differences in comparison with the melting of the macroscopic matter. The melting temperature of finite arrays of ions is found to be lower than that for infinite Coulomb matter, by an amount that depends on the number of charges and on the fraction of ions in the surface layer, in particular [45]. It would appear that the lowered melting temperature is almost entirely due to the finite size rather than the different form of ordering. The diffusion rates in the outer regions are substantially larger when parallel to the surface than perpendicular to it, in the vicinity of the melting temperature. These facts clarify why in general the temperature of 'orientational melting' is lower than 'radial melting'.

An especially big interest is devoted to investigations of so-called *magic number* or highly symmetric clusters. Such clusters, in which the particle number in the outer shells are multiples by those on the inner shells, have high symmetry which leads to particular properties. Examples of these *magic number* clusters in 2D are N =10, 12, 16, 19. Properties of these small clusters were subject of Ref. [40, 46]. In a 2D dusty plasma the *magic number* cluster containing $N = 19$ and non-magic cluster with 20 particles the intershell rotation barrier height could be measured quantitatively by applying a well defined torque on the clusters' outer shell by the radiation pressure of two opposite laser beams. Moreover, a complex behavior is found for the 19-particle cluster where structural transition occurs together with the intershell rotation showing that the presence of shielding of the dust particle interaction can basically change the least stable modes in the finite clusters. The measured crystal properties from the experiment have been compared with MC simulations [46,47] . However, in these equilibrium simulations only a statistical result is obtained. No information is available on how these rotations proceed in a real system, after what time etc. To answer these questions we study the real-time dynamics of classical Coulomb clusters

during intershell rotation. Real-time molecular dynamics simulation results were compared with MC, which does not include time propagation.

Now we enumerate the open questions, which we consider in the next section:

- applying the MD method to simulation of confined 2D systems of charged particles;
- calculation of the intershell rotation barrier heights in the clusters using different approaches;
- investigation of the melting process in the systems;
- investigation of the response of mesoscopic 2D cluster to an external angular excitation;
- control of the angular current by addition/removal of a single electron and simulation of a single-electron device on the example of the cluster $N = 19$.

The next part of the work is organized as follows. In Sec. 2.3 we describe the applied model of classical particles in a confinement potential. Sec. 2.4 is devoted to the method of Molecular Dynamic simulation of these systems. In Sec. 2.4.1 the ground state configurations for clusters with $N < 20$ are discussed for a parabolic confinement potential. We reproduce the shell structure in such small clusters. Sec. 2.4.2 and 2.4.3 are devoted to phase transitions where we present the results from MD simulations at different temperatures and calculate the intershell rotation barriers in the system $N = 12$. We consider the rotation dynamics of the outer shell by application of a short-time external force. Three different methods were used to determine the intershell rotation barrier:

- from the work of the external force;
- from the fluctuation of angular kinetic energy;
- from the change of the potential energy of the cluster.

Using differences in the properties of magic and non-magic clusters in Sec. 2.5 we demonstrate on the example of clusters $N = 19$ and 20 a principal possibility of creation of a micro device with 'open' and 'closed' states, as in a semiconductor diode. The angular current of the outer shell can be controlled by

removal/addition of one particle in the system. Sec. 2.6 gives a brief summary of the main points about the classical system in the confinement potential. The main results of the present chapters were published in Ref. [36, 38, 49].

2.3 Physical model of mesoscopic 2D cluster

Let us consider a finite number N of interacting particles with charge Z and mass m in the external harmonic potential. The particles interact through a repulsive Coulomb potential

$$U_{ij}(r_{ij}) = \frac{Z_i Z_j e_0^2}{4\pi\epsilon\epsilon_0 r_{ij}}, \tag{2.1}$$

where ϵ is the dielectric constant of the medium. The Hamiltonian for such a system is given by

$$H = \sum_{i=1}^{N} \frac{\mathbf{p}_i^2}{2m_i} + \sum_{i=1}^{N} V_c(r_i) + \sum_{i<j}^{N} U_{ij}(\mid \mathbf{r}_i - \mathbf{r}_j \mid), \tag{2.2}$$

where $r_i \equiv \mid \mathbf{r}_i \mid$ is the distance of the ith particle from the center of the confinement potential. For convenience, we will refer to our charged particles as *electrons*, keeping in mind that they can also be ions or any other charged particles. So in following we set $Z_i = -1$ and $m_i = m$. Generalizations are straightforward.

The first term in Eq.(2.2) is the classical kinetic energy of the system and the second term represents particle energy in the confinement potential, where we consider the the following case:

$$V_c(r) = \frac{m\omega_o^2 r^2}{2}. \tag{2.3}$$

There are other types of confinement, like hard-wall confinement [41], but we consider systems only in the parabolic confinement potential (Eq.(2.3)).We will express the coordinate in units of r_o, defined from the expression

$$\frac{e_0^2}{4\pi\epsilon\epsilon_0 r_0} = \frac{m\omega_0^2 r_0^2}{2},$$

as

$$r_0 = \left(\frac{e_0^2}{\epsilon_0}\frac{2}{m\omega_0}\right)^{1/3} \tag{2.4}$$

momentum as

$$p_0 = \sqrt{2k_B T m} \tag{2.5}$$

and the energy in the units

$$E_0 = \frac{e_0^2}{4\pi\epsilon\epsilon_0 r_0}. \tag{2.6}$$

Temperature is defined by analogy with temperature of a macrosystem as

$$k_B T = \frac{1}{N}\sum_{i=1}^{N}\frac{p_i^2}{m_i}. \tag{2.7}$$

The distance r_0 defined by Eq.(2.4), corresponds to the stable distance between particles for $N = 2$.

All results will be given in reduced form, i.e. in the above dimensionless units. In these units the Hamiltonian (Eq.2.2) becomes

$$H = \frac{1}{\Gamma}\sum_{i=1}^{N}\mathbf{p}_i^2 + \sum_{i=1}^{N} r_i^2 + \sum_{i<j}^{N}\frac{1}{\mid \mathbf{r}_i - \mathbf{r}_j \mid}, \tag{2.8}$$

$$\Gamma = \frac{E_0}{p_0^2/2m} = \frac{E_0}{k_B T}. \tag{2.9}$$

Here Γ is the classical coupling parameter of the system, the ratio of the mean potential energy to the mean kinetic energy. The coupling parameter Γ measures the strength of correlations in the system.

We notice that ground state configurations do not depend on the value of the confinement frequency ω_0. The confinement frequency ω_0 defines the length and energy scales in the system. Changing the number of electrons N will, on average, not change the dimensionless density ρ of the system (in units of $\rho_0 = \pi r_0^2$), which is determined by the strength of the confinement frequency.

2.4 Molecular Dynamics simulation of confined mesoscopic systems

In standard Molecular Dynamics a time propagation of the system is achieved by numerical solution of N differential Newton's equations of motion:

$$m_i \frac{d^2\mathbf{r}_i}{dt^2} = \mathbf{F}_i, \tag{2.10}$$

$$\mathbf{F}_i(t) = \sum_{j,j>i}^{N} \mathbf{F}_{ij}(t) - \nabla_{\mathbf{r}} V_c. \tag{2.11}$$

where $\mathbf{F}_i$ is the sum of all forces, acting on the ith particle. In the case of the confined system it is the sum of all particle-particle interactions (first term in Eq. (2.1)) and the confinement force (second term), created by external potential Eq. (2.3). Interparticle interactions are repulsive whereas the confinement force pushes a particle towards the center of the parabolic potential. In our simulations we have used the standard velocity algorithm of Verlet [50].

$$\begin{aligned} \mathbf{r}(t+\Delta t) &= \mathbf{r}(t) + \mathbf{p}(t)\Delta t/m + \mathbf{F}(t)\frac{\Delta t^2}{2m} \\ \mathbf{p}(t+\Delta t) &= \mathbf{p}(t) + \frac{\mathbf{F}(t)+\mathbf{F}(t+\Delta t)}{2}\Delta t. \end{aligned} \tag{2.12}$$

The algorithm is simple to realize and it has small round-off error effects on big time scales [51]. The time step Δt is chosen small enough to guarantee conservation of total energy. At the same time the time step should be as big as possible in order to allow for long runs in the phase space. A particularity of the Verlet algorithm is that the calculation of coordinates is performed before the calculation of velocities. The timestep in the present simulation was $9.4 \cdot 10^{-3} T_0$, where $T_0 = 2\pi/\omega_0$, is the time period of the present confinement field.

We perform the simulations in the canonical ensemble with constant temperature or coupling parameter Γ. In order to achieve defined Γ value we rescale the velocities of all particles after every timestep.

$$\Gamma(t) = \frac{E_0(t)}{k_B T(t)} = \frac{E_0}{\sum_{i=1}^{N} p_i^2(t)/2m}$$

$$p_{i,scale}^{x,y} = \alpha p_i^{x,y};\ \alpha = \sqrt{\frac{\Gamma(t)}{\Gamma}} \tag{2.13}$$

In all cases, first equilibrium configurations were reached using thermal scaling. The initial velocities were chosen such that all particles had only radial velocity components, i.e. the whole angular momentum of the system was zero.

During equilibration, the kinetic energy was spontaneously distributed in all directions but still maintaining a zero total angular momentum $\mathbf{L}$, which is

$$\mathbf{L} = \frac{1}{m}\sum_{i=1}^{N} \mathbf{r}_i \times \mathbf{p}_i. \tag{2.14}$$

We will consider the process of equilibration in detail in Sec. 2.4.1. In some cases after equilibration was reached the velocity scaling was turned off.

2.4.1 Ground state configurations of the small clusters

In our work, the first step was the search of the configuration in which the system has a global energy minimum (Eq. 2.8). It is very important to find configurations that positively ensure that the potential energy (second and third terms in Eq. 2.8) is at the global minimum and not local minimum. This global minimum coincides with the global minimum of the total energy if all velocities are equal to zero, which yields the classical ground state. The search of ground state configurations for big clusters ($N > 40$) is a quite complicated task, because the number of local minima grows rapidly with an increasing number of particles and at the same time every local minimum has its own convergence region. The probability to find a configuration which guarantees a global minimum of potential energy is essentially reduced if the convergence region of a local minimum turns out narrower as than one of a global minimum.

To solve this problem clusters in Ref. [41] were heated up and cooled down to $T = 0$ to check it there was a global minimum. But this may be not the best way, because the difference of potential energies per particle U/N is usually quite small (for $N = 19$ $U\{1, 7, 11\} - U\{1, 6, 12\} = 8.73 \cdot 10^{-4} E_0 = 1.1 \cdot 10^{-4}\%$, numbers in parentheses are numbers of particles on the corresponding shells). In such cases the only reliable way is to start searching from several independent initial configurations.

In Tab. 2.2 we compare our results for internal energy of several 2D Coulomb clusters with classical MC simulations [41, 52]. MD simulations are given for $\Gamma = 10^4$ and agree with the MC data within the statical errors. Due to the small number of simulated particles the statistical errors of internal energy are relatively big.

N	N_1, N_2, N_3	H/N, MC [52]	H/N, MD
5	4	2.33845	2.33840
9	2, 7	4.08813	4.08819
12	3, 9	5.23896	5.23909
19	1, 6, 12	7.63197	7.63208
19	1, 7, 11	7.63280	7.63286
20	1, 7, 12	7.94961	7.94968

Table 2.2: Ground state configurations and internal energy of classical 2D Coulomb clusters in a radial-symmetric parabolic confinement potential. MD simulations were performed for systems with $\Gamma = 10^4$. N- is the number of particles, N_1, N_2... are populations of the shells. The metastable configuration $\{1, 7, 11\}$ for $N = 19$ is also shown .

As we can see in Fig. 2.1, the addition to the system of new particles leads to changes of the number of shells and their populations.

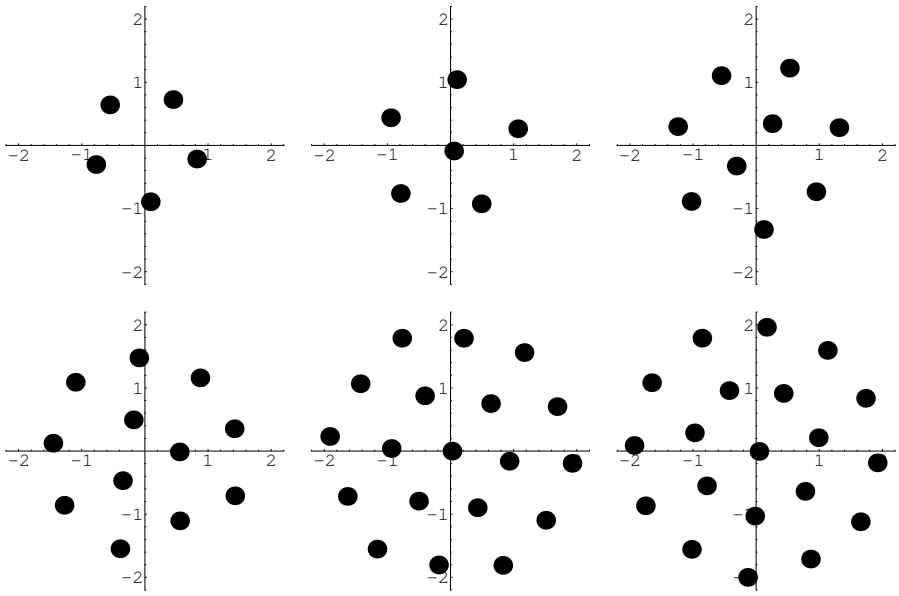

Figure 2.1: Equilibrium configurations of clusters $N = 5$, 6, 9, 12, 19 and 20 at $\Gamma = 500$ ($T = 3.33 \cdot 10^{-3}$). One can see hexagonal symmetry and formation of a shell structure with increasing of N .

There are rules for filling the shells:

1. Rules for the number particles in the first shell:
   (a) The first shell contains a maximum of 5 particles.
   (b) Two particles appear only when we add one particle to the system which has the configuration {1, 7,...}.
   (c) Three particles appear only when we add one particle to the system which has the configuration {2, 8,...}.
   (d) Four particles appear only when we add one particle to the system which has the configuration {3, 9,...}.
   (e) Five particles in the center appear only when we add one particle to the system which has the configuration {4, 10,...}.
2. Second shell never exceed $N_2 \leq 10$ particles for $N \leq 50$, and $N_2 \leq 11$ for $N > 50$.
3. Increasing number of particles on the inner shell takes place when the difference between number of particles on all other shells approaches the maximal allowable values.
4. Differences between the numbers of particles ΔN on neighboring shells strives for a minimum and lies in the range $3 \leq \Delta N \leq 6$. This rule is fulfilled for small clusters ($N < 82$) where the shell structure prevails on the triangular-lattice structure.

All equilibrium states of clusters were reached from initial configurations which had only radial kinetic energy. On Fig. 2.2 on example of the relaxation of radial and tangential energy in the cluster $N = 19$ from some initial configuration to equilibrium is shown. The initial state was choosen as the ground state whereas all particle velocities were directed towards the origin $r = 0$. Radial and tangential kinetic energy are calculated as

$$E_{k\phi} = \sum_{i=1}^{N} \frac{p_{i,\perp}^2}{2m}, \tag{2.15}$$

$$E_{kr} = \sum_{i=1}^{N} \frac{p_{i,\parallel}^2}{2m}, \tag{2.16}$$

where $p_{i,\perp}$and $p_{i,\parallel}$ are components of the momentum, perpendicular and parallel to the radius vector $\vec{r}$.

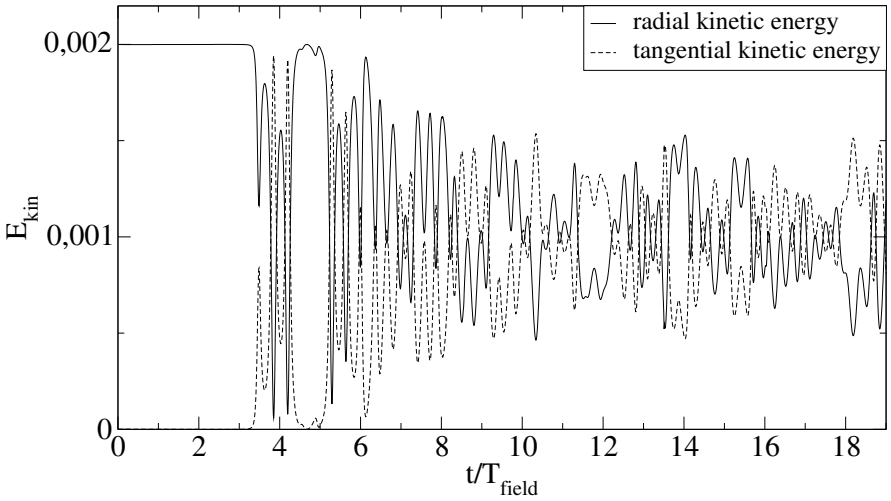

Figure 2.2: Relaxation of radial and tangential kinetic energy to equilibrium in the cluster $N = 19$ from initial configuration to the equilibrium state with $\Gamma = 500$. Energy in units of E_0.

There are three stages of evolution of kinetic energy in this example. At the first one, from $t = 0$ to $t \approx 3.5\,T_0$, all particles under the influence of confinement potential move towards the origin $r = 0$, the cluster is compressed. There is only the 'breathing' energy mode, which is defined in Ref. [53] as an oscillation of the sum of radial positions of all particles $\sum \mathbf{r}_i/N$. Then, after the particles have reached nearly equilibrium positions, radial kinetic energy is partially redistributed into tangential kinetic energy. This redistribution lasts till time $t \approx 10\,T_0$, and then it exibits more or less equilibrium stationary velocity behavior. Total kinetic energy remains constant due to velocity scaling. This behavior is typical for many initial conditions.

The further dynamics of the cluster strongly depend on the the number of particles N, which defines the shell structure and the coupling parameter Γ (or "temperature") of the cluster. In the next section we will consider the dynamic of particles in the cluster with $N = 19$.

2.4.2 Melting

As we mentioned before in Sec. 2.2, there are some clusters with *magic numbers*. These clusters have maximal numbers of particles on the outer shell and coordination number $C = 6$ of the outer shell with very high angle symmetry. These clusters possess some special properties. The numbers of particles on the shells in such systems in ground state configuration have a common denominator, e.i. in clusters $N = 10$ {2, 8}, 12 {3, 9}, 17 {1, 6, 10}, 19 {1, 6, 12}. Also the second derivate of specific total energy by the numbers of particles $\partial^2(H/N)/\partial N^2$ has maximal values in magic clusters [47].

The classical coupling parameter Γ in continuous media, as a ratio of the mean potential energy to mean kinetic energy k_BT can characterize a range of phase transition. In low-density and high temperature systems parameter Γ is small ($\Gamma < 1$) and Coulomb interaction does not play a big role. At the intermediate densities ($1 < \Gamma < 100$) movements of electrons are highly correlated and looks like they are moving in liquid. At higher densities of electrons and lower temperatures ($\Gamma > 100$) Coulomb interaction plays a determining role and transition to the state with space periodical distribution of charged centers takes place, i.e. Wigner crystal is formed. Similarly to the continuous systems, if we replace mean interparticle distance in potential energy by value r_0(Eq.(2.4)) we will have the coupling parameter for cluster systems.

To investigate the melting process of magic clusters we consider the cluster $N = 19$ in equilibrium for coupling parameters Γ= 500, 400, 340, 300, 250, 200, 160, 150, 160, 50, 30, 10. We calculate the single-particle density distribution $P(\mathbf{r})$ as

$$P(\mathbf{r}) = \frac{1}{N}\sum_{i=1}^{N}\langle\delta(\mathbf{r}-\mathbf{r}_i)\rangle\,, \tag{2.17}$$

where $\mathbf{r}_i$ is radius vector particle i, and the average is over the duration of the MD simulation.

Fig. 2.3 shows 2D profiles of the particle density distributions for the 3 lowest temperatures or highest coupling parameter Γ =500, 400 and 340. At low temperature electrons are well localized near their equilibrium positions, and deviations from these positions are small in comparison to the mean interparticle distance r_0. It is interesting to mention that in spatially bounded systems these

deviations are anisotropic due to the space non-linearity of the external confinement potential. Angular components of the deviation dominate in systems where angular symmetry dominates the particles distribution on the shells.

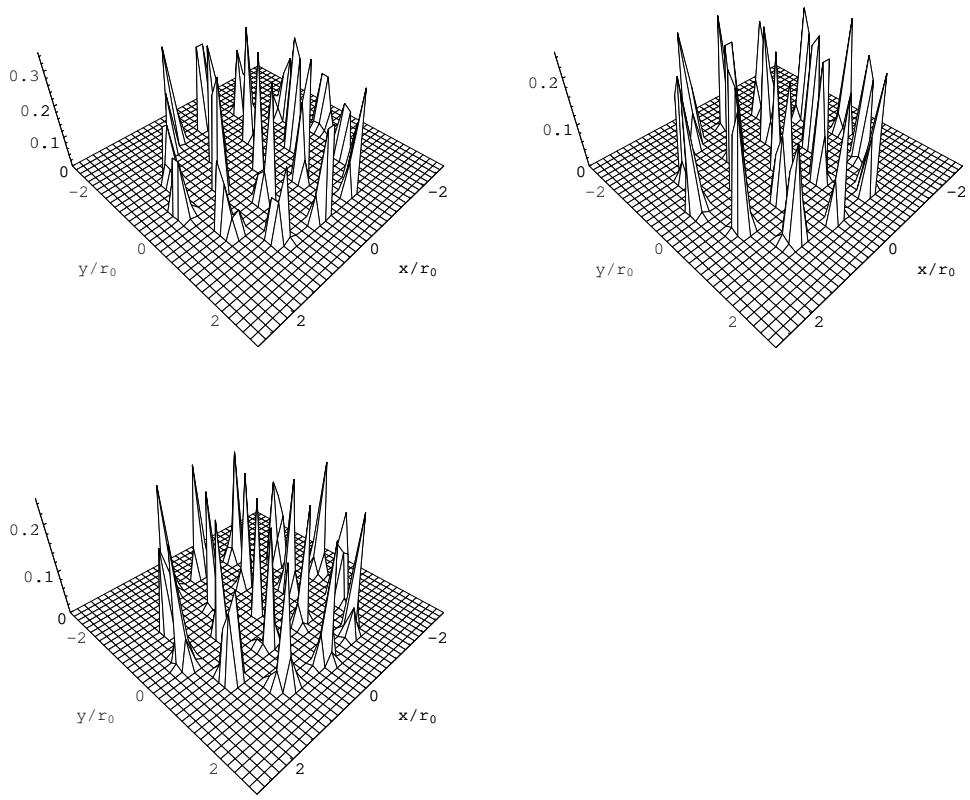

Figure 2.3: Snapshots of the density distribution in the cluster $N = 19$ in a parabolic confinement field for 3 values of coupling parameter: $\Gamma = 500$ (top left), 400(top right) and 340 (bottom). All clusters are in the crystal phase.

We see that even at low temperatures the form of the one particle distribution has a small elliptic deformation along the shell circle. As a result the temperature of orientational melting (OM) is always much lower then the temperature of radial melting (RM). The density peaks of all particles have approximately the same height; it means that there is not any kind of structure change. There is zero probability of electron jumps between the shells.

The Fig. 2.4 shows the density distributions in the range $160 \leq \Gamma \leq 300$. We observe increasing probabilities of transitions of particles between stable positions

on the inner and outer shells, respectively. With increasing temperature the peak heights become smaller, and the values of the distribution between neighboring peaks grow. Only the particle in the center of the cluster stays in the same place due to still high intershell barrier, so its peak remains constant during heating.

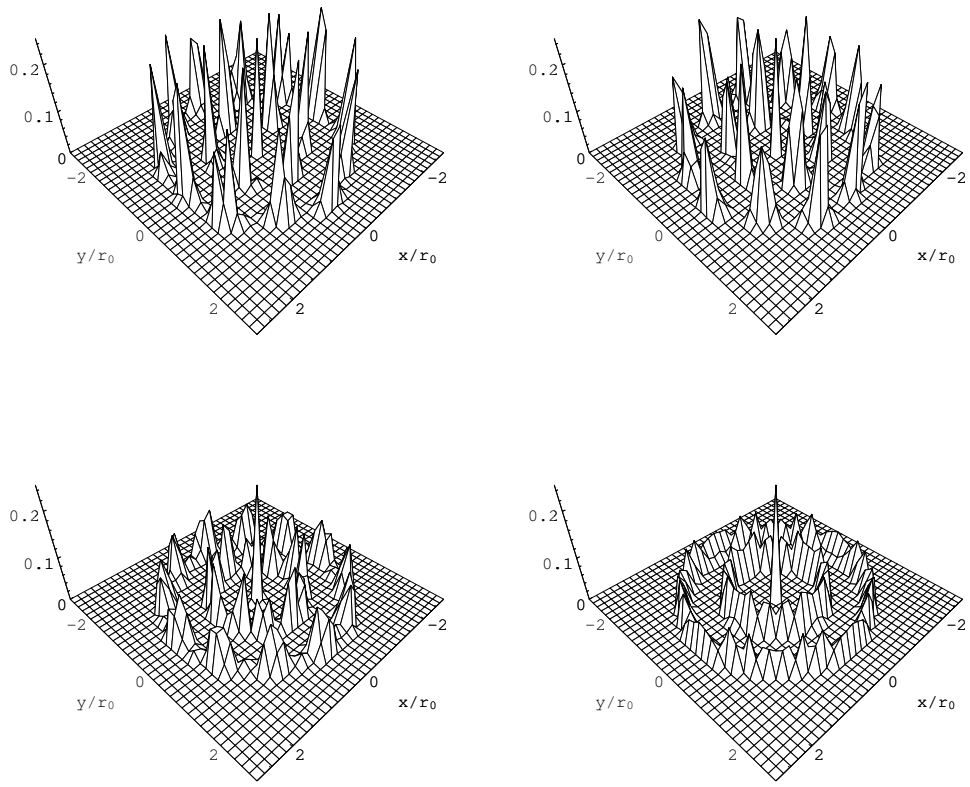

Figure 2.4: The same as in Fig.2.3 but for four values of $\Gamma = 300$ (top left), 250 (top right), 200 (bottom left) and 160 (bottom right), which is in the region of orientational melting.

It should be noted that the angular displacements of the particles on the shells have collective character. The whole shell begins to rotate, it is not a series of uncorrelated unique jumps of some particles. These shell rotations generate random circular currents in a clockwise or counterclockwise direction. At temperatures close to the temperature of OM the shells tend to execute jumps, instead of steady angular motion (see $\Gamma = 300$ in Fig.2.5).

The higher the temperature of the clusters, the bigger the angular currents of

the shells. Beginning from $\Gamma = 200$ the heights of the density peaks on the shells become comparable with the density heights between main positions. In the case $\Gamma = 160$ (bottom right of Fig.2.4) the temperature is near the temperature of RM; there are no more constant particle positions on the shells - the two shell rings rotate relative to each other all the time.

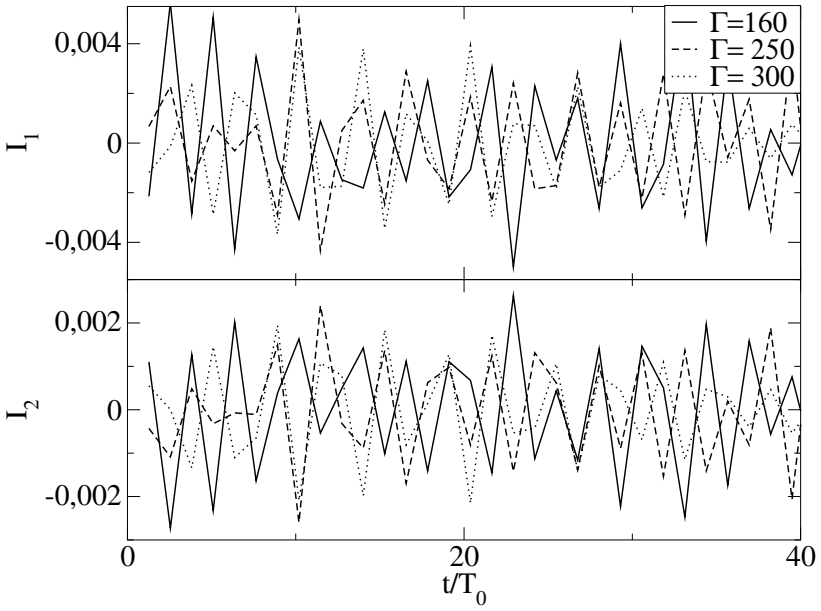

Figure 2.5: Currents I_1 of the first (top graph) and second I_2 (lower graph) shells of the cluster $N = 19$ under Γ =160, 250 and 300 versus time in equilibrium state. Currents are in units of $I_0 = e_0 r_0/T_0$, time in units of the period of the confinement field $T_0 = 2\pi/\omega_0$. All temperatures are above the orientational melting (OM) temperature ($\Gamma^{OM} \simeq 333$).

The maxima of the circular shell currents also grow with increasing temperature. In Fig. 2.5 the dependence of the tangential currents I_a^t on time is depicted. Tangential current of the shells was calculated by analogy with tangential kinetic energy E_{kin}^t [Eq.(2.15)] as

$$I_a^t = \frac{e_0}{m} \sum_{i=1}^{N_a} \mathbf{p}_{i,\perp} \,, \tag{2.18}$$

where N_a is number of particles on the shell a.

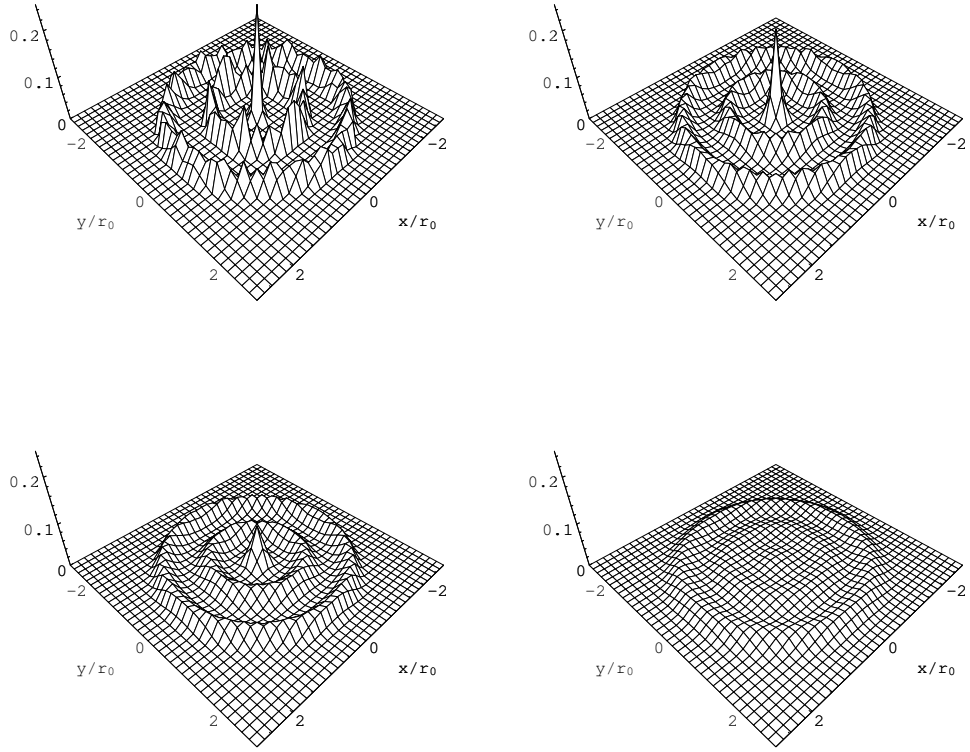

Figure 2.6: The same as in Fig. 2.4 but $\Gamma = 150$ (top left), 50 (top right), 30 (bottom left), 10 (bottom right). All systems are in the phase region of radial melting.

The inner and outer shells rotate in opposite directions. It is easy to observe that the ratio of the tangential current of the inner shell to the tangential current of the outer shell is $I_1^t/I_2^t \approx -2$. If we consider a shell as the rigid ring then the ratio of angular moment is

$$\frac{M_1}{M_2} = \frac{R_1^2\, p_1^t}{R_2^2\, p_2^t} = \frac{v_1^t}{4\, v_2^t} = -1, \tag{2.19}$$

where M_1, M_2 are the angular momenta , R_1, R_2 are the radii and p_1^t, p_2^t and v_1^t, v_2^t are the angular momenta and velocity of inner and outer shells respectively. Recall that at the the initial moment the whole cluster has zero total angular moment which is conserved in the simulation. Here, approximately $R_2 = 2R_1$.

So, the ratio of tangential currents is

$$\frac{I_1^t}{I_2^t} \approx \frac{m\, N_1 v_1^t}{m\, N_2 v_2^t} = -\frac{6}{12}\,\frac{4}{1} = -2. \tag{2.20}$$

The particle in the middle of the cluster also possesses some very small angular momentum, that is why in the simulation we have a small fluctuation of the current ratio.

If the temperature of the cluster is above the temperature of radial melting, the shells no longer possess a stable particle configuration. Radial fluctuations become big enough to overcome the intershell potential barrier. Fig. 2.6 shows cluster $N = 19$ for temperatures above the radial melting coupling parameter $\Gamma^r = 155$. The process of particle exchange between the shells leads to a decrease of the maximal density values (consider for example to the density peak of the particle in the center of the cluster) and increasing width of the shells. But even at this stage the angular movement prevails over the radial one - the peak of density of the central particle, which has practically only a radial velocity component, is still bigger then for particles on the circular rings. Finally, when the coupling parameter is below $\Gamma \approx 10$, angular and radial energy components become of the same order. Interestingly, the shell structure can be observed even at such high temperatures.

Transition of cluster from a well-ordered to a disordered state also has influence on pair distribution function $g_{ij}(r)$(Eq.(2.21)) which we define as

$$g_{ij}(r) = \frac{2}{N(N-1)} \sum_{i \le j} \langle \delta(r - \mid \mathbf{r}_i - \mathbf{r}_j \mid) \rangle \,, \tag{2.21}$$

where, as in the single particle density distribution Eq. (2.17), $\mathbf{r}_i$ is the radius vector particle i and the average is over the duration of the simulation.

On Fig.2.7 the results of calculation for the cluster $N = 19$ in the range of coupling parameter $10 < \Gamma < 400$ are shown. One sees that in the region of RM the position of the first peak (top graph) is being shifted to smaller values during the heating, particles can move closer to each other. With increasing temperature the amplitude of particle fluctuations is growing leading to a widening of the shells in a radial direction, the shells can exchange particles. The second peak is not well defined which is analogous to a conventional solid-liquid transition. This justified the use of the term “melting” for these small clusters.

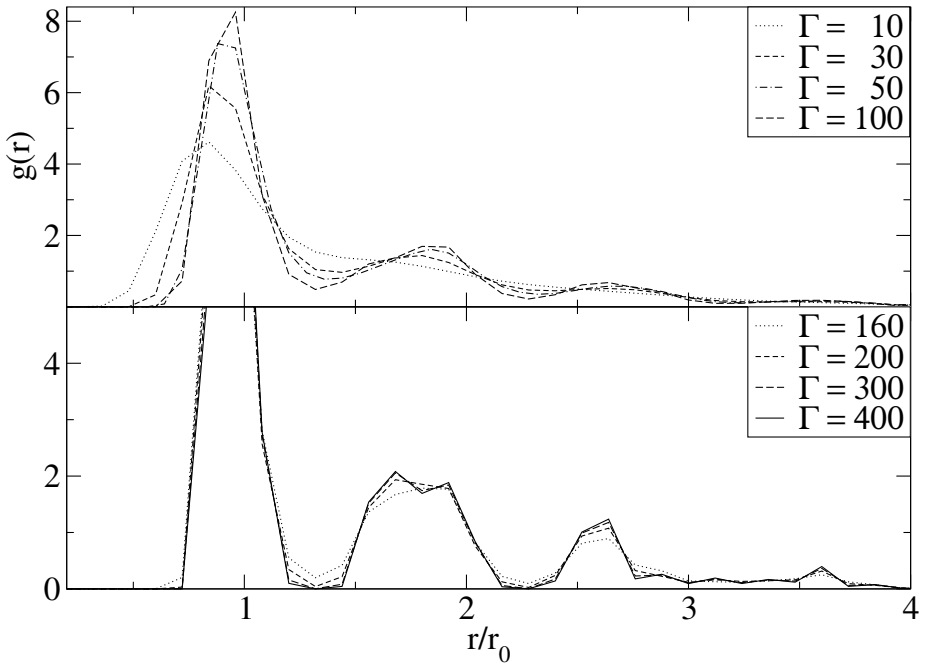

Figure 2.7: Pair distribution functions $g(r)$ of the cluster $N = 19$ $\{1,\ 6,\ 12\}$ in the range of coupling parameter $10 < \Gamma < 400$. The critical values of the coupling parameter at radial melting is $\Gamma^r = 155$, at orientational melting $\Gamma^o = 333$.

In the region of orientational melting $155 < \Gamma < 333$ the functions are changing slowly. The position of the first peak is constant, the close order is formed, as in usual solids. Due to rotation, the values of $g(r)$ between the first and second peaks are not zero and is increasing with increasing temperature. Above the critical coupling parameter of orientational melting $\Gamma^o = 333$ there are two small peaks on the second peak because the cluster $N = 19$ has hexagonal symmetry and particles are situated at a different distance on the second shell.

During cluster melting, the particles exchange their equilibrium positions. During this process the particles have to overcome some potential barriers. Also the non monotonic dependence of the radial and angular fluctuations on temperature shows the presence of potential barriers. In this way, the process of radial melting can be considered as a jump of one particle over the barrier between shells and orientational melting as synchronous passage all particles of one shell over an angular potential barrier. These latter kind of barriers will be investigated in the next section.

2.4.3 Intershell rotation barriers of clusters with 2 shells

Let us focus on the magic clusters and investigate their barriers for intershell rotation, i.e. the energy needed to allow for intershell rotation. This question has been investigated previously by means of Monte Carlo techniques, e.g. [41,47] which allows to accurately compute the threshold energy for intershell rotation. However, in these equilibrium simulations only a statistical result is obtained. No information is available on how this rotation proceeds in a real system, after what time etc. Some attention was paid to dynamic investigation of two-shell carbon nanoparticles in Ref. [54]. MD simulations of a 3D model of fullerene C_{20} and C_{240} were performed there. Interaction between atoms of the neighbor shells was described by short-range Lennard-Jones potential, interaction between atoms inside shells - by the Born potential. Dynamic properties of the fullerenes like reorientational frequency and angular distributions versus temperature are calculated. But still there are some open questions, for example, the authors in Ref. [54] mention a possible decrease of the rotation barrier with increasing temperature, but MC calculation [47] shows that the barrier height stays almost unchanged below or near the critical melting temperature. Spectral properties of small clusters was the subject of study in the works [53, 55, 57], a theoretical and experimental investigation of potential barriers was given in Ref. [46, 58].

To answer these questions about the rotation process we study the real time dynamics of classical Coulomb clusters during intershell rotation and radial melting. We perform a realistic computer experiment where an angular force F^{ext} acts on one of the shells, and the subsequent dynamics of the system is monitored. From a series of such calculations with varying amplitude of F^{ext} we determine the height of the barriers for intershell rotation for the magic clusters with $N = 12$ and $N = 19$.

In our simulations we take two-dimensional clusters with N particles in the parabolic trap with frequency ω_0. The particles interact via a pure Coulomb potential. Total energy of the system is then given by Eq.(2.8).

Here we provide only the specific parameters for the situations studied below. The time step in the present simulations was $9.4 * 10^{-3} T_0$, where $T_0 = 2\pi/\omega_0$, is the time period of the confinement field. In all cases, first equilibrium configurations were reached using thermal scaling to achieve the given temperature or, equivalently, the needed value of Γ. The initial velocities were chosen such

that all particles had only radial velocity components, i.e. the whole angular momentum of the system was zero. During equilibration, the kinetic energy was spontaneously distributed over all directions but still maintaining zero total angular momentum. After equilibration was reached the velocity scaling was turned off. The temperature of the systems was taken sufficiently below the temperature of orientational melting to guarantee absence of intershell rotation (in the runs below, Γ was in the range $1000 \ldots 5000$, whereas the threshold for orientational melting is $\Gamma = 330$ for $N = 19$ and $\Gamma = 1250$ for $N = 12$, cf. [40]). To prevent rotation of the cluster as a whole, one particle on the inner shell was pinned (it was allowed to move only radially).

In the equilibrium state with the temperature below the orientational melting threshold, the outer shell cannot rotate with respect to the inner one but oscillates between the peaks of the angular barriers, the angular distance between two adjacent peaks is given by $2\pi/N_{out}$, where N_{out} is the number of particles on the outer shell.

To make the outer shell go over the angular barrier, one has to supply additional kinetic energy. We choose an external force acting in tangential direction on all particles of the outer shell. In order to avoid continuous angular acceleration and heating (i. e. decreasing of Γ) a short pulse was used which was of the form

$$F^{ext}(t) = F_0^{ext}[1 - e^{-t/T_0}], \quad t \leq t_1. \tag{2.22}$$

For $t \geq t_1$ the force was zero. The duration t_1 was chosen shorter than the period of intershell oscillations in the absence of the force. By this it was achieved that the external force dominantly excited angular motion of the outer shell without loosing much energy for excitation of oscillatory degrees of freedom.

Depending on the force amplitude F_0^{ext} and its duration, we observe differing behaviors of the cluster. Angular trajectories of one particle of the outer shell in the cluster with $N = 19$ are depicted in Fig. 2.8 for various force amplitudes. The time behavior of the external force is also shown (left bottom corner). In all cases the pulse duration was less than the period of the angular oscillations. We see that without external excitation the outer shell (containing 12 particles) spontaneously oscillates with an angular amplitude of approximately 7.5 degrees relative to the pinned inner shell around the ground state position (of 30 degrees). Applying a weak external force, the amplitude of the oscillations increases and its

period grows as well. At the threshold force the oscillation amplitude reaches the critical value of 15 degrees corresponding to the top of the barrier. In this case the outer shell can rotate relative to the inner shell by 30 degrees, as can be seen from the dotted curve in Fig. 2.8. The additional weak high-frequency modulation is connected with particle oscillations with the frequency of the confinement field ω_0.

The same excitation mechanism was applied to the cluster with $N = 12$. It has a much lower barrier height (reflecting the higher orientational melting parameter Γ, see above), thus the threshold force is significantly reduced compared to the case of $N = 19$.

In order to define the potential barrier for the intershell rotation, U_{rot}, we first perform a series of calculations with varying force amplitude *above* the threshold value. In this case, the outer shell has sufficient angular kinetic energy to perform a quasi-steady rotation with respect to the inner shell with period T_{rot}.

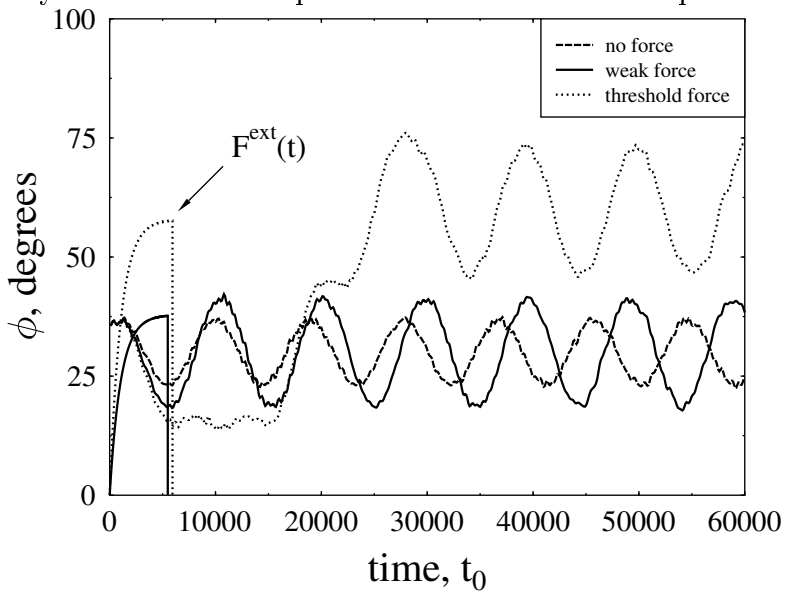

Figure 2.8: Angular position of one particle on the outer shell for $N = 19$ vs. time. Short curves in the left bottom corner show the time dependences of the external force $F^{ext}(t)$ (arbitrary units). Time in units of time step $t_0 = 9.4\,10^{-3} T_0$.

Reducing the amplitude of F^{ext} leads to slower rotations (i.e. T_{rot} increases) until T_{rot} diverges for the threshold force. We compute the barrier value as the limit of the work W^{ext}, produced by the external force during its action, from

time t_0 to t_1 where the angular position of the outer shell evolves from ϕ_0 to ϕ_1

$$W^{ext}(F_0^{ext}) = \int_{\phi_0}^{\phi_1} M^{ext}(\phi)d\phi = \int_{\phi_0}^{\phi_1} |\vec{r}_{out}(t) \times \vec{F}^{ext}(t)|d\phi = \\ = \int_{t_0}^{t_1} F^{ext}(t)\, r_{out}(t)\, \omega(t)dt. \tag{2.23}$$

Here, r_{out} denotes the radial distance from the trap center of one particle of the outer shell which may vary during the excitation and ω is the angular velocity of that particle.

In Fig. 2.9 the work W^{ext} is shown versus half of the intershell rotation period T_{rot}. Each of the symbols denote a separate calculation with a given force amplitude F_0^{ext} which uniquely corresponds to a given T_{rot}. By extending the calculations to $T_{rot} \to \infty$ we expect to obtain the threshold value of W^{ext}.

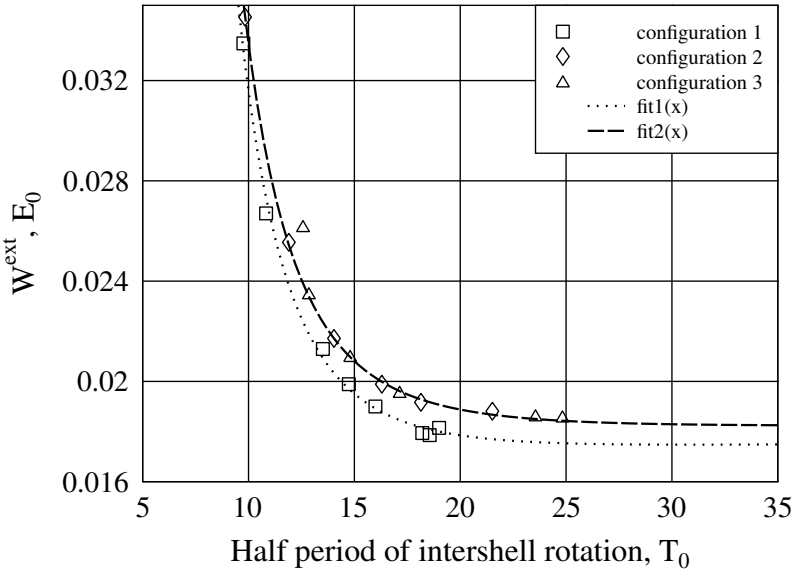

Figure 2.9: Work of the external force necessary to rotate the outer shell relative to the pinned inner shell by 180°. $N = 12$, $\Gamma = 5000$. Time in units of T_0.

However, when approaching the threshold, the intershell rotation is disturbed by rather complex oscillatory motion. To avoid this problem, we did not extend the calculations beyond $T_{rot}/2 = 25$. Instead, we performed a series of calculations for finite T_{rot} from which we obtained an analytical fit of the form $W^{ext}(x) = a + b/x^2 + c/x^4$, where $x = T_{rot}/2$. Using this fit we extrapolated

the numerical data to infinity and obtained for the barrier $U_{rot}(N = 12)/E_0 \approx \lim_{x\to\infty} W^{rot}(x) = a = 0.018 \pm 0.0014$. In order to estimate the magnitude of the statistical error resulting from the choice of the initial data as well as from differences between different particles on the outer shell we performed a series of calculations three of which are shown in the figure. Configurations 1 and 2 correspond to different initial conditions but the same particle, whereas configuration 3 denotes an average over all 9 particles on the outer shell. As a result we may conclude that the deviation between different realizations is approximately 6 %.

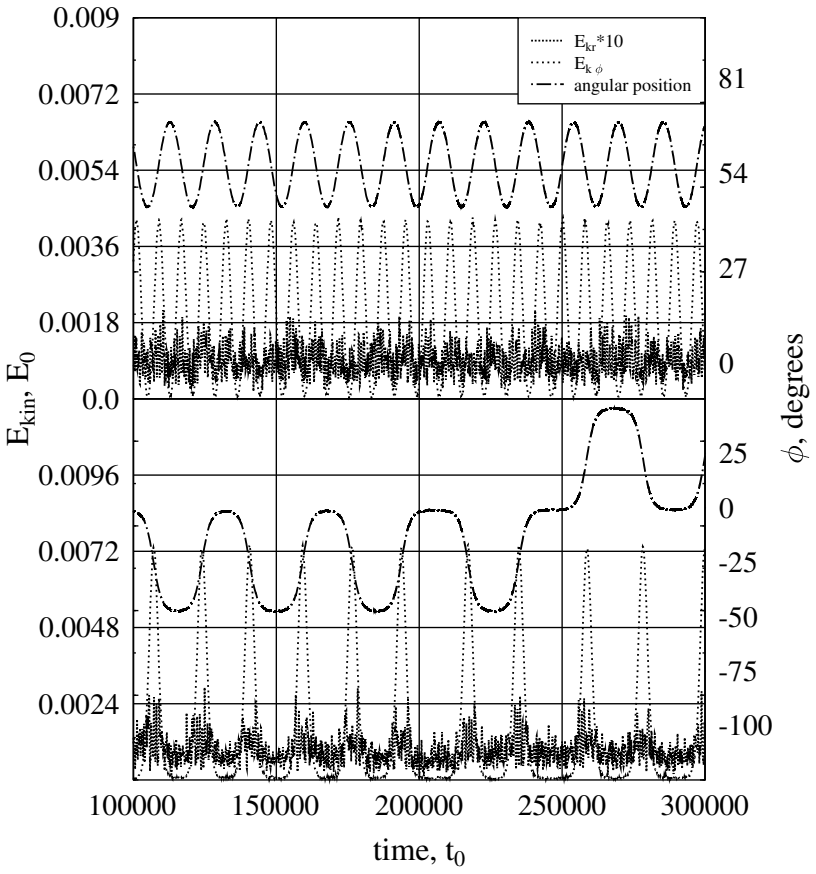

Figure 2.10: Radial E_{kr} and angular $E_{k\phi}$ parts of kinetic energy of the outer shell and relative angular distance between shells (right axis). Upper graph: no external force, lower graph: with external force, close to intershell rotation threshold. Time in units of T_0.

The above threshold value is about twice as larger than the result obtained from classical Monte Carlo simulations [47]. The probable reason is that not all

work of the external force is converted into intershell rotation, part of it goes into excitation of high frequency oscillations.

To analyze this question, we now consider the energy distribution between radial and angular motion before and after excitation. In Fig. 2.10 we depicted the time evolution of radial and angular kinetic energies before and after application of the force to the outer shell. As can be seen from the upper picture (no force applied), in thermal equilibrium almost all kinetic energy resides in tangential motion of the whole shell, the radial component of kinetic energy is approximately 20 times less. The minimum of angular kinetic energy appears when the particles reach the boarder of the barriers (turning point), so the shell starts to move in the opposite direction. Let us now consider the same after external excitation. The lower figure shows the energy relaxation sufficiently long after the force close to the threshold has been turned off. We find that the external force increases the radial component of kinetic energy of the outer shell by approximately 50% and similar behavior is found for both components of the kinetic energy of the inner shell (not shown in the figure). A much stronger increase appears in the angular kinetic energy, its maximum goes up to a value above $0.0074E_0$ (almost by a factor of two). At some random moment of time the shell makes a jump by 30 degrees (see right axis). The corresponding value of angular kinetic energy maximum can be also treated as the height of the barrier for intershell rotation which turns out to be very close to the Monte Carlo result, see below.

It is interesting to compare the behavior of potential energy on the same time scale (Fig. 2.11). Potential energy is found to oscillate with two main frequencies: first, there is a fast mode with the frequency $2\omega_0$ connected with the frequency of the trap and, secondly, there is a slow mode which reflects the relative angular displacement of the inner and outer shells. We again start with the case without external force, see upper figure. The turning points of the intershell oscillations correspond to "highest" values reached in the intershell potential, thus there the potential energy is maximal. The lower picture shows potential energy after the external excitation, at the moment of an intershell rotation. As one can see, the high-frequency mode is unchanged, whereas the slow mode clearly reflects the motion across the rotational barrier.

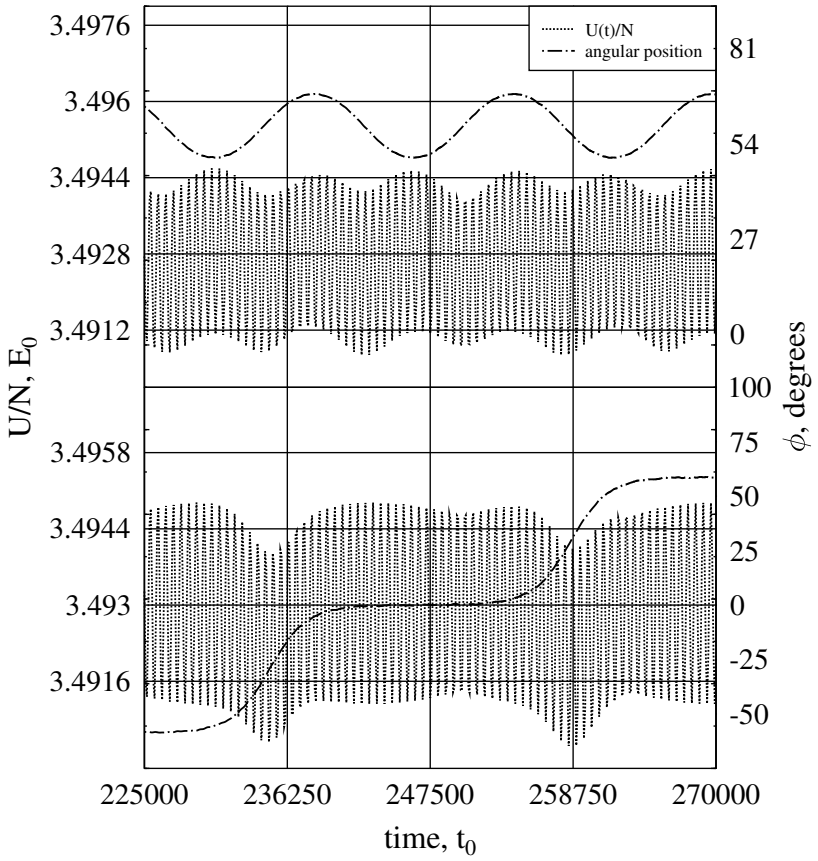

Figure 2.11: Potential energy per particle as a function of time. The upper picture shows the case without external force, the lower picture with external force, close to the rotation threshold. Same parameters as in Fig.2.10, but note the different time scale.

In Fig. 2.12 we plot the angular dependence of the intershell rotation barrier and compare our data to that of classical Monte Carlo simulations [47]. Qualitatively both approaches coincide very well and both agree on the minimum values of the potential. On the other hand, the MD simulations yield slightly higher values for the peak height of the potential. This is readily explained by the fact that, in order to overcome the barrier dynamically, the outer shell needs to have a finite angular velocity.

We can make some concluding remarks. From the three used MD approaches to the intershell rotation barrier we have obtained the following values for the barriers for $N = 12$: i) from the computation of the work of the external force: $U_{rot} = 0.018 \pm 0.0013 E_0$, ii) from the maximum of angular kinetic energy $0.0074 E_0$, and iii) from the change of potential energy $0.0082 E_0$. Classical MC simulations give us $0.00733 E_0$ [47].

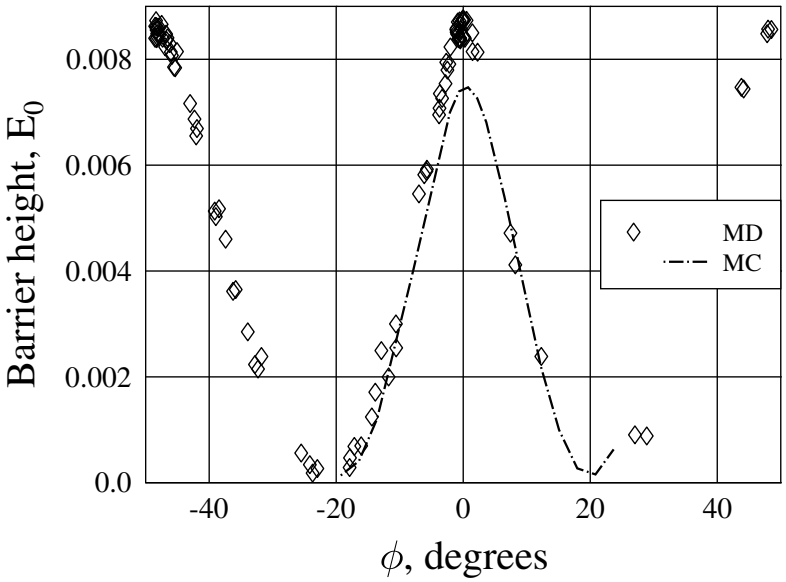

Figure 2.12: Intershell rotation barrier for the cluster with $N = 12$ as a function of the angle between the two shells.

So, the most accurate data, and that closest to MC intershell rotation barrier data is obtained from the value of the maximum of angular kinetic energy. The differences can be explained by the peculiarities of the measured values. In the case of the work W^{ext}, we found that not all external energy goes into angular motion, some energy is lost to excite high-frequency radial oscillations which results in values too high for the rotation barrier. The result from potential energy is more accurate. But again, as a consequence of the real dynamics of the particles which go above the barrier with finite kinetic energy the obtained potential energy is slightly higher than the static Monte Carlo result. Only the fluctuations of the angular kinetic energy of the outer shell agree with equilibrium results for the height of the barrier for intershell rotation.

2.5 Single-electron control of cluster properties

2.5.1 Idea of device

As we know from the previous study the location of the phase boundary of the Wigner crystal in the density-temperature plane sensitively depends on the precise particle numbers. The temperature of orientational melting can differ in different clusters by many in some orders of magnitude $T_o = 3 \times 10^{-3}...10^{-12}$

[40, 46, 47]. Orientational stability of shells strongly depends on the filing numbers of the shells. The highest temperature of orientational melting was found for *magic* clusters. Especially high stability is found in the cluster with $N = 19$, which has the orientational melting temperature $T_o \approx 3 \times 10^{-3}$ ($\Gamma_o^{19} = 330$) only 2 times lower than the radial melting temperature $T_r = 6.5 \times 10^{-3}$ ($\Gamma_r^{19} = 155$). This is due to the fact, that the number of particles on the three shells is optimal for formation of a hexagonal lattice (Fig. 2.13, top left picture). On the other hand in non-magic clusters, which have noninteger ratio of particles on the neighboring shells, temperature of orientational melting turns out to be many orders lower than the temperature of radial melting. Especially interesting orientational instability has the cluster $N = 20$, for which $T_o^{20} = 2.9 \times 10^{-12}$ ($\Gamma_o^{20} = 3.4 \times 10^{11}$) and $T_r^{20} = 1.2 \times 10^{-2}$ ($\Gamma_r^{20} = 83$).

The right picture of Fig. 2.13 shows the phase diagram of the crystals $N = 19$ and $N = 20$. There are classical and quantum parts of the diagram. The classical part of the boundaries is given by lines with constant Γ with the corresponding values of coupling parameter (from top to bottom) Γ_r^{20}, Γ_r^{19}, Γ_o^{19}, Γ_o^{20}. The quantum part is given by lines with constants r_s (density) and was calculated using PIMC [40].

The presence of three regions on the phase diagram (completely ordered, fully localized electrons 'CO', orientational disordered 'OD' and radially disordered 'RD') and a large temperature range for magic and non-magic clusters can be observed also on the current spectra of inner and outer shells in magic clusters $N = 19$ and non-magic $N = 20$. The Fourier transformation of the angular currents of the cluster $N = 19$ is shown on the Fig. 2.14. At $\Gamma = 500$ there are only small angular fluctuations at two relative high frequencies ($\omega \approx 0.49$ and $2.1\,\omega_0$). At the temperature near radial melting (region 'OD'), the energy spectrum broadens at the lower peak and shifts to lower frequency. We see a growing low frequency part of the spectrum at $\omega \approx 0$, which corresponds to an excitation of the smallest eigenfrequency of shell rotation in agreement with the result of simulation by a modified Newton technique [44]. The maximum value of the inner shell spectrum in both cases is bigger than that of the outer shell.

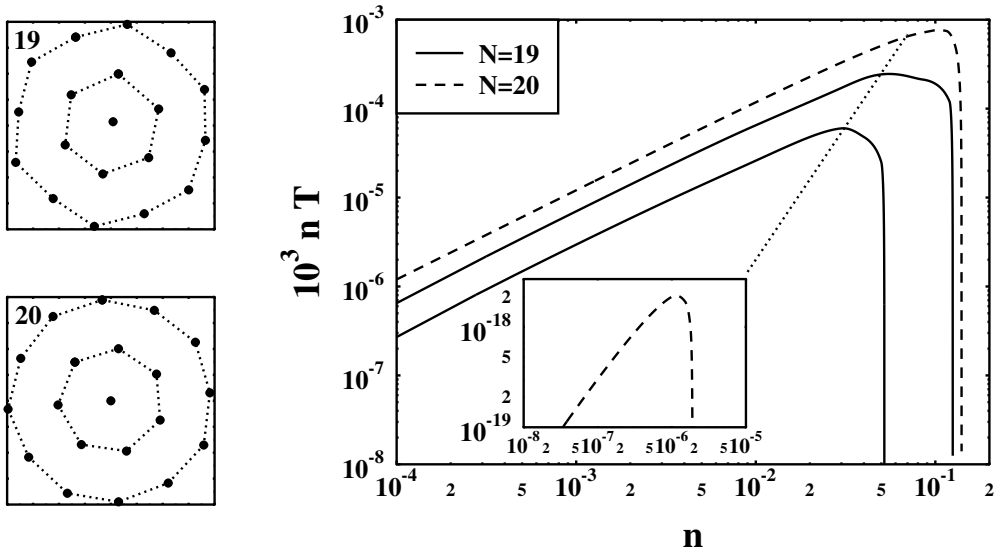

Figure 2.13: Ground state configuration of the 'magic' cluster $N = 19$ (top left) and $N = 20$ (bottom left) in the cluster plane. Each solid dot represents an electron. Right figure: Phase diagram of the Wigner crystal of 2D cluster with $N = 19$ and $N = 20$ electrons. The outer (inner) lines are the radial (angular) melting phase boundaries. The dotted diagonal line separates the classical (left) from the quantum (right) crystal. The dimensionless density and temperature are given by $n = r_s^{-1/2}$ and $T \equiv 1/\Gamma$.

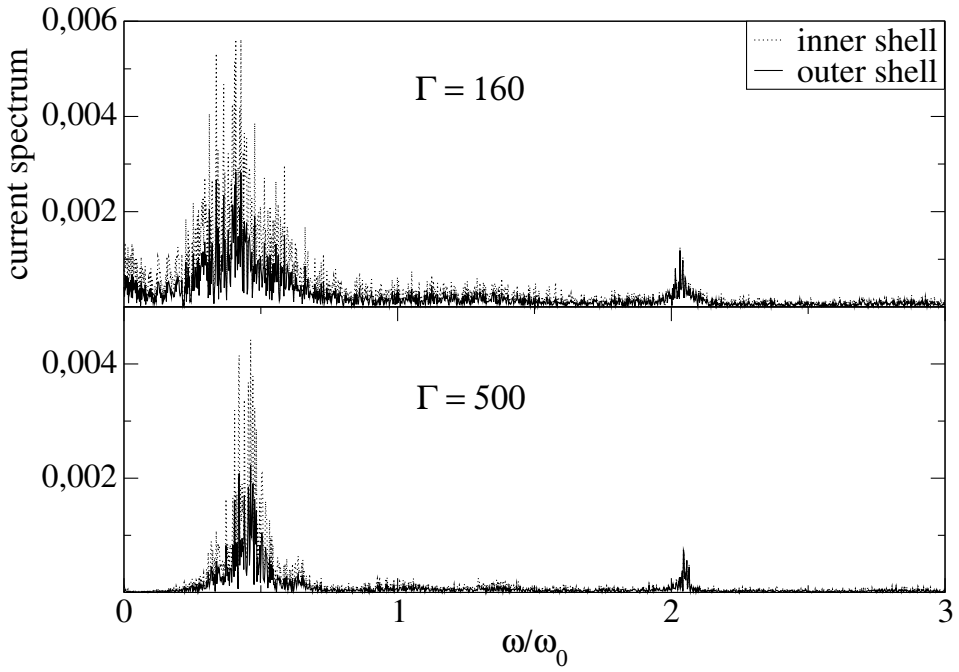

Figure 2.14: Spectrum of tangential current of inner and outer shells in cluster $N = 19$ for $\Gamma = 160$ (region of OM) and $\Gamma = 500$ (crystal phase).

At the same time cluster $N = 20$ at $\Gamma = 500$ and even at the lower coupling parameter $\Gamma = 100$ exhibits different behavior. Most of the energy is concentrated at low frequencies $\omega \simeq 0$, the rest is either smoothly distributed ($\Gamma = 100$) or concentrated at higher frequencies ($\omega \simeq 1.0$ and $1.85\ \omega_0$).

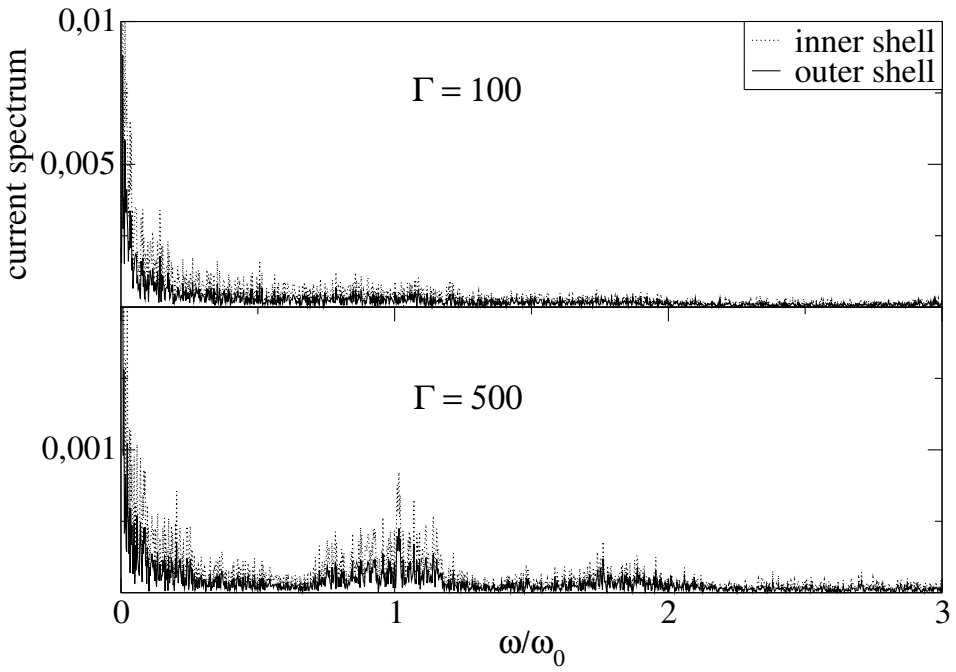

Figure 2.15: The same as in Fig. 2.14 for the cluster $N = 20$. Both coupling parameters correspond to the region of OM.

This behavior can be exploited for a non-traditional control of crystallization. In addition to changing temperature or/and density (confinement strength), crystallization in mesoscopic systems can be achieved by variation of the particle numbers *without a change of T and n.* For example, choosing a point in the temperature-density plane, Fig. 2.13, which is located between the radial (orientational) melting curves of $N = 19$ and $N = 20$ and switching between two particles numbers is equivalent to a crossover between crystal-like ('CO') and liquid-like ('OD'-'RD') behavior. We will demonstrate this below for the orientational melting curves in the classical part of the phase diagram, i.e. we fix the classical coupling parameter Γ between Γ_o^{20} and Γ_o^{19}, (see Fig. 2.13, right part). The main difference between the orientationally ordered (with $N = 19$) and disordered ($N = 20$) state will be that the latter is able to support inter-shell rotation excitations.

This should give rise to microscopic currents and magnetic fields. To estimate these effects, we compute the total angular current created by N electrons confined to one of M shells of radius R_k rotating with angular frequency ω_k(positive or negative depending on the directory) $I_\phi = e\sum_{k=1}^{M} N_k\omega_k R_k$. The associated magnetic field on the symmetry axis in a distance z above the cluster plane is directed normal to the plane: $B_z(z,\,t) = \mu e/2\sum_{k=1}^{M} N_k\omega_k(t)\left[1+(z/R_k)^2\right]^{-3/2}$. For example, for $N = 20$, we have $N_1 = 7$, $N_2 = 12$, $R_2 \approx 2R_1 \approx 2\cdot r_0$, so that $I_\phi^{20} \approx er_0(7\cdot\omega_1 + 24\cdot\omega_2)$. The relation between ω_1 and ω_2 depends on the excitation conditions. For example, if the total angular momentum of the excitation is zero, one readily finds $\omega_1/\omega_2 \approx -4N_2/N_1$, i.e. the inner shell rotates approximately seven times faster. Alternatively, rotation of some shells may be inhibited due to defects (pinning one or more particles).

2.5.2 Details of simulation

To verify this concept, described also in Ref. [48], let us consider the cluster with $N = 19$ in the ground state below the temperature of oriental melting T_o^{19}. The equilibrium state of the cluster was reached in the usual way using classical MD as described above. If we now apply a small external constant tangential force F_0^{ext} to all particles on the *outer* shell, the whole cluster will rotate due to strong intershell interaction. We can suppress the trivial rotation of the whole system pinning of one particle on the *inner* shell - this particle will be allowed to move only in a radial direction. If the external force F_0^{ext} is small enough (i.e. in the range of linear response and too small to overcome the intershell angular barrier, see Sec. 2.4.3), it causes angular excitations of shells: the outer shell will oscillate with some frequency depending on the value of F_0^{ext}.

Ground states of clusters $N = 19$ {1, 6, 12} and $N = 20${1, 7, 12} differ by one particle on the inner shell. So, if we insert one more particle on the inner shell to the cluster $N = 19$ we come near the equilibrium state for $N = 20$. This situation is shown on Fig. 2.16.

Such introduction is equivalent to a manipulation of the charge $e^{20}(t)$ of the inserted 20th particle: in the limit $t \to 0$ the particle charge is set to $e^{20}(t) \to 0$, for $t \to \infty$ the charge approaches the usual particle charge value, in our case $e^{20}(\infty) \to e_0$. During introduction of the particle the system will relax to its new equilibrium state. In case of momentary introduction of the particle

(time duration of insertion equal to zero) the whole cluster explodes, due to instantaneous overheating, where the temperature reaches a value much higher than the temperature of radial melting Γ_r^{20}. So, the law of changing the charge (or law of velocity of insertion of the particle) plays a crucial role in our simulation.

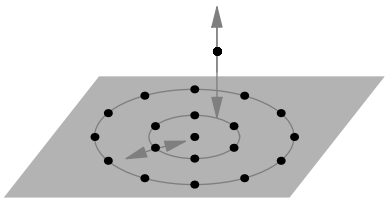

Figure 2.16: Schematic of the simulated cluster. On the inner shell of the cluster $N = 19$ one more particle is slowly inserted. To prevent rotation of the cluster as whole one particle on the inner shell (left particle) is pinned, it is allowed to move only radially.

We know that at big distance z between inserted particle and the cluster plane the inserted particle acts with force $F^{20} \sim z^{-2}$. If we choose velocity of inserted particle constant at the initial stage, then distance particle-cluster will be $z \sim t^{-1}$ and the force will be $F^{20} \sim t^2$. At beginning of particle introduction the particle charge will change as t^2 up to the time t_1. The main influence in particle charge looks like

$$e_1^{20}(t) = \frac{A\,(t/t_1)^2}{B + (t/t_1)^4}, \tag{2.24}$$

where $A = 0.2$ and $B = 4$ are coefficients. This is continued continue up to the time $t_1 = 5T_0$, the function $e_1^{20}(t)$ is shown on the Fig. 2.17 left part. On the next stage, which continues up to $t_2 = 1.5\,t_1$ the main contribution in the charge of inserted particle will have term $e_2^{20}(t)$, which has the form:

$$e_2^{20}(t) = 1 - e^{-t/t2}. \tag{2.25}$$

The resulting time dependence

$$e^{20}(t) = e_1^{20}(t) + e_2^{20}(t), \tag{2.26}$$

and also the function $e_2^{20}(t)$ are plotted on the right of Fig. 2.17. If the charge value exceeds the charge of any other particles, it is cut to the value e_0.

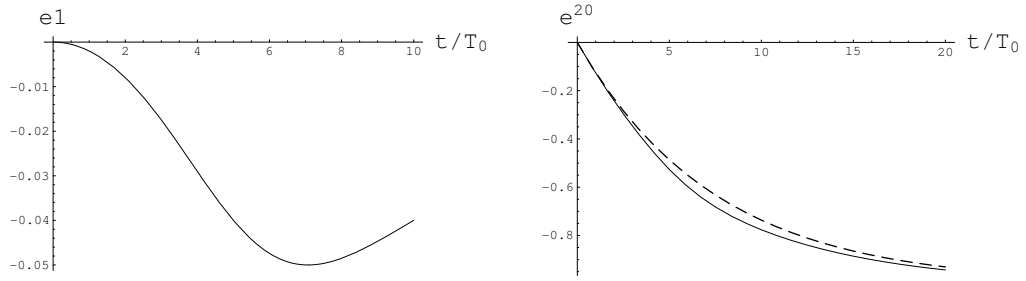

Figure 2.17: Time dependence of charge component $e_1^{20}(t)$ (Eq. 2.24) of the inserted particle (left) and component $e_2^{20}(t)$(dashed line on the right picture) as the resulting charge dependence $e^{20}(t)$(solid line on the right picture). Time in unit of T_0, charge in e_0.

During the time $[0,\, t_2]$ there is not any dynamics of the inserted particle in the cluster plane. The dynamic is turned on if time of introduction is more than $19\,T_0$(the particle has charge near e_0) and turned off if the charge becomes less than a quite small value, in our simulation $e^{20}(t) < 0.01 e_0$.

After the charge of the insert particle reaches the value e_0 the cluster $N = 20$ is in an excited state. Due to the lower value of the angular barrier the outer shell starts to rotate in the direction of the *external constant force* F_0^{ext}. The current and tangential kinetic energy are growing linear and quadratic with time, respectively. The whole kinetic energy also rises.

One possibility to prevent overheating and subsequent melting of the cluster is to remove the particle again. Analogously to the previous case we perform a slow change of the charge of the inserted particle from the inner shell in the opposite direction. In this case the functions e_1^{20} and e_2^{20} have the form:

$$e_1^{20}(t) = \frac{A\,[t_r - t/t_1]^2}{B + [t_r - t/t_1]^4}, \tag{2.27}$$

$$e_2^{20}(t) = 1 - e^{-(t_r - t\,C/t1)}, \tag{2.28}$$

where $A = 0.2$, $B = 4$ and $C = 1.5$. In these equations t_r is the staring of of the particle removal. To prevent rotation of the cluster $N = 19$ again, during the removal and after that we pinned one particle on the inner shell.

After removal of the particle the cluster $N = 19$ begins to relax to equilibrium state. The relaxation of radial and tangential kinetic energy of the outer shell is shown in the Fig. 2.18. During insertion from $t = 0$ to $t = 40\,T_0$ tangential kinetic energy grows quadratically and after removal from $t = 98\,T_0$ relaxes to equilibrium state. The kinetic energy starts to redistribute which leads to a decrease of $E_{k\phi}$ and an increasing of E_{kr}. In the equilibrium state both mean values are equal.

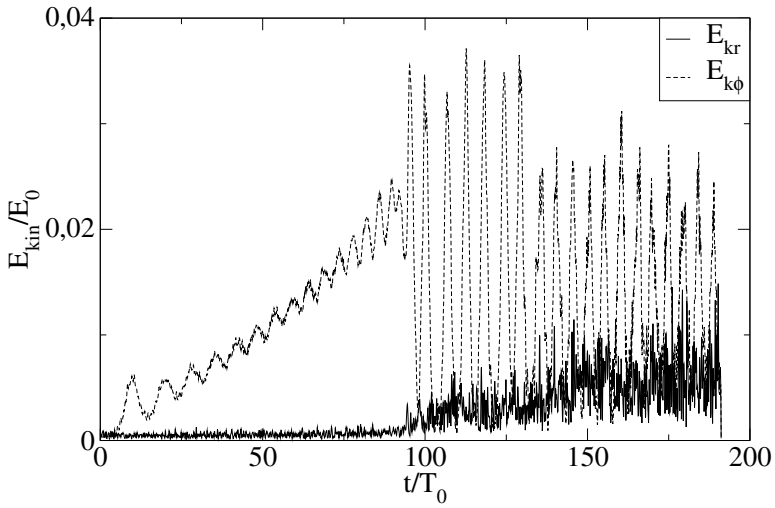

Figure 2.18: Radial and tangential energy of the outer shell during insertion and subsequental one particle operation. Insertion of the particle was terminated at $t \sim 40\,T_0$, removal ended at $t = 98\,T_0$.

As we see, the external tangential force F_0^{ext} acting on the outer shell leads to a strong heating of the outer shell. One possibility of preventing heating is to come back to the cluster $N = 19$ by removal of the inserted particle as just discussed. However, at the end the cluster remains in a state of increased kinetic energy corresponded to the initial state. Other possibility is immersion of the cluster in a viscous medium, which will absorb the energy. In a real experiment the particles also move in a medium with friction. In this case the equation of motion of the ith particle is modified to :

$$m_i \frac{d^2\mathbf{r}_i}{dt^2} = \mathbf{F}_i - \gamma m_i \mathbf{v}_i + \mathbf{F}_0^{ext}, \tag{2.29}$$

where the term $-\gamma m\mathbf{v}_i$ corresponds to linear viscous damping which transfer kinetic energy to the background, and $\mathbf{F}_0^{ext}$ is the tangential force, acting only on the particles of outer shell. It is clear that depending on the value of the friction coefficient the system will have different behavior. If the friction is too big, there is not any significant displacement of particles after insertion of the new particle and, vice versa if $\gamma = 0$ then we will get the usual MD simulation, as before. One can choose the friction coefficient γ small enough, that the emerging current of the outer shell in the cluster $N = 20$ will be approximately constant in time. In a real device this will correspond to an open state in the analogy to an open state of a diode, when it carries current. The second requirement to the medium is that the friction coefficient should be big enough to damp the spontaneous currents or oscillations in the cluster $N = 19$, appearing in the cluster after removal of the inserted particle. The quicker the system comes to the close equilibrium, the quicker the micro-device will be ready to reach the next 'ready-to-switch' state. This corresponds to the time between two subsequent switches. Of course this friction coefficient is a function of the external tangential force F_0^{ext}. In a real device the friction is determined by intrinsics processes. The is then to adjust the external force to the system. Here, we preliminarily want to demonstrate the principle functioning of such a device.

2.5.3 Results and discussion

Let us again consider cluster $N = 19$ in ground state configuration with initial coupling parameter $\Gamma_0 = 2 \cdot 10^4$, as depicted in Fig. 2.16. Now all particles will move according Eq.(2.29), where a weak external tangential force acts on the outer shell $F_0^{ext} = 2.158{\cdot}10^{-3}F_o$, $F_o = m_e r_o/T_0^2$. The charge of the inserted particle is increased beginning from $t_{in} = 70\,T_0$ according Eq.(2.26), than, from $t_{out} = 110\,T_0$ decrease according to Eqs.(2.27-2.28), and finally, after some equilibration time $t_{eqv} = 120\,T_0$, the insert-removal procedure is repeated.

Now there is not any velocity scaling applied, except for the new dissipative process - friction. The equations of motion were solved using the algorithm of Brownian dynamics with friction [59] and zero random noise.

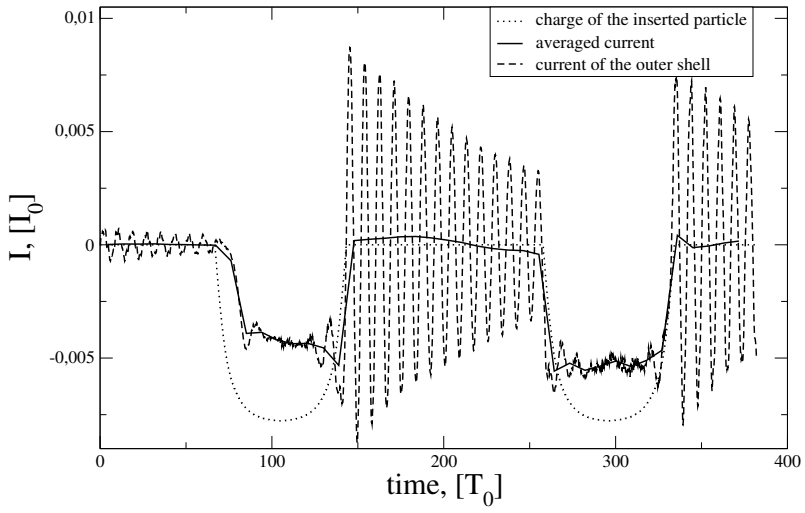

Figure 2.19: Dependence of the outer shell current on time. Average current as well as effective charge of the inserted particle are shown as well. Charge is in a.u. Unit of current is $I_0 = \frac{e_0 r_0}{T_0}$. Coefficient of friction in the simulated system is $\gamma = 0.0314\, T_0^{-1}$.

We have performed a series of simulations changing the friction coefficient from $\gamma = 3.14 \cdot 10^{-3}\, T_0^{-1}$ to $\gamma = 3.14\, T_0^{-1}$. We looked for the value γ, when we obtain an approximately constant current of the outer shell in cluster $N = 20$. The behavior of the system current with friction coefficient $\gamma = 0.0314\, T_0^{-1}$ is shown in Fig. 2.19. At the beginning tangential oscillations of particles on the outer shell decrease due to damping of medium. After increasing of charge of the inserted particle (which models the vertical distance of the change from the cluster plane) at time t_{in} the current starts to grow rapidly. When the charge becomes close to the charge of the other particles e_0, the current is almost constant. This means our "device" is in the open state, it is "conducting" an angular current (relative intershell current). We underline that the system is now not supporting intershell rotation, the high amplitude oscillation correspond to oscillation between neighboring potential barriers (which have a large height for $N = 19$, as was shown before). Still the system is far from a "closed" (nonconducting) state. One solution would be to wait until the oscillation decay to zero, but this would mean a low transient period which drastically reduces the speed of the device. A more

fruitful idea is to monitor not the instantaneous current but the time-averaged current.

After the charge is decreased again (the particle is removed) the system begins to equilibrate, and as result the momentary current oscillates with large amplitude. This amplitude exponentially goes down due to the damping. Fig. 2.19 also show the current, averaged over the time interval $9T_0$ (solid line) which remains almost zero and now more resemble a "closed " state of the device. The same behavior we observe during the second insert-removal cycle.

The average current clearly shows the desired step-like dependence. The "close" state of the device corresponds to the phase with zero (or near zero) *average* current, the "open" state - time with non zero value of the current (in our simulation $I_{max} \simeq 0.005\, I_0$). For practical application, the time of averaging in a real device limits the resolution ability for the measured properties, in our case this property is the current. Role of the external excitation F_o^{ext} could play also a constant or pulsed circularly polarized electric field.

Based on our simulation, we expect that the response of a (pinned) $N = 20$ cluster will be a nearly dissipationless rotation of the inner shell which stops after removal of one particle. Thus we may conclude that we have demonstrated the working principle of the device.

2.6 Summary

This chapter was devoted to a specific class of physical objects - spatially confined two-dimensional strongly coupled classical Coulomb clusters, consisting of a small ($N < 20$) number of particles. Such systems possess some interesting properties and can be investigated both in experiments and in computer simulation.

In our classical Molecular Dynamics simulations we studied the process of melting of such clusters in a real time. It was shown that the melting process consists of two stages: at a lower temperature the cluster undergoes orientational melting. In this phase region shells begin to rotate relative to each other. At a higher temperature, above the radial melting point, shells begin to exchange particles. Results of our classical MD simulations are in full agreement with the simulations Monte Carlo methods. However, in addition we have been able to study with realistic melting scenarios and its time dependences.

We have investigated the dynamics of the intershell rotation in *magic* clusters. Calculation of the intershell rotation barrier heights, in the example of the cluster $N = 12$ was performed using 3 different approaches. The response of the mesoscopic 2D cluster to an angular excitation was used as the main method of attack. reflected the existing real dynamics of the shell motion. Small overestimation of the values of the angular barrier found in the MD method reflects the existing real dynamics of the shell motion.

The existence of drastic differences in the angular melting properties of clusters $N = 19$ and $N = 20$ was used in the simulation of a single-electron device with controlled current of the outer shell. This allows for a completely new kind of single-electron controlled device. Such collective rotations of a group of electrons can be easily transmitted, e.g. in a system of multiple layers and may find applications for quantum computing. Naturally, realization of this concept will require very clean samples, and detection of the weak circular currents is another important issue to be solved. At the same time, high sensitivity of these few-electron clusters to very weak rotation excitation could be of interest for applications by itself.

Chapter 3

Dynamical Properties of one-component plasmas

3.1 Introduction

The plasma which we can observe in the universe usually has a much more complicated nature than the relatively simple two-dimensional clusters investigated in the previous chapter. It consists of a large number of particles. Such big systems have as a consequence many degrees of freedom, that make an accurate description of plasma a quite complicated task.

Secondly, depending on conditions, like density, temperature, pressure, chemical composition, the plasma is partially or fully ionized, processes of recombination and ionization proceed. On one hand, the long-range Coulomb potential is screened by the field of oppositely charged particles, on the another hand - the presence of the potential with a long range tail gives rise to new kinds of properties - collective excitations, which a play significant role in plasma.

In many instances, one can introduce and consider the model of a spatially homogeneous *one-component plasma* (OCP) for simplicity. It is a system consisting of a single species of charged particles embedded in a uniform background of neutralizing charges. Such an OCP is a substantially idealized model of a real plasma. The OCP model has - due to its simplicity- been widely investigated both theoretically and with various numerical and simulation methods, see e.g. [64–66] and [67, 68], respectively. Since the pioneering numerical work of Brush, Sahlin, Teller [69], the thermodynamic and dynamic characteristics of the classical OCP

have been studied in detail. In particular, the dependence of the properties on the coupling parameter $\Gamma = 4\pi e^2/(\bar{r}k_BT)$, where $\bar{r} = (\frac{3}{4\pi\rho})^{1/3}$ is the mean interparticle distance and ρ is the density, have been investigated up to very large values of Γ [70,71]. Among the most important thermodynamic results is the prediction of crystallization at values of Γ of the order of 172-180 [72–74,76]. An illustrative case of such crystallization is shown on Fig. 3.1. From classical MD simulation of Coulomb plasma, one sees the formation of a lattice of electrons order in the limit of high coupling parameter Γ on one hand and weakly correlated electron distribution in the Debye-Hückel limit Γ on the other. Furthermore, investigations of the dynamic properties of strongly correlated classical plasmas have indicated that the wave number dependent plasmon dispersion changes from monotonic growth, common for weakly coupled plasmas, to a decreasing dispersion around $\Gamma \approx 3$ [64].

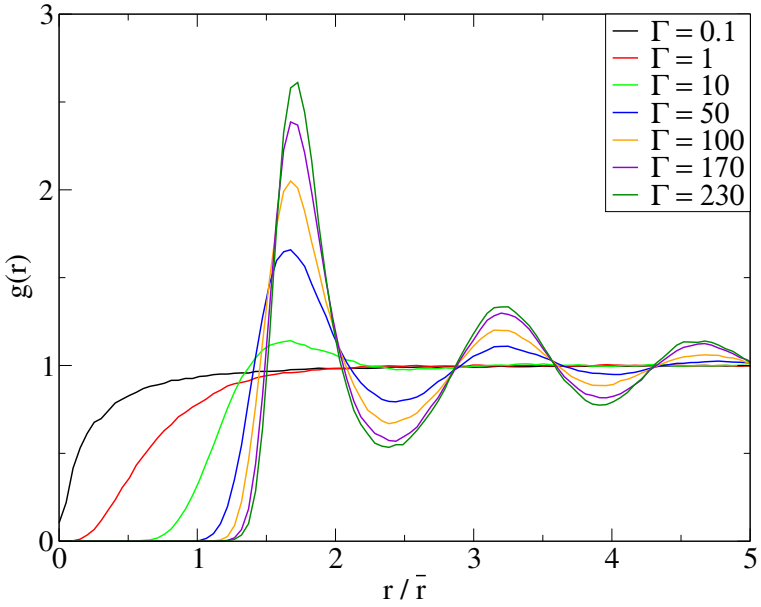

Figure 3.1: Pair distribution function of a classical electron Coulomb OCP. The simulations are performed in a system $N = 250$. Length of calculated distribution is limited by the half-length of the simulation box L. The details of the simulation are described below.

Furthermore, there is growing interest in the dynamic properties of dense *quantum* plasmas, in particular in astrophysics, laser plasmas and condensed

matter. While the case of strong degeneracy (strong quantum limit) and weak coupling at very high densities is well described by the random phase approximation (RPA, see e.g. [62, 77–80]), the properties at *intermediate coupling and degeneracy* remain poorly explored. Especially, one is interested in the dynamic plasma behavior in cases where the average kinetic energy is of the same order as the mean potential energy, i.e. $\Gamma \sim 1$, where collisionless theories such as the RPA fail, e.g. [78, 79, 81]. For these situations, quantum molecular dynamics (QMD) simulations [83] are the appropriate numerical approach which, however, is yet lacking the required efficiency. For weakly degenerate plasmas, with $\rho\Lambda^3 \leq 1$, where Λ is the De-Broglie wave length (see below), it is expected that one can perform much simpler classical MD simulations using effective quantum pair potentials, e.g. [66, 84–86]. These potentials can be derived from the 2-particle Slater sum using Morita's method. The Kelbg potential has recently been successfully used for path integral Monte Carlo simulations [87, 88]. There, it was found to give excellent results up to moderate degeneracy, $\rho\Lambda^3 \leq 5$ which lets us to expect reliable results also for MD simulations, at least for $\rho\Lambda^3 \leq 1$. It is the aim of this chapter to explore this MD approach with the Kelbg potential in detail, especially for the analysis of the optical (Langmuir) plasmon dispersion.

It is natural to start this analysis with OCP–simulations because they have the advantage of the absence of a collapse of oppositely charged particles at small distances. On the other hand, the existence of a homogeneous background of oppositely charged particles leads to some additional technical difficulties in comparison to 2-component systems, due to restricted carrier rearrangement causing less effective screening of the Coulomb interaction. One major problem of MD simulations of dynamical properties is that the behavior at small wave numbers is difficult to investigate. The reason is that large box-sizes are required which, for the analysis of high density plasmas, translates into large particle numbers. The current increase of available computer power gives one the possibility to investigate size-dependent properties like the density-density correlations $\langle \rho_{\vec{k}}(0)\rho_{-\vec{k}}(t)\rangle$ for smaller k-vectors than before. In this dissertation, we are able to present accurate results for the dynamical properties of the OCP, such as the dynamical structure factor and the wave vector dispersion of Langmuir oscillations. Our simulations for intermediate values of the coupling parameter, $\Gamma = 1 \ldots 4$, show an interesting dispersion: the frequency increases up to a maximum and, for

large wave numbers, decreases again. Further, we investigate the role of quantum effects by comparing simulations with the Coulomb potential and an effective quantum pair potential (Kelbg potential [84]) for the region of small and intermediate coupling. We find that quantum diffraction effects have a noticeable influence on the behavior of the optical dispersion curves. Increase of the degeneracy leads to a softening of the dispersion $\omega(k)$, especially at intermediate wave vectors.

3.2 Dynamical properties of the OCP

3.2.1 Statistical approach

A central quantity to determine the dynamic properties of charged many-particle systems is the frequency-dependent dielectric function $\epsilon(\vec{k},\omega)$ which, for the OCP, is given by

$$\epsilon(\vec{k},\omega) = 1 - U_C(\vec{k})\Pi(\vec{k},\omega). \tag{3.1}$$

Here $U_C(\vec{k})$ is the spatial Fourier transform of the Coulomb potential, $U_C(k) = 4\pi e^2/k^2$, and $\Pi(\vec{k},\omega)$ is the longitudinal polarization function. Thus, many-body effects enter the dielectric function via Π. There exist many approximations for the latter function - the simplest are mean-field theories which neglect short-range correlation effects, i.e. collisions between the particles.

In the first mean-field theory of Vlasov (1937), the classical kinetic equation for the distribution function $F(r,\, p,\, t))$ is used as the starting point of consideration. If one neglects fluctuations of microscopic density ρ, electric $\vec{E}$ and magnetic $\vec{B}$ fields then, we have a set of closed equations:

$$\frac{\partial F}{\partial t} + \vec{v}\frac{\partial F}{\partial \vec{r}} + (e\vec{E} + \frac{e}{c}\left[\vec{v}\times\vec{B}\right])\frac{\partial F}{\partial \vec{p}} = 0,$$

$$\mathrm{rot}\vec{B} = \frac{1}{c}\frac{\partial E}{\partial t} + \frac{4\pi e}{c}\int \vec{v}F(\vec{r},\,\vec{p},\,t)d\vec{p},$$

$$\mathrm{rot}\vec{E} = -\frac{1}{c}\frac{\partial \vec{B}}{\partial t},$$

$$\mathrm{div}\vec{E} = 4\pi e\int F(\vec{r},\,\vec{p},\,t)d\vec{p}, \tag{3.2}$$

where e is the charge of a particle. This approach is applicable for plasma in a

"collisionless" regime, because a collision term is absent on the r.h.s of the first equation in Eqs. 3.2, which would describe two and higher particle correlations in plasma. The last condition corresponds to a condition when the coupling parameter is much less than one, $\Gamma \ll 1$, or a hot dilute fully-ionized plasma.

For the classical OCP, the mean-field result is the Vlasov polarization function:

$$\Pi_{\text{Vlasov}}(\vec{k},\omega) = -\frac{1}{m}\int d^3v \, \frac{\vec{k}}{\omega - \vec{k}\vec{v} + i\delta}\frac{\partial F(\vec{v})}{\partial \vec{v}}. \tag{3.3}$$

Here $\delta \to +0$, indicating the retarded (causal) character of the polarization and the dielectric function. Further, $F(\vec{v})$ is the Maxwell distribution function:

$$F(v) = \frac{\rho}{(2\pi m k_B T)^{3/2}}\exp(-\frac{mv^2}{2\,k_B T}),\ \int d^3v F(\vec{v}) = \rho \tag{3.4}$$

The Vlasov polarization applies only to classical plasmas, where the quantum wave character of the particles can be neglected.

Quantum effects are important if the interparticle distance or the Debye radius become comparable to the De-Broglie wave length $\Lambda = h/\sqrt{2\pi m k_B T}$. Therefore, quantum diffraction effects should show up in the dielectric properties at large wave numbers. The Maxwell distribution Eq.(3.4) is the particular case of equilibrium distribution, if the Fermi energy E_F of particles is much less then thermal energy $k_B T$:

$$E_F = (2\pi^2)^{2/3}\hbar^2\rho^{2/3}/2m \ll k_B T. \tag{3.5}$$

In the case of a degenerate electron system one has to use the Fermi distribution function:

$$f(p) = \frac{2}{(2\pi\hbar)^3}\,\frac{1}{1+\exp((p^2/2m-\mu)/k_B T)}. \tag{3.6}$$

The quantum generalization of the Vlasov polarization is the RPA polarization function given by

$$\Pi_{RPA}(\vec{k},\omega) = -\int \frac{d^3p}{(2\pi\hbar)^3}\frac{f(\vec{p}) - f(\vec{p}-\hbar\vec{k})}{\hbar\omega + \frac{p^2}{2m} - \frac{(\vec{p}+\hbar\vec{k})^2}{2m} + i\delta}. \tag{3.7}$$

In this dissertation we consider only plasmas in equilibrium without external electric and magnetic fields, so F and f are the Maxwell and Fermi function, respectively. One readily confirms that, in the limit of long wavelengths, $\vec{k} \to 0$,

indeed the RPA result (3.7) goes over to the Vlasov polarization function (3.3). An important quantity which follows from the dielectric function (3.1) via the fluctuation-dissipation theorem is the dynamical structure factor $S(\vec{k},\omega)$

$$S(\vec{k},\omega) = -\frac{\hbar}{2\pi U_C(k)}\ \coth(\frac{\hbar\omega}{2k_BT}\hbar\omega)\ \mathrm{Im}\frac{1}{\epsilon(\vec{k},\omega)}, \tag{3.8}$$

which shows the frequency spectrum of density fluctuations for a given value of $\vec{k}$.

Very useful, exact relations are provided by the nth frequency moment sum rules for $S(\vec{k},\omega)$, which are expressed in terms of the quantities $< \omega^n(\vec{k}) >$, defined by

$$< \omega^n(\vec{k}) >= \int_{-\infty}^{+\infty} \omega^n S(\vec{k},\omega)d\omega. \tag{3.9}$$

The zero moment

$$< \omega^0(\vec{k}) >= S(\vec{k}) = \int_{-\infty}^{+\infty} S(\vec{k},\omega)d\omega \tag{3.10}$$

is called static structure factor, which is directly connected with the pair distribution function $g(\vec{r})$:

$$S(k) = 1 + \rho \int_0^{+\infty} \exp(-i\vec{k}\vec{r})\,[g(\vec{r}) - 1]\,r^2 dr. \tag{3.11}$$

The static structure factor describes the spectra of density fluctuations in the wave-vector space. In the Debye-Hückel limit for an isotropic system $S(k)$ reads

$$S_{DH}(k) = \frac{k^2}{k^2 + 3\Gamma.} \tag{3.12}$$

The second and third lowest-order sum rules obeyed by $S(\vec{k},\omega)$ are [93]

$$< \omega^2 >= \int_{-\infty}^{+\infty} \omega^2 S(\vec{q},\omega)d\omega = \frac{q^2\omega_{pl}}{3\Gamma} = \omega_0^2, \tag{3.13}$$

$$< \omega^4 >= \int_{-\infty}^{+\infty} \omega^4 S(\vec{q},\omega)d\omega = \frac{\omega_{pl}^4}{3\Gamma}\,(\frac{q2}{\Gamma} + q^2 - 2q^2 I(q)), \tag{3.14}$$

where $\vec{q} = \bar{r}\,\vec{k}$, $\omega_{pl} = \sqrt{4\pi e_0 \rho/m}$ is the plasma frequency and

$$I(q) = \int_0^{+\infty} \frac{1}{r}\,[g(r)-1]\left(\frac{\sin qr}{qr} + \frac{3\cos qr}{(kr)^2} - \frac{3\sin kr}{(kr)^3}\right) dr$$

for isotropic systems.

As mentioned above, the mean field expressions (3.3) and (3.7) neglect short-range correlations and are, therefore, valid only for weakly coupled plasmas, $\Gamma \ll 1$. There exist many theoretical concepts to go beyond the RPA which are based on quantum kinetic theory, density functional theory and other approaches. This is beyond the scope of this dissertation, see e.g. Ref. [78,79,81] and references therein. Here, we consider the alternative approach to the OCP at finite coupling which is based on molecular dynamics simulations.

3.2.2 Molecular dynamics approach to the dynamical properties

The dielectric and dynamical properties of an interacting many-particle system are easily accessible from the density-density correlation function which is defined as

$$A(\vec{k},t) = \frac{1}{N}\langle \rho_{\vec{k}}(t)\rho_{-\vec{k}}(0)\rangle, \tag{3.15}$$

where N is the number of particles. $\rho_{\vec{k}}(t)$ is the Fourier component of the density,

$$\rho_{\vec{k}}(t) = \sum_{i=1}^{N} e^{i\vec{k}\vec{r}_i(t)}, \tag{3.16}$$

which is computed from the trajectories $\vec{r}_i(t)$ of all particles. The dynamical structure factor is just the Fourier transform of the density-density correlation function (3.15)

$$S(\vec{k},\omega) = \frac{1}{2\pi}\int_{-\infty}^{+\infty} dt\, e^{i\omega t}\, A(\vec{k},t). \tag{3.17}$$

For the correlation function Eq. (3.15) which can be expanded in the series

$$A(\vec{k},t) = A(\vec{k},0) + \frac{t^2}{2!}\frac{\partial^2}{\partial t^2}A(\vec{k},0) + \frac{t^4}{4!}\frac{\partial^4}{\partial t^4}A(\vec{k},0) + \ldots \tag{3.18}$$

the Fourier transformation is an even function of ω and the odd moments are all zero. The sum rules Eq. (3.13-3.14) are related to zero-time derivatives in the expansion (3.18) by [82]

$$< \omega^{2n} >= (-1)^n \frac{\partial^{2n}}{\partial t^{2n}} A(\vec{k}, 0) = \frac{1}{2\pi} \int_{-\infty}^{+\infty} \omega^{2n} S(\vec{k}, \omega) d\omega. \tag{3.19}$$

Equation (3.17) can be directly compared to formula (3.8) and, thus, allows for a comparison of the simulation results with the statistical theories. Furthermore, Eq. (3.17) allows to investigate the influence of quantum effects on the dynamical properties and plasmon dispersion of the OCP. Variations of the interaction potential (see below) directly affect the particle trajectories and, via Eqs. (3.15)–(3.17), the dynamical structure factor.

3.3 Details of the MD-simulations

The simulations have been performed in a cube of length L containing N interacting electrons on a uniform positive background. For this system, we solved Newton's equations of motion containing all pair interactions which are derived from a total potential $U(r)$, see below. As an algorithm of motion we used a second-order scheme in form of the Swope algorithm [60]. Since our simulations are performed in the microcanonical ensemble, the mean kinetic energy may change. Therefore, to maintain the chosen value of temperature and Γ, we applied scaling (renormalization) of all velocities at every second step.

A central goal of our simulations was to study the influence of quantum effects. We therefore performed several simulations which used either a Coulomb potential or an effective quantum pair potential (see below). To permit flexibility in the use of the potential, U was divided into a short-range and a long-range part, $U = U^{\rm sr} + U^{\rm lr}$, where quantum effects influence only $U^{\rm sr}$, whereas the behavior at large distances, $U^{\rm lr}$, is dominated by the long-range Coulomb interaction. Let us first describe the treatment of the long-range term.

3.3.1 Long-range interaction

The long-range interaction was computed in a standard way using periodic boundary conditions and the Ewald summation procedure [90, 91]. As a result, the long-range potential is given by the Coulomb interaction in the main box and all image cells:

$$U^{\mathrm{lr}}(\vec{r}) = 4\pi e^2 \sum_{i \neq j}^{N} V_{\mathrm{ewald}}(\vec{r}_{ij}), \tag{3.20}$$

$$V_{\mathrm{ewald}}(\vec{r}) = \sum_{\vec{n}=0}^{n_x,n_y,n_z \leq 3} \frac{\mathrm{erfc}\left[\sqrt{\pi}|(\vec{r}+\vec{n}L)/L\right]}{|\vec{r}+\vec{n}L|} + \sum_{\vec{n}\neq 0}^{n_x,n_y,n_z \leq 5, n^2 \leq 27} \frac{\exp(-\pi n^2)\cos(2\pi \vec{n}\vec{r}/L)}{\pi n^2 L} - \frac{1}{L} \quad , \tag{3.21}$$

where erfc is the complementary error function, L - the side length of the simulation cell and $\vec{n}$ - a vector of integer numbers which labels the periodic images of the simulation box. In this expression, the first term corresponds to a potential of particles with Gaussian broadened charge distribution around the electrons with a width of $\sqrt{\pi}$, the second term - the compensating Gaussian distributions, and the last accounts for the influence of the homogeneous background. It turns out that the second term in (3.20) can be reduced to 2 loops (one over the particles and one over the vectors $\vec{n}$ in the reciprocal space) and is not very time consuming. The more complicated part is the first term which contains three loops (one is over vector $\vec{n}$ and two are over all pairs of particles). In case of a two-component plasma, a proper choice of the width of the Gaussian distribution and use of periodic boundary conditions greatly simplifies this term due to cancellations. In contrast, for an OCP, the background cancels the interactions only partially, "statically". As a result, convergence of the sum is worse, and one needs to take into account all first neighboring image cells (total of 26) at every time step. The contribution of all neighboring cells except for the main one ($0 < |\vec{n}| \leq \sqrt{3}$) was computed before the start of the simulations and stored in 3-dimensional tables for the potential and forces. During the simulations, we used 3D-bilinear interpolation at every step to obtain the values of the potential and forces for intermediate distances. We found that 100 grid points in every direction are adequate, so the total size of the table was 10^6 elements. The particle

interactions inside the main ($\vec{n} = 0$) cell were evaluated directly at every time step without minimum image convention.

3.3.2 Short-range interaction. Quantum effects

Let us now discuss the short-range potential. As has been shown by Kelbg and co-workers [84, 89], quantum effects can be treated efficiently by an effective pair potential, the Kelbg potential:

$$U_{\text{kelbg}}(r,T) = 4\pi e^2 \left(\frac{1-\exp(-r^2/\lambda^2)}{r} + \frac{\sqrt{\pi}}{\lambda}\text{erfc}(r/\lambda) \right), \tag{3.22}$$

where $\lambda = \frac{\Lambda}{\sqrt{2\pi}}$. As a consequence of quantum effects, this potential differs from the Coulomb potential at small distances $r \leq \lambda$ and is finite at $r = 0$. Further, it is temperature-dependent via the thermal De-Broglie wavelength. The Kelbg potential can be regarded as the proper quantum pair potential following from the two-particle Slater sum S_2 without exchange effects:

$$\ln S_2 = -\frac{U_{\text{kelbg}}}{kT} + O(\Gamma^2). \tag{3.23}$$

It treats quantum diffraction effects exactly, up to first order in Γ. Frequently other quantum pair potentials have been used, including the Deutsch potential [92], which has the same value at $r = 0$ but differs from the Kelbg potential at intermediate distances. As was mentioned by Hansen [93], symmetry effects do not have a big influence on the dynamical properties (although they give a major contribution to the static properties, especially for the light mass components). Using the Kelbg potential (3.22), we can immediately separate the short-range part of the interaction,

$$U^{\text{sr}}(r,T) = 4\pi e^2 \left(\frac{-\exp(-r^2/\lambda^2)}{r} + \frac{\sqrt{\pi}}{\lambda}\text{erfc}(r/\lambda) \right), \tag{3.24}$$

which has been calculated together with the first sum of Eq. (3.21) using the interpolation table.

The Kelbg potential contains just the lowest order quantum corrections (lowest order in e^2) and is, thus, accurate at small coupling, $\Gamma < 1$. Nevertheless, we expect that it correctly reproduces the influence of quantum effects also at

intermediate coupling, $\Gamma \leq 5$, which is also motivated by its successful use in quantum Monte Carlo calculations [87, 88], see above. Further improvements are straightforward, e.g. by including exchange effects or by evaluating the full two-particle Slater sum. The corresponding results will be presented in chapter 4. We note that the described numerical procedure of lookup tables applies to such improved quantum pair potentials as well, even if they are not given analytically.

3.3.3 Thermodynamic and dynamical quantities

Solving Newton's equations with forces derived from the total potential $U^{\rm sr}+U^{\rm lr}$, we computed the thermodynamic and static quantities, such as the total energy and the pair distribution function in usual manner. The results will be presented in the next section. Here we discuss some details of computation of the dynamical properties, as they require much more effort and computation time in order to achieve sufficient accuracy.

To obtain useful results for the dynamical structure factor, requires simulations in a sufficiently broad range of wave numbers and frequencies. Natural units of the wave number and frequency are $1/\bar{r}$ and the plasma frequency $\omega_{pl} = \sqrt{4\pi e^2\rho/m}$, respectively, which will be used in the following. The minimum possible wave number k_{min} depends on the size L of the simulation box and thus, for a given density or coupling parameter, on the number of particles N. One readily verifies that $k_{min} = 2\pi/L = 2\pi(\rho/N)^{1/3}$ or, using dimensionless wave numbers, $q_{min} = k_{min}\bar{r} = (6\pi^2/N)^{1/3}$. Clearly, to reduce k_{min} requires an essential increase of the number of particles in the simulation.

The simulation accuracy can be further increased by taking advantage of the isotropy of the plasma in wave vector space. Indeed, in equilibrium, the density-density correlation function and dynamical structure factor should only depend on the absolute value of the wave vector. On the other hand, the simulations yield slightly different results for different directions of the wave vector. Averaging all results corresponding to the same absolute value of $\vec{k}$ allows reduction of the statistical error. For example, the minimum wave number k_{min} corresponds to directions of $\vec{k}$ along either the x-, y- or z-axis, cf. Eq. (3.16), so we can use the average of the three. The next largest value is $\sqrt{2}\,k_{min}$, corresponding to the diagonals in the x-y, x-z and y-z planes. The third value, $\sqrt{3}\,k_{min}$, corresponds to the space diagonal and is not degenerate; consequently it carries the largest

statistical error. This is the main reason for the fluctuations of the numerical results for the wave vector dispersion, see for example Fig. 3.7.

Finally, to resolve the collective plasma oscillations, the duration of the simulations has to be much larger than the plasma period. Also, increased simulation times leads to a reduction of the noise. We found that times of the order of 250 plasma periods are adequate.

3.4 Numerical Results

We have performed a series of simulations for varying values of Γ and $\rho\Lambda^3$, using the Coulomb and Kelbg potential. Also, time step and particle number have been varied until a satisfactory compromise between accuracy and simulation efficiency was achieved. The parameters of the runs chosen for the figures below are summarized in Table 3.1. We mention that kinetic energy conservation in all runs (if velocity scaling was turned off) did not exceed 0.1%. Also, the results for the total energy (not shown), in case of the Coulomb potential, agree very well with data from the literature.

Γ	$\rho\Lambda^3$	$\rho(cm^{-3})$	$T\,(10^4)$	$\omega_{pl}(fs^{-1})$	$r_D/\bar{r}$	N	$k_{min}\bar{r}$	(T_{pl})
0.5	0.1	$9.12{\cdot}10^{21}$	11.26	5.387	0.816	500 (250)	0.491 (0.619)	515 (341)
0.5	0.5	$2.28{\cdot}10^{23}$	32.92	26.940		400 (250)	0.529 (0.619)	429 (429)
1.0	0.1	$1.14{\cdot}10^{21}$	2.228	1.905	0.577	250	0.619	290 (327)
1.0	0.5	$2.85{\cdot}10^{22}$	8.23	9.524		250	0.619	682 (682)
1.0	1.0	$1.14{\cdot}10^{23}$	1.31	19.048		250	0.619	477
4.0	0.1	$1.78{\cdot}10^{19}$	0.176	0.238	0.289	250	0.619	570 (227)
4.0	1.0	$1.78{\cdot}10^{21}$	0.817	2.381		250	0.619	716

Table 3.1: Parameters of the molecular dynamics simulations with the Kelbg potential. Numbers in parentheses refer the runs with Coulomb potential.

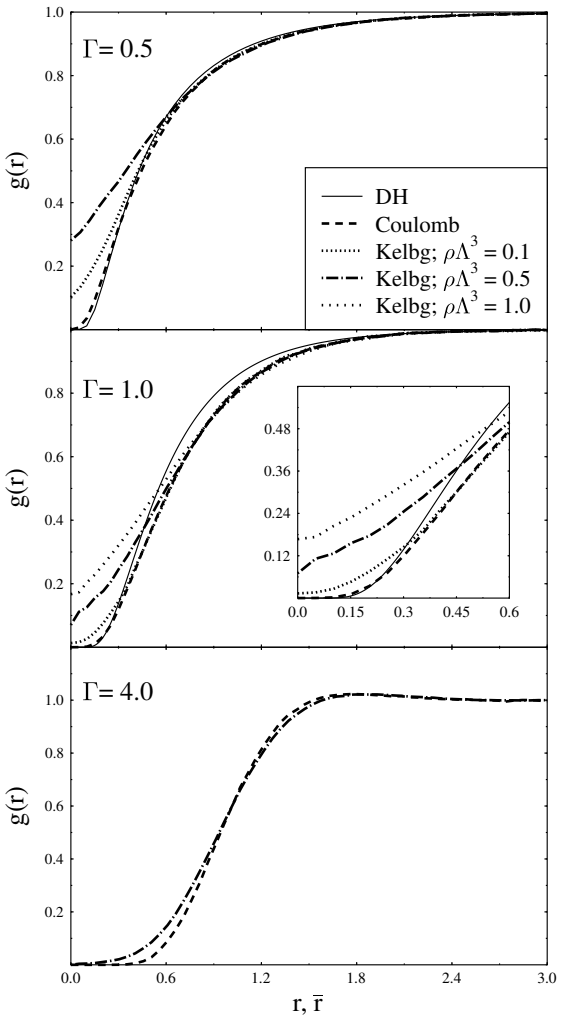

Figure 3.2: Pair distribution functions for Γ= 0.5 (upper figure), Γ= 1.0 (middle figure), 4.0 (lower figure), and $\rho\Lambda^3 = 0.1$, 0.5, 1.0 for systems with Coulomb and Kelbg potential. Further, the Debye-Hückel (DH) limit (Eq. 3.25) is shown (solid line). Line styles are the same in all three figures. Inset in the middle Fig. shows the influence of the degeneracy at small distances. The results for $\Gamma = 4.0$, $\rho\Lambda^3 = 0.1$ with Kelbg potential are not distinguishable from the Coulomb result and are not plotted.

We first consider the pair distribution function $g(r)$ for varying interaction potentials and parameter values. Fig. 3.2 shows $g(r)$ for three values of the coupling parameter, $\Gamma = 0.5$, 1, 4.

As expected, the Coulomb pair distribution function is close to the Debye-

Hückel limit

$$g_{DH}(r) = 1 - \Gamma \exp(-r/r_D) \tag{3.25}$$

for small coupling, with increasing Γ, the deviations, especially around $r = \bar{r}$, grow systematically. The Kelbg pair distributions practically coincide with the Coulomb functions for $r > 0.6\,\bar{r}$ but deviate from the latter at small distances of the order of the thermal De-Broglie wave length Λ where quantum effects are important.

Clearly, with increasing degeneracy, the ratio $\Lambda/\bar{r}$ increases, and the deviations extend to larger distances and grow in magnitude. With increasing Γ, the deviations become smaller since Coulomb effects dominate the behavior at small distances.

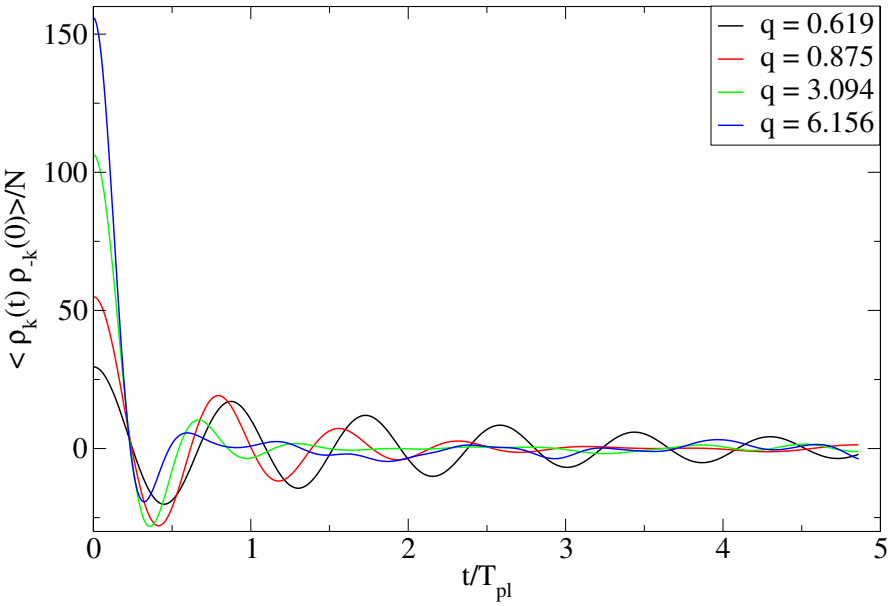

Figure 3.3: Density-density correlation functions for four wave vectors $q = 0.619$, 0.875, 3.094 and 6.156 in OCP with Kelbg potential, $\Gamma = 1$ and $\rho\Lambda^3 = 0.1$. Unnormalized auto-correlation functions are averaged over all possible spatial directions. q is in units of $\bar{r}$.

Let us now turn to the dynamical properties. In case of an OCP, charge and mass fluctuations are identical because of the rigid oppositely charged background. In our simulations, we have calculated the density-density correlation function (Eq. 3.15). Typical behavior of the density-density auto-correlation function at different wave vectors is shown on Fig. 3.3. The appearance at large times of oscillations at a frequency close to ω_{pl} is an indication of the collective density

fluctuations or plasmon. The dynamical structure factor $S(q,\omega)$ for several (from 6 to 10, depending on the simulation) wave numbers was obtained by numerical Fourier transformation . The values of wave vectors are determined by the size of the simulation box L (see above). The value of the smallest wave number is given in Table 3.1.

The frequency dependence of $S(q,\omega)$ for several wave vectors is presented in Figs. 3.4, 3.5, 3.6 for the Coulomb and Kelbg potentials. Also, the results of the mean-field models are shown.

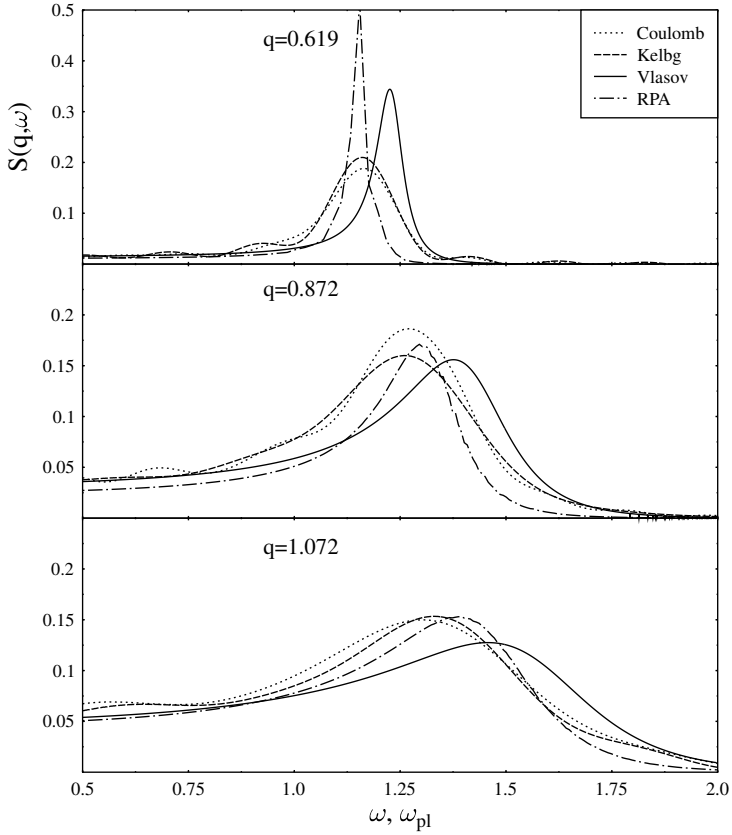

Figure 3.4: Dynamic structure factor for an OCP at $\Gamma = 1$ and $\rho\Lambda^3 = 0.1$ from MD simulations with Coulomb and Kelbg potentials. In addition, Vlasov and RPA results are shown. The wave numbers are shown in the figures in units of $\bar{r}$, i.e. $q = k\bar{r}$.

The peak of the structure factor is related to the optical plasmon (Langmuir mode) of the electrons, its position shows the plasmon frequency $\Omega(k)$, its width - the damping of the mode. In the limit $k \to 0$, $\Omega(k) \to \omega_{pl}$ for all models. For increasing wave numbers, the width of the peak grows steadily, and it merges with

the continuum of single-particle excitations, e.g. [62, 79], therefore, no results for larger wave numbers are shown.

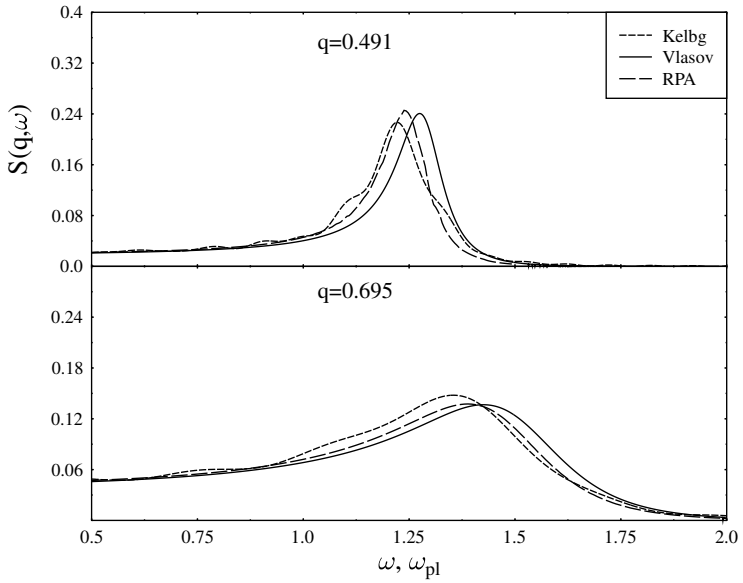

Figure 3.5: Same as Fig. 3.4, but for $\Gamma = 0.5$ and $\rho\Lambda^3 = 0.1$. The values of the wave numbers differ from Fig. 3.4 due to the different particle numbers, cf. Table 3.1.

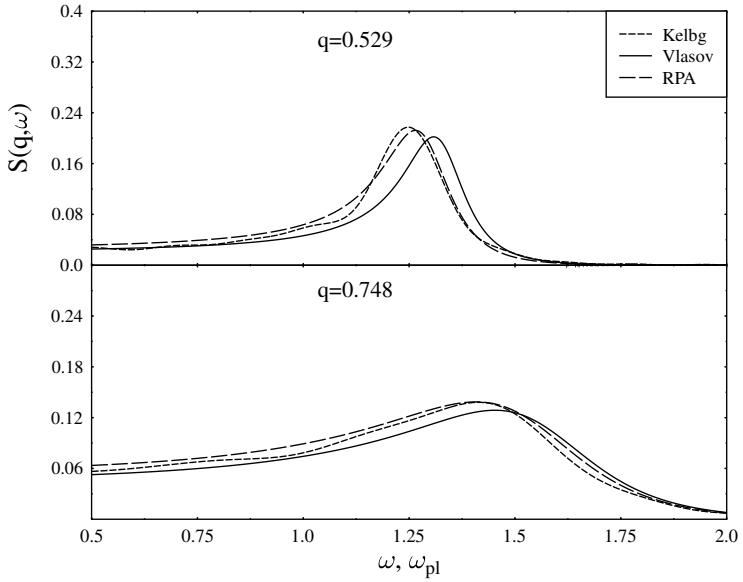

Figure 3.6: Same as Fig. 3.5, but for $\rho\Lambda^3 = 0.5$.

Consider now the results for the plasmon dispersion in more detail, cf. Fig. 3.7.

First, we discuss the mean field results (3.8) which are calculated using the Vlasov and RPA polarizations, Eqs. (3.3) and (3.7), respectively. The Vlasov result was computed using the formulas given in the review of Kugler [94]. In this approximation $S(q,\omega)$ takes the form

$$S^{vlasov}(q,\omega) = \frac{S_0(q,\omega)}{\left[1 - U_C(q)\Phi(z)\right]^2 + \left[\omega\pi U_C(q) S_0(q,\omega)\right]^2}, \tag{3.26}$$

where $U_C(q)$ is Fourier transformation of the Coulomb potential, divided by $k_B T$, $z = (3\Gamma/2)^{1/2}\omega/q$, and

$$\Phi(z) = 2z\, I_D(z) - 1,$$

where

$$I_D(z) = \exp(-z^2) \int_0^z \exp(t^2) dt,$$

is Dawson's integral.

In the limit $\Gamma \to 0$ the dynamic structure factor goes to its ideal-gas limit $S_0(q,\omega)$, given by

$$S_0(q,\omega) = \left[\frac{3\pi\Gamma}{2}\right]^{1/2} \frac{1}{q} \exp\left[-\frac{3\Gamma\omega^2}{2q^2}\right], \tag{3.27}$$

where ω is expressed in units of the plasma frequency.

For computation of the RPA results, a code was used which accurately evaluates the pole integration in Eq. (3.7), [95]. Both approximations show the same general trend for small and intermediate wave numbers: with increasing wave number, the plasmon frequency and the damping increase. At large q, the dispersion exhibits a maximum and decreases again. In all situations, the RPA yields a slightly smaller frequency than the Vlasov result, whereas the damping values are very close to each other.

Let us now turn to the simulation results. The Coulomb and Kelbg simulations have been performed for exactly the same parameters, except for N and run time (cf. Table 3.1). (Notice that, in contrast to the Kelbg case, the Coulomb simulations depend only on Γ which can be achieved by various combinations of density and temperature). Comparison of the two simulations shows, cf. Fig. 3.4, that the results for the structure factors are very similar in the case of small Γ.

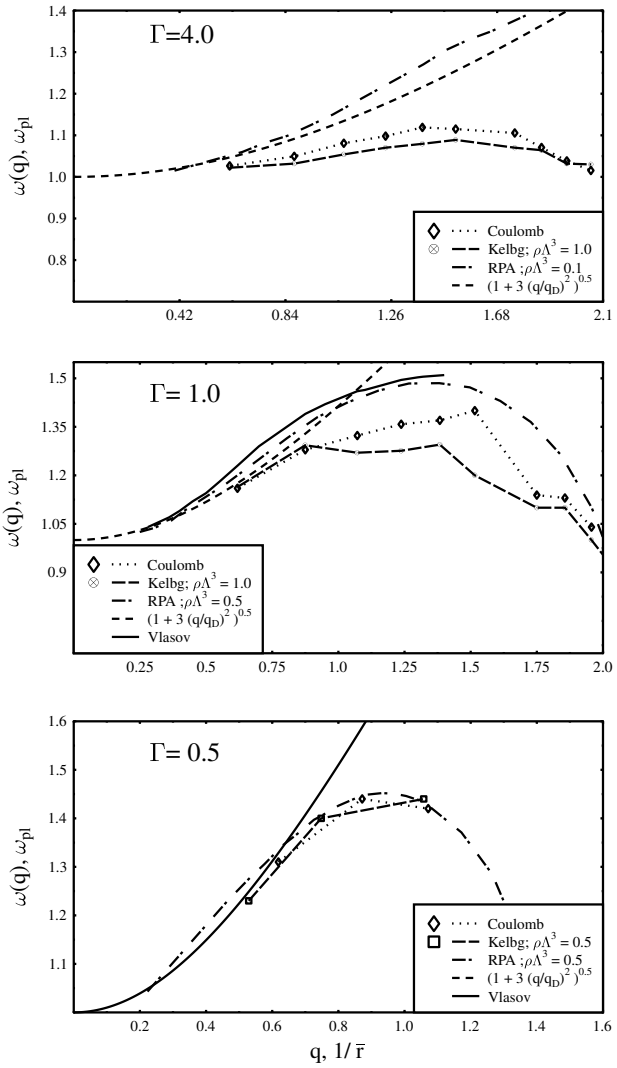

Figure 3.7: Optical plasmon dispersion for various coupling and degeneracy parameters from MD simulations with Coulomb and quantum potentials. Also shown are results of the Vlasov and RPA approximations, and of the analytical approximation of Eq. (3.28). For $\Gamma = 4.0$ and $\rho\Lambda^3 = 0.1$ (upper graph) the MD simulations with Kelbg potential and the RPA curve are not shown since they almost coincide with the Coulomb simulation and the Vlasov curve, respectively.

Peak positions and widths as well as the low and high frequency tails are very close to each other. The reason is obvious: since the potentials (and pair distributions, cf. Fig. 3.2) differ only at small interparticle distances of the order of Λ, differences in the structure factor would show up only at $k > 2\pi/\Lambda$, which

is about an order of magnitude larger than the wave numbers shown in Fig. 3.4. There, the plasmon peak has already a width of the order of the frequency and no longer describes a well-defined collective excitation.

q	$<\omega^0>$	$<\omega^0>_{MD}$ [93]	$<\omega^0>_{MC}$	$<\omega^2>$	$<\omega^2>_{MD}$ [93]	$q^2/(3\Gamma)$
0.619	0.109	0.112	0.118	0.159	0.144	0.129
0.875	0.210	0.188	0.216	0.266	0.241	0.257
1.072	0.281	0.296	0.300	0.342	0.405	0.386
1.857	0.620	0.602	0.612	1.120	0.979	1.158
2.315	0.717	0.702	0.739	1.561	1.084	1.80
3.094	0.832	0.680	0.876	2.170	1.183	3.214
6.156	0.650	-	0.994	2.259	-	12.72

Table 3.2: Comparison of zeroth and second moments of $S(q,\omega)$ from MD runs of Coulomb OCP with $\Gamma = 0.993$ with classical MC structure factors [64], other MD simulations and with the exact value of the second moments (Eq. 3.13). Zeroth moment $<\omega^0>$ is equal to static structure factor (Eq. 3.10) if we take the upper integration limit $t = +\infty$.

Simulation results for zeroth and second moment sum rules are listed in Tab. 3.2 for OCP Coulomb plasma with $\Gamma = 0.993$. The presented results are generally in good agreement with two lowest sum rules Eq. (3.9). For most wave vectors (except the smallest, $q = 0.619$) both sum rules are in better agreement with classical MC simulations than analogous MD runs from Ref. [64]. The reason is that we used sufficiently longer time length to calculate the density-density correlation function Eq. (3.15). Deviations for vectors $q = 0.619$ and 1.072 from MC results are connected with an applied filter procedure in Fourier-Laplace transformation. In the case of the smallest wave vectors, when damping is relatively small, we have divided the oscillating signal $A(q,\, t)$ into two components: one fits $A(q,t)$ with function $f(t) = a{\cdot}\cos(b\cdot t)\exp(-c\cdot t)$ where a, b, c are fitting parameters, and the reminder $A(q,t) - f(t)$. After summation of the numerical Fourier transformation of the reminder and analytical Fourier transformation of $f(t)$ we have smoothed spectrum of function $A(q,\, t)$ with the correct limit value of $S(q,\omega)$ under $\omega \to 0$. However this filtering procedure introduces some distortions in the final spectrum. For the largest q the calculated moments do not

reflect the accuracy of MD simulation since part of the high-frequency tail of $S(q,\omega)$ was not included.

It is now interesting to compare the simulation results to the theoretical approximations. The first observation is that the simulation peaks are significantly broader, cf. Fig. 3.4. This is obvious since the simulations fully include interparticle correlations missing in the mean-field results. Consequently, the plasmon damping contains collisional damping in addition to the Landau damping (which is the only damping mechanism in the mean-field models). Correspondingly, the plasmon peaks in the simulations are shifted to smaller frequencies. This effect grows with increasing wave number as well as with increasing coupling (see also Fig. 3.7). We note that, in our simulations, this shift is observed for all wave numbers, which is in contrast to the result of Hansen [see Fig. 9 of Ref. [93] for $q = 0.6187$]. In other words, the plasmon dispersion curves from the MD simulations are lower than the mean-field result for all wave vectors $\vec{k}$, which is seen more clearly in Fig. 3.7. As expected the MD curves for the structure factor are much closer to the RPA than to the Vlasov result.

In Fig. 3.7 we plot the optical plasmon dispersion curves for three values of the coupling parameter for the Vlasov and RPA dispersions together with the simulation results. Further, we show the well-known analytical approximation to the Langmuir dispersion in the classical limit,

$$\omega(q) = \omega_{pl}\left(1 + \frac{q^2}{\Gamma}\right)^{1/2}. \tag{3.28}$$

Clearly, this predicts a monotonically increasing dispersion. However, this approximation is valid only for $k < 1/r_D$ and for $\Gamma < 1$. Let us now consider the simulation results which do not have this limitation. In Fig. 3.7 we show the MD results for a Coulomb potential and for the Kelbg potential for three values of the degeneracy parameter, $\rho\Lambda^3 = 0.1,\ 0.5,\ 1.0$. One clearly sees that, for these parameters, the dispersion is positive, $d\omega(q)/dq > 0$, up to wave numbers of the order of one over the mean interparticle distance. For larger q, the dispersion changes its sign. This general trend is observed for the Coulomb and the Kelbg potential. On the other hand, with increasing quantum effects, $\rho\Lambda^3$, the deviations between the two potentials are growing. This becomes more pronounced as Γ increases, cf. the curves for $\Gamma = 1$ and $\Gamma = 4$: the dispersion in case of the

Kelbg potential shows a softer increase with increasing wave number and reaches a lower maximum approximately at the same wave number as in the Coulomb case. We mention that this sign change of the dispersion has not been reported by Hansen [64]. Comparing the simulations with the mean-field results, we again see that the MD dispersions proceed lower than the mean field results, and this effect grows with increasing Γ and increasing wave number.

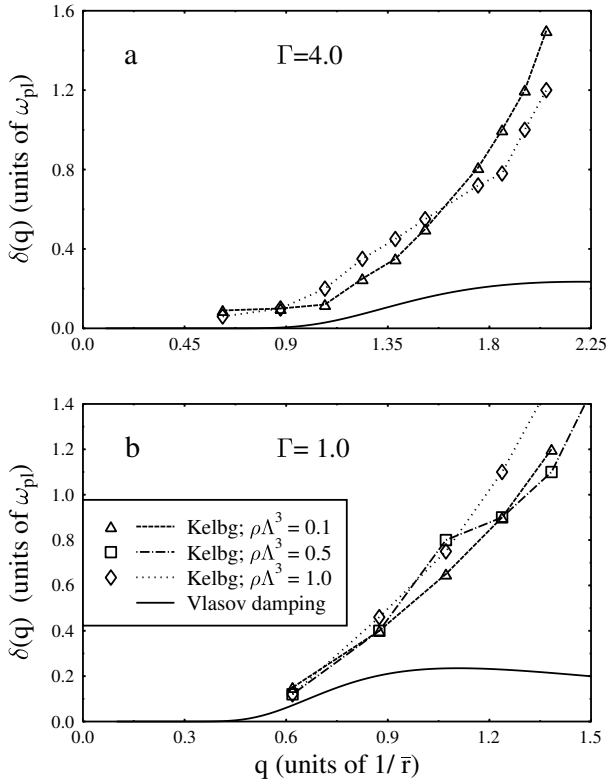

Figure 3.8: Damping of Langmuir waves from MD simulations with the Kelbg potential for various values of Γ and $\rho\Lambda^3$. Solid lines represent the analytical small damping limit of the Vlasov theory, Eq. (3.29).

Once more, we confirm that the RPA dispersion is much closer to the MD result than the Vlasov dispersion, at least for $\Gamma \leq 0.5$. [As mentioned above, the simulation results for the dispersion show certain statistical fluctuations due to the varying accuracy of the results for the different wave numbers].

Let us now consider in more detail the plasmon damping. Fig. 3.8 shows the damping (full width at half maximum of the plasmon peak of the structure factor) as a function of a wave number. It is interesting to compare with the

familiar analytical expression from the Vlasov theory, e.g. [96],

$$\delta(\kappa) = \sqrt{\frac{\pi}{8}} \frac{\sqrt{1+3\kappa^2}}{\kappa^3} \exp(-(2\kappa^2)^{-1} - 3/2), \tag{3.29}$$

where $\kappa \equiv kr_D$ is the dimensionless wave number in units of the inverse Debye radius r_D given in Table 3.1. Formula (3.29) is derived under the condition that the damping is much smaller then the frequency [$\delta(q) \ll \omega(q)$], and is limited to small wave numbers $\kappa \ll 1$. As expected, the damping given by formula (3.29), which is only Landau damping, is much smaller than the damping found in the simulations, as the latter contain the full collisional damping also. Obviously, for small coupling and small q, Eq. (3.29) shows the correct trend. However, deviations increase rapidly with growing coupling parameter. Furthermore, the simulations which are not limited to small wave numbers, show a qualitatively different behavior at large q: a monotonic increase of the damping. Interestingly, with increasing Γ the damping is reduced, cf. Figs. 3.8 a,b.

Γ	$\rho\Lambda^3$	a	b
1.0	0.1	1.013±0.031	-0.260± 0.023
1.0	0.5	1.074±0.041	-0.288±0.013
1.0	1.0	0.975±0.055	-0.259±0.018
4.0	0.1	0.169±0.015	-0.035±0.006
4.0	1.0	0.121±0.007	-0.025±0.003

Table 3.3: Fit parameters of the Langmuir dispersion relation curves shown on Fig. 3.9. The fit equation was taken in the form of $\omega(q)/\omega_{pl} = (1 + a\,q^2 + b\,q^4)^{1/2}$. Parameters of the fit for $\Gamma = 1$ and $\rho\Lambda^3 = 0.1$ are less reliable, because of the absence of data for big wave vectors, cf. Table 3.1.

Finally, we try to extend the analytical result for the plasmon dispersion, Eq. (3.28), to a higher Γ and to include quantum effects. For this purpose, we used the MD data with the Kelbg potential to construct an improved fit of the form $\omega(q) = \omega_{pl}\,(1 + aq^2 + bq^4)^{1/2}$. The result is shown in Fig. 3.9 for $\Gamma = 1$ and $\Gamma = 4$.

Due to the large fluctuations in the dispersion data and the increasing damping for large wave numbers, we used a weighted fit where the smallest $q-$values had the largest weight and the statistical errors of the individual points have been taken into account. Table 3.3 contains the resulting fit parameters. According

to this data both parameters a and b depend on Γ and $\rho\Lambda^3$. The parameter a is close to $1/\Gamma$ in agreement with Eq. (3.28), but with increasing Γ, deviations are growing, compare with Table 3.3. We see no systematic influence of quantum effects on the parameter a for $\Gamma = 1$. Noticeable effects show up for $\Gamma = 4$, where increased degeneracy leads to a reduction of the coefficient a. The second fit parameter allows to qualitatively reproduce the change of the sign of the dispersion. The overall agreement is satisfactory for wave numbers up to the inverse mean interparticle distance where the plasmons are comparatively weakly damped.

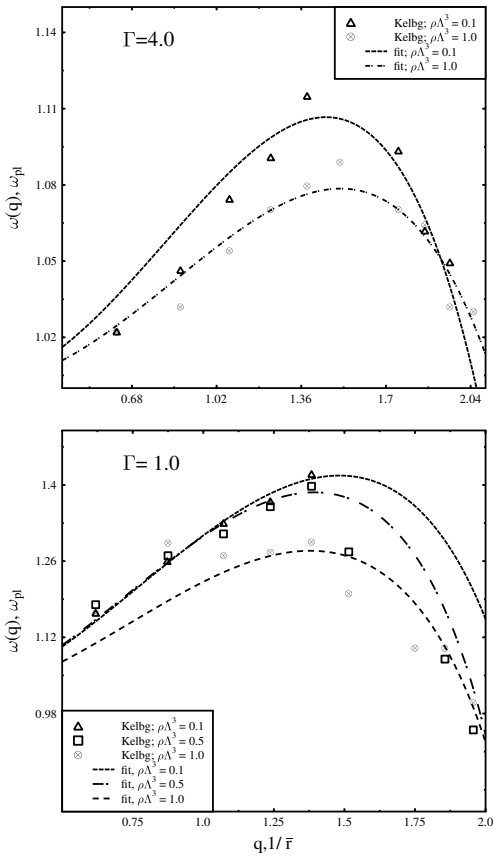

Figure 3.9: Dispersion of Langmuir oscillations from MD simulations with the Kelbg potential for various values of the coupling and degeneracy. Symbols are MD results, lines the best fits to the low wave number part ($q < 1/\bar{r}$). The fit formula and parameters are given in Table 3.3.

3.5 Conclusion

We have presented extensive classical molecular dynamic simulations of the dielectric properties of a one-component plasma at intermediate coupling and degeneracy, $\Gamma \leq 4$ and $\rho\Lambda^3 \leq 1$. The main conclusion is that increase of coupling and degeneracy influence the dispersion in similar way: they reduce the plasmon frequency. The physical reason is simple: with increasing Γ, the Coulomb interaction is screened more and more. Thus the binary interaction is dominated by short-range effects which tend to soften the collective mode. Similarly, increase of the degeneracy leads to a growth of the electron wave length which, again, increases the efficiency of short-range binary interaction.

While classical MD simulations can be extended to arbitrary large values of Γ, they have limited applicability to quantum plasmas. We used, as an effective quantum pair potential, the Kelbg potential which rigorously describes quantum diffraction effects in an equilibrium plasma for small Γ. On the other hand, the Kelbg potential is only the first term of a Γ expansion for an effective quantum pair potential, and for $\Gamma > 1$ the account of higher order corrections to the quantum diffraction effects may become important. Nevertheless, we found that the plasmon dispersion is rather weakly influenced by the details of the pair potential, so we expect that the Kelbg potential correctly reproduces the dynamic properties of a weakly degenerate plasma also for intermediate values of Γ. The main advantage of using the Kelbg potential is that it correctly treats close collisions, i.e. the two-particle scattering a inter-particle distances smaller than the De-Broglie wavelength. This is of even higher importance in the case of two-component plasmas where the Kelbg potential allows to avoid the collapse of oppositely charged particles. This is demonstrated below in next chapter.

Chapter 4

Simulation of partially ionized dense hydrogen plasma with improved Kelbg potentials

4.1 Introduction

The OCP model, considered in the previous chapter for electron gas, is a useful but too simple model to describe a real plasma. We know that the assumption of a uniform neutralizing background charge, used in the OCP, is not adequate in most real plasmas. Only in some special cases, for example, at very high density, when electron temperature is very high, protons start to build a crystal lattice. At such conditions, one can consider a movement of protons on an opposite charged background of electrons, spread in the space as in the OCP.

In a region of medium density, which is considered here, heavy particles also take part in many processes and have big influence on the light-mass subsystem via collisions. The more complicated the compound of the plasma is and the smaller the differences in mass of the interacting particles are, the more complicated the picture and the dynamics of matter become. In a hydrogen plasma, which will be consider now, a mass ratio is $m_i/m_e \simeq$ 1836 in comparison with semiconductors, where this value is about 1...100. Despite the quite big mass ratio, a role of protons is very important due to formation of *bound states* with electrons. These bound states (atoms, molecules and their radicals) change different properties of plasma, comparing with the OCP plasma. That is a main reason

why an explicit treatment of all components is needed to correctly simulate even a plasma of the simplest element of the periodic table.

Classical MD simulations of dense two-component hydrogen plasmas have been performed by many authors before. To overcome the problem of collapse of an electron into a proton, arising from the divergence of the electron-proton Coulomb potential at zero distance, one introduces some effective quantum potentials. In the simulation these potentials should not only prevent any collapse but also correctly, in principle, reproduce the formation of bound states. These potentials can be derived from different theoretical approximations and usually involve only the dependence on the interparticle distance and the temperature of the components. Most of these methods are based on perturbation expansion in the coupling strength and are limited to regions of small coupling parameter ($\Gamma < 1$) and small degeneracy ($k_B T > E_F$). Another important simplification is the reduction of the many-body problem to two-particle correlations.

In the present work we apply, for the first time, a new effective quantum potential based on Kelbg potential (Eq. 3.22) in classical Molecular Dynamics simulations, which includes in addition to quantum diffraction effects also *spin effects*. Similarly to our previous investigations of the OCP in chapter 3, in this chapter we will investigate the following questions:

- the influence of the coupling parameter Γ and the degeneracy parameter $\rho\Lambda^3$ on the structure properties of hydrogen plasma;
- electron-electron and proton-proton density-density correlation functions;
- the influence of the coupling parameter Γ and the degeneracy parameter $\rho\Lambda^3$ on dynamic properties of dense hydrogen plasmas in particular on the dispersion and damping of Langmuir waves;
- spin-spin density correlations in the hydrogen plasma in the absence of the external magnetic field;
- boundaries of applicability of the improved Kelbg potential in semiclassical Molecular Dynamics simulations.

The results of these simulations are compared with corresponding simulations of an OCP, which give us more understanding of both models.

4.2 Improved Kelbg potential

We start with a discussion of the improved quantum pair potential. The Kelbg potential (KP) was described before in Sec. 3.3.2. Its main defect is incorrect value at $r = 0$. As a consequence, the KP becomes increasingly inaccurate with increasing Γ. Improved Kelbg potentials (IKP) use the suggestion ([97] and references therein), that the form of the real interaction can be expressed by the usual Kelbg potential (Eq. (3.22)) with an additional free parameter γ_{ij}:

$$U^{IKP}(r_{ij,}, T) = \frac{e_i e_j}{r_{ij}} \left[1 - \exp(-r_{ij}^2/\lambda_{ij}^2) + \frac{\sqrt{\pi} r_{ij}}{\lambda_{ij}\gamma_{ij}} \mathrm{erfc}(\gamma_{ij} r_{ij}/\lambda_{ij}) \right]. \tag{4.1}$$

Similar to the OCP, the De Broglie wavelength for a particle pair i, j is $\lambda_{ij}^2 = \frac{\hbar^2\beta}{2\mu_{ij}}$ with $\mu_{ij}^{-1} = m_i^{-1} + m_j^{-1}$. Allowing for the dependence $\gamma_{ij}(T)$ one can obtain a correct zero-point value of the potential (Eq. (4.1)). Here by "correct" value we mean a good quantitative agreement with the 'exact' pair potential value, obtained from the analytical Slater sum $Sl(r_{ij}, T)$ for the two-particle interaction

$$Sl(T)_{r_{ij}=0} = \exp(-\beta U_{ij}(T)_{r_{ij}=0}). \tag{4.2}$$

The temperature fit of the parameters $\gamma_{ij}(T)$ was performed on the data of inter-particle potentials from Path Integral Monte Carlo (PIMC) simulations, based on the exact binary density matrix [98]. It was found that the temperature dependence of γ_{ij} can be well described by the following Pade approximations

$$\gamma_{ep}(T) = \frac{x_1 + b_{ep} x_1^2}{1 + a_{ep} x_1 + b_{ep} x_1^2}, \tag{4.3}$$

$$\gamma_{ee}^{\uparrow\downarrow} = \frac{\gamma_{ee}^{\uparrow\downarrow}(T \to 0) + b_{ee} x_1^2}{1 + a_{ee} x_1 + b_{ee} x_1^2}, \tag{4.4}$$

where $x_1 = \sqrt{8\pi k_b T/Ha}$, one Hartree $[Ha]$ is 2 Ry= 315775 K. Best fit coefficients are the following: b_{ep}= 1, b_{ee} = 1, a_{ep}= 1.10, a_{ee}= 0.180. The limit $\gamma_{ee}(T \to 0)$ has been found by evaluating the zero temperature limit of $Sl_{ee}^{\uparrow\downarrow}$ at $r_{ee} = 0$, which for two electrons with anti-parallel spins [28] is given by

$$Sl_{ee}^{\downarrow\uparrow}(r_{ee} = 0) = 4\sqrt{\pi}\xi_{ee} J_1(\xi_{ee}), \tag{4.5}$$

where the interaction parameter $\xi_{ij} = e_i e_j \beta / \lambda_{ij}$ and

$$J_1(\xi) = \int_0^\infty x \exp(-x^2) \left[1 - \exp(-\pi\xi/x)\right]^{-1} dx.$$

The zero temperature limit of $\gamma_{ee}^{\downarrow\uparrow}$ can be written as

$$\gamma_{ee}^{\downarrow\uparrow}(T \to 0) \approx -\frac{2}{\sqrt{\pi}} \widetilde{x}^3 \left[\ln(\widetilde{x}^4/\sqrt{\pi}) - 3\widetilde{x}^2\right]^{-1}, \tag{4.6}$$

with $\widetilde{x} = (\pi \mid \xi \mid /2)^{1/3}$.

For electrons with parallel spins the coordinate part of the two-electron wave function must be anti-symmetric. The corresponding effective quantum potential has to be defined as

$$\exp(-\beta U_{ee}^{\uparrow\uparrow}) = \chi_{cm}(\mathbf{R}, \mathbf{R})\{\chi(\mathbf{r}, \mathbf{r}) - \chi(\mathbf{r}, -\mathbf{r})\},$$

where χ_{cm} is the free particle density matrix in the coordinate system of the center of mass, $\mathbf{R} = (m_i \mathbf{r}_i + m_j \mathbf{r}_j)/(m_i + m_j)$. Using for $\chi(\mathbf{r}, \mathbf{r})$ an expression for the two-particle density matrix from perturbation theory we get

$$\exp(-\beta U_{ee}^{\uparrow\uparrow}) \quad =$$

$$= \quad \exp(-\beta U_{\text{kelbg}}(\mathbf{r}, \mathbf{r})) - \exp(r^2/\lambda_{ij}^2) \exp(-\beta U_{\text{kelbg}}(\mathbf{r}, -\mathbf{r})). \tag{4.7}$$

Here $U_{\text{kelbg}}(\mathbf{r}, \mathbf{r}')$ is the result of first-order perturbation theory for Coulomb system

$$U_{\text{kelbg}}(\mathbf{r}, \mathbf{r}', \beta) = e_i e_j \int_0^1 \frac{d\alpha}{d_{ij}(\alpha)} \text{erf}\ (d(\alpha)/(2\lambda_{ij}\sqrt{\alpha(1-\alpha)})), \tag{4.8}$$

where $d_{ij}(\alpha) = \left|\alpha \mathbf{r}_{ij} + (1-\alpha)\mathbf{r}_{ij}^{-1}\right|$. The diagonal element ($\mathbf{r}_{ij} = \mathbf{r}'_{ij}$) of Eq. (4.8) is just the familiar Kelbg potential $U_{\text{kelbg}}(r, T)$, Eq. (3.22).

If the off-diagonal potential term $U_{\text{kelbg}}(\mathbf{r}, -\mathbf{r})$ in the expression for the effective potential (Eq. (4.7)) is approximated by its diagonal matrix element $U_{\text{kelbg}}(\mathbf{r}, \mathbf{r})$ then the effective potential for electrons with parallel spins reads

$$U_{ee}^{IKP\uparrow\uparrow}(r,T) = U_{\text{kelbg}}(r,T) - k_B T \ln(1-\exp(-r^2/\lambda_{ee}^2)). \tag{4.9}$$

As we see, the IKP differs from the KP at $r \to 0$ where the potential has a logarithmic divergency. This reflects the Pauli principle for electrons with parallel spins.

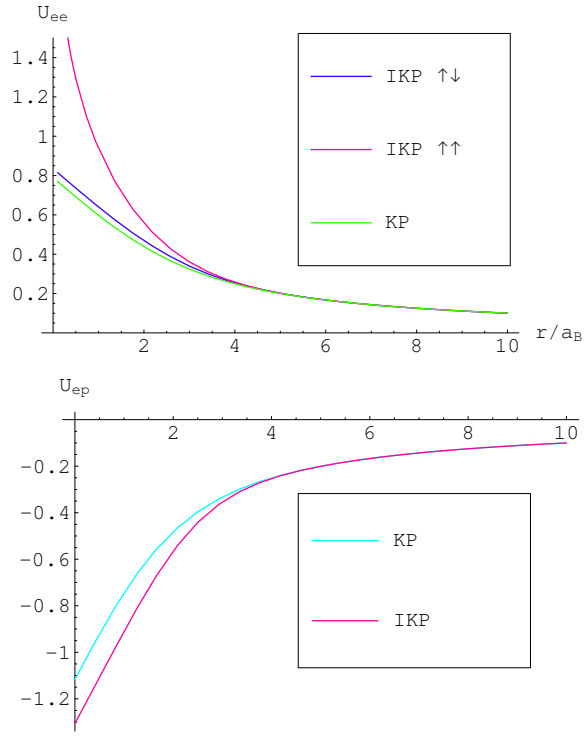

Figure 4.1: Electron-electron (top) and electron-proton (bottom) improved Kelbg potential (IKP) at T= 62500 K. The Kelbg potential (KP) is also plotted. The e-e potential is shown for parallel (IKP $\uparrow\uparrow$) and anti-parallel (IKP $\downarrow\uparrow$) spins. The potentials are given in the units of $k_B[Ha]$.

In Fig. 4.1 the behavior of the electron-electron and electron-proton improved Kelbg potential (IKP) at $T = 62500\,K$ is shown together with the usual Kelbg potential. The proton-electron IKP has a bigger absolute value at $r = 0$ in comparison with the Kelbg potential and will give a tighter binding of an electron and proton. In contrast to this, the e-e potential shows more repulsion even for electrons with anti-parallel spins, electrons with parallel spins can not overlap at all due to the divergency of the potential at zero distance (Pauli principle).

We underline that this set of e-e potentials correctly accounts for the spin pro-

jections of the interacting particles and allow for the inclusion of spin-dependent effects which is important, in particular, in the presence of a magnetic field. In our simulation we will investigate a plasma without external magnetic field, e.g. without spin-flip processes, but this model should be capable to describe related phenomena as well.

4.3 Details of numerical simulation

As an object of simulation we have chosen a dense partially ionized plasma of the first element of the periodic table – hydrogen. For such a plasma there are many theoretical and numerical results, for example [21, 26, 28, 99], the hydrogen plasma has been simulated in a wide range of the density-temperature plane, so we can compare results of our MD simulations to variety of data.

As in the OCP case, we have performed a series of simulation runs of hydrogen plasmas in the most interesting range of coupling parameters Γ and degeneracy parameters $\rho\Lambda^3$ around 1. We add also phase points with $\Gamma = 0.1$ to see the low-coupling limit of this model. The parameters of the MD simulations are displayed in Tab. 4.2.

Γ	$\rho\Lambda^3$	$\rho_e(cm^{-3})$	$T\,(10^4\mathrm{K})$	$\omega_{pl}(fs^{-1})$	$\triangle t\, T_{pl}$
0.1	0.1	$1.14{\cdot}10^{24}$	281.4	60.23	0.03
0.1	0.5	$2.85{\cdot}10^{25}$	823	301.17	0.03
0.5	0.1	$9.12{\cdot}10^{21}$	11.26	5.387	0.03
0.5	0.5	$2.28{\cdot}10^{23}$	32.92	26.94	0.03
1.0	0.1	$1.14{\cdot}10^{21}$	2.228	1.905	0.08
1.0	0.5	$2.85{\cdot}10^{22}$	8.23	9.524	0.08
1.0	1.0	$1.14{\cdot}10^{23}$	13.1	19.048	0.08

Table 4.2: Parameters of MD simulations of a hydrogen plasma with IKP. ρ_e is the total density of the electron component.

The time step $\triangle t$ was chosen according to analogous simulations of a TCP with the Deutsch potential [99]. In simulation the maximum time length of correlation functions is limited by memory of computer. This maximum length

is proportional to the time step and should be as big as possible to get good numerical results for spectrum of the correlation functions. On the one hand we should take $\triangle t$ as big as possible, on the other hand a smaller time step guarantees a smaller round-up error in the numerical integration of the equations of motion. The compromise values of time steps for every run are listed in Tab. 4.2.

The simulation box in all these cases has the length $L = ((N_p+N_e^{\downarrow}+N_e^{\uparrow})/\rho)^{1/3}$, ρ is the total density of the plasma, $\rho = \rho_p + \rho_e^{\downarrow} + \rho_e^{\uparrow}$, and contains $N_p = 512$ protons, $N_e^{\downarrow} = 256$ electrons with spin down and an equal number of electrons $N_e^{\uparrow}$ with spin up. We keep the condition of overall electroneutrality by taking $N_p = N_e^{\uparrow} + N_e^{\downarrow}$. The scheme of integration of the equations of motions was the same as in the OCP case.

For interaction between electrons and protons, protons with protons and electrons with anti-parallel spins, we have used the IKP (Eq. 4.1) with the fit parameters given by Eqs. (4.3) and (4.4), respectively. The interaction between electrons with parallel spin projections is described by Eq. (4.9).

To properly account for the long-range character of the potentials, we used the standard Ewald procedure. In contrast to the OCP case, in the TCP we have "dynamic" screening of the Coulomb interaction and we can restrict ourself to the first term in the potential energy sum in Eq. (3.21), i.e. the main cell ($\vec{n} = 0$). That leads to the usual Minimum Image Convention in the main box. The parameter α in Eq. (3.21) was taken as $5.6/L$, the sum in the reciprocal space (second term of Eq. (3.21) was calculated with 5 vectors in all directions. This gives some computational-cost advantage compared with the OCP simulation.

Because of the temperature-dependent potentials we applied a temperature scaling at every time step for all components separately (for protons and two sorts of electrons) to guarantee an equality of the temperatures of all components in equilibrium simulations.

For each simulation the systems were equilibrated for at least 10^4 steps of molecular dynamics. The equilibrium states were identified by a saturation of the change of the potential energy in time. The maximum fluctuation of potential energy in simulations of systems with medium coupling ($\Gamma \geq 0.5$) was 4.29%, in weakly coupled systems ($\Gamma = 0.1$) it reached 25.5% because of the very high ratio of mean kinetic/potential energies and temperature scaling. The length of productive runs in equilibrium was $1.1{\cdot}10^5$ steps for all these phase points.

4.4 Results of simulations

4.4.1 Static properties of hydrogen plasma

An important static property in MD simulations is the pair-correlation or radial distribution function $g_{ij}(r)$ which measures the probability to find the particles i and j at a distance r. In MD the maximum length of the calculated pair distribution function is restricted by the half-length of the box.

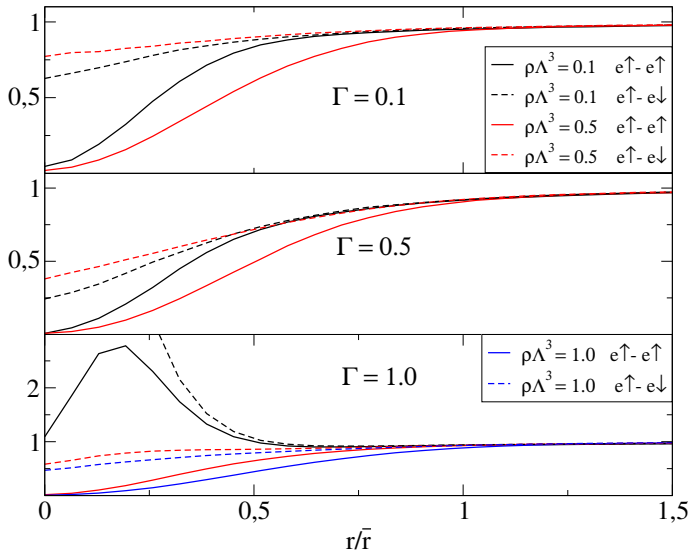

Figure 4.2: Electron-electron pair distribution functions for parallel and anti-parallel spins in a hydrogen plasma with the IKP for $\Gamma = 0.1$, 0.5 and 1.0 and degeneracy parameter $\rho\Lambda^3 = 0.1$, 0.5 and 1.0.

In Fig. 4.2 the pair distribution functions $g_{ee}(r)$ for H at coupling parameters $\Gamma = 0.1$, 0.5, 1.0 and degeneracy parameters $\rho_e\Lambda^3 = 0.1$, 0.5 and 1.0 are presented. As expected, the distribution functions of electrons with parallel spins at all densities and temperatures are below the corresponding distributions of electrons with anti-parallel spins and are equal to zero at $r = 0$, corresponding to zero probability of overlap in space. That arises from the Pauli principle and the divergence of the interaction potential (Eq. (4.9)) at $r = 0$. At the lowest coupling parameter $\Gamma = 0.1$ the electron subsystem almost looks like an ideal quantum electron gas – the pair distribution function averaged over spin

$$g_{ee}(r) = \frac{1}{2}\left[g_{ee}^{\downarrow\uparrow}(r) + g_{ee}^{\uparrow\uparrow}(r)\right] \tag{4.10}$$

at zero distance is very close to the low coupling limit of $g_{ee}(0) = 0.5$.

An increase of Γ leads to an increase of all e-e space correlation – the function $g_{ee}(r)$ gets a higher zero-distance value. As we see, all diffraction and spin effects play an important role only at a distance less then one mean electron-electron distance.

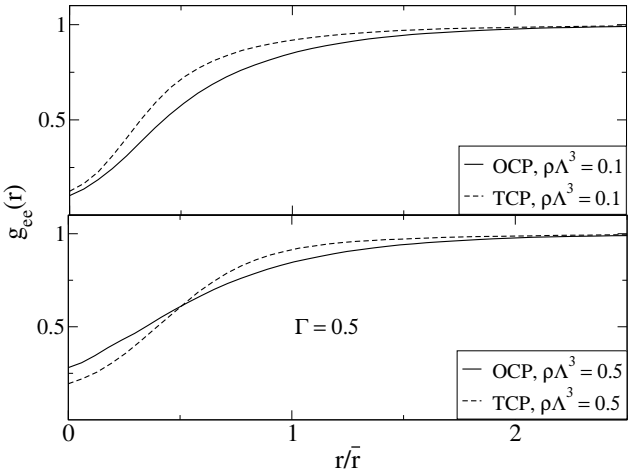

Figure 4.3: The electron-electron pair distribution functions for $\Gamma = 0.5$ and $\rho\Lambda^3 = 0.1, 0.5$, calculated with Kelbg potential in OCP and with IKP in the hydrogen TCP. The results for TCP are averaged over spin, Eq. (4.10).

A comparison of the result for $g_{ee}(0)$ of the OCP with the present simulations for $\Gamma = 0.5$ and $\rho_e\Lambda^3 = 0.1$, 0.5 gives a close agreement, especially at low degeneracy: 0.11 and 0.29 in the OCP (Fig. 4.3), 0.125 and 0.194 in the TCP. The differences are also come from the different kind of screening: in an OCP case it is a "static" screening of a opposite charge background, in the TCP case protons "dynamically" screen the electron-electron interactions. That is the reason of the long range tails in the OCP pair distribution functions. So we can conclude that the improved Kelbg potential reproduces the OCP behavior of the electron component in the limit of small and moderate coupling and small degeneracy. Since the two-component calculations with IKP are the more accurate than the OCP results we can conclude that differences arise from the dynamics of the second component.

A quite different situation we observe at stronger coupling Γ= 1.0. *Electron*

structure appears at $\rho\Lambda^3 = 0.1$ in form of a peak at the distance $r \approx 0.15\bar{r}$. Secondly, an increase of degeneracy leads to a sudden *decrease* of the range of the total electron-electron space correlation in contrast to the OCP. These significant differences are explained by the presence of protons and by the confinement of electrons into bound states. In the OCP, electrons can not form any complex structure except building a highly ordered lattice, as in Fig. 3.1. We will pay special attention to these questions in the following sections.

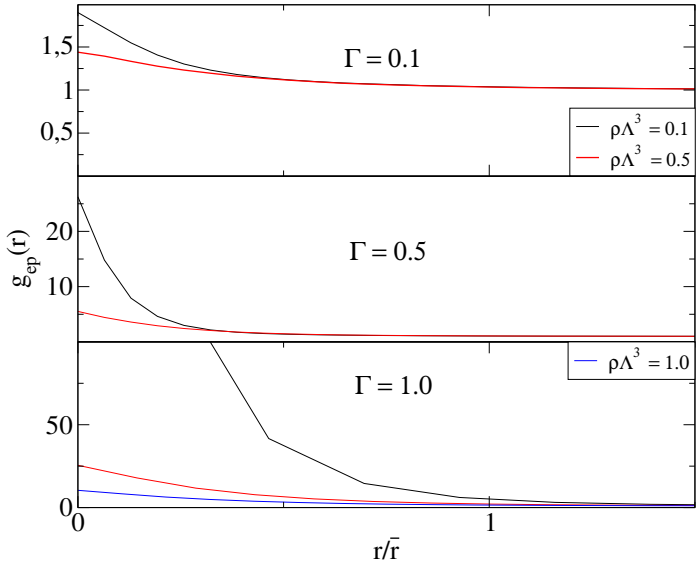

Figure 4.4: The same as in Fig. 4.2 for the electron-proton pair distribution function in the hydrogen plasma.

Let us now look at the proton-electron radial distribution. Fig. 4.4 presents the e-p distribution in the hydrogen plasma. In the whole simulated range we see a clear evidence of bound state formation – hydrogen atoms. As in the e-e case, with an increase of coupling the maximum of the distribution function in all cases becomes higher which indicates a larger fraction of hydrogen atoms in the plasma. Increasing the degeneracy leads at all coupling parameters to a higher ionization rate of hydrogen atoms. This process becomes especially substantial at $\Gamma = 1$, where at $\rho_e\Lambda^3$ =0.1 we observe a very steep growing of the maximum at $r = 0$. Such strong building of hydrogen atoms together with unrealistic e-e distribution at this condition, which was shown before, gives an evidence that at these densities or temperatures the improved Kelbg potential fails.

In corroboration of this conclusion we can look at the proton-proton distribution functions in the simulated plasma, plotted in Fig. 4.5. At $\Gamma = 0.1$, $g_{pp}(r)$ practically coincides for both investigated degeneracies. The degeneracy has only a small influence on the proton-proton distribution also at $\Gamma = 0.5$ and $\Gamma = 1.0$ with $\rho\Lambda^3 = 0.5$ and 1.0. But in the case of $\rho\Lambda^3 = 0.1$ protons form aggregates where the p-p distance is $r \simeq 1.5a_B$. From all three figures we can construct the following picture: at some conditions protons and electrons build many-particle aggregates, consisting of hydrogen atoms with proton-proton and electron-electron distance equal 1.5 and $2.17a_B$, respectively. Building of these clusters looks rather unphysically.

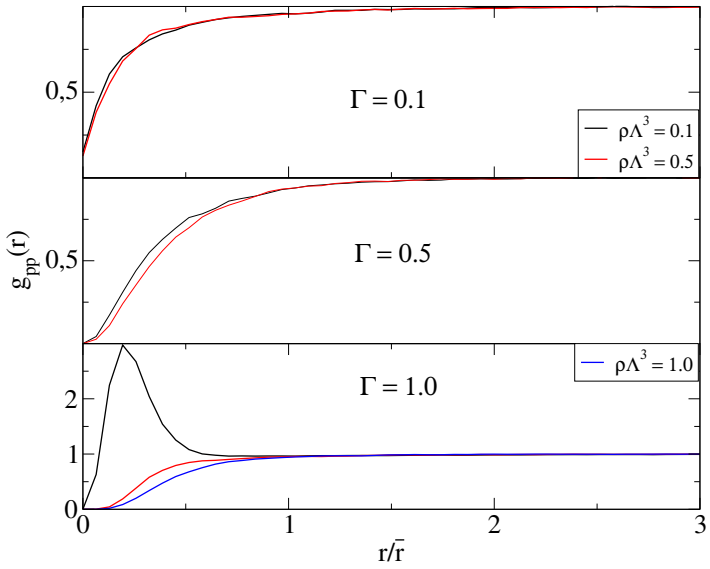

Figure 4.5: The same as in Fig. 4.2 for the proton-proton pair. In this units, the hydrogen Bohr radius corresponds to $a_B/\bar{r}$= 0.089 in the lower picture for $\Gamma = 1$ and $\rho\Lambda^3 = 0.1$.

To investigate the nature and reasons of this behavior of the improved Kelbg potential we have performed a series of simulations of the hydrogen plasma at two densities, corresponding to the Bruckner parameter $r_s = \bar{r}/a_B$ (a_B is Bohr radius) being equal to 4 and 6 and five different temperatures T =31250, 50 000, 62 500,125 000 and 166 670K. These parameter values correspond, respectively to $\Gamma = 2.53$, 1.58, 1.26, 0.63 and 0.47, for $r_s = 4$, and 1.68, 1.05 and 0.84, 0.42, 0.32, for $r_s = 6$. Numbers of particles were $N_p = 200$, $N_e^{\downarrow} = 100$ and $N_e^{\uparrow} = 100$. Other details were the same, as in the previous runs.

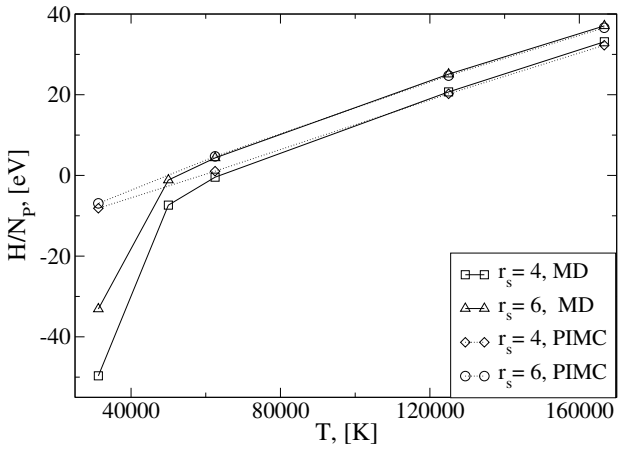

Figure 4.6: Internal energy per hydrogen atom (solid lines) at densities corresponding to $r_s = 4$ and 6 versus temperature. The results of restricted PIMC simulations [26] are shown for comparison (dotted lines). Symbols indicate the five temperatures for which the MD simulation has been performed. The pair approximation breaks down at around 50 000K, i.e. at the molecule binding energy.

In Fig. 4.6 we plot the internal energy per atom as a function of temperature for two densities and compare it to the Path Integral Monte Carlo results of Militzer [26]. One can note, that for high temperatures the energies from MD and PIMC simulations coincide very well and are within the limits of statistical errors. This is an important test for the simulation, and this agreement was expected due to the asymptotic character of the Kelbg potential as a rigorous weak coupling result. Moreover, we observe practically full agreement between MD and PIMC results down to a temperature of approximately 50 000K, corresponding to a coupling parameter $\Gamma \approx 1$. At this temperature of about 0.3 Ryd the plasma is dominated by atoms - a region completely unaccessible to the original Kelbg potential. This is a remarkable extension of 'semiclassical' molecular dynamics into the regime of moderate coupling, moderate degeneracy and partial ionization.

Naturally, below a critical temperature of about 50 000K the deviation from PIMC starts to grow rapidly – the MD results for the energy are becoming very low. It is very interesting to analyze the reason for this deviation, as this may suggest directions for future improvements. It turns out that the reason is not a failure of the used quantum pair potentials or the MD.

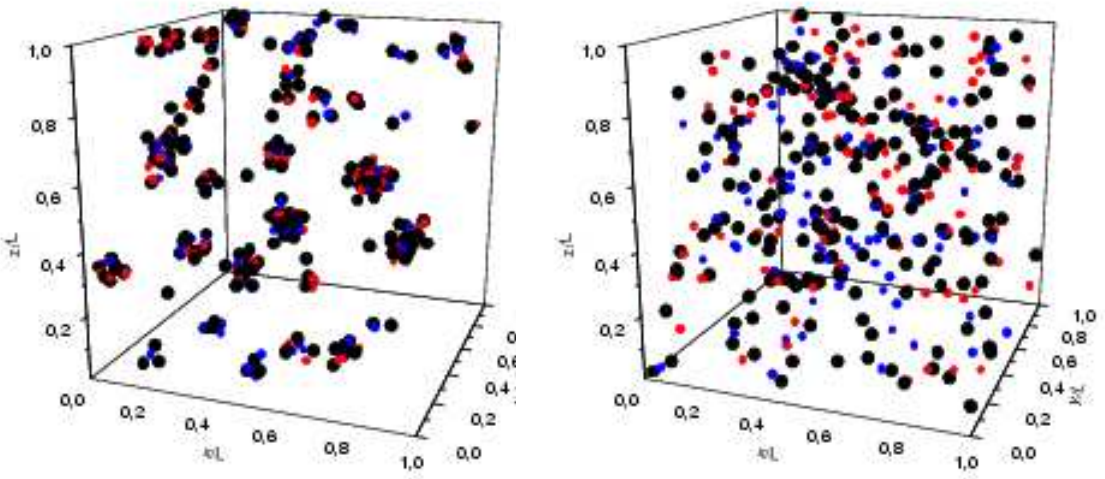

Figure 4.7: Snapshots of the simulation box in MD runs for a hydrogen plasma with $r_s = 4$ and T= 31 250K (left) and T= 62 500K(right). Protons are depicted as black points, electrons with spins up(down) are red(blue) points. The boxes are scaled in units of L for the given density.

To analyze this question we performed a careful inspection of the microscopic particle configuration in the simulation box. At high temperatures, the particle trajectories are those of a fully ionized classical plasma. At temperatures below one Ryd, we observe an increasing number of electrons undergoing strong deflection (large angle scattering) on protons and eventually performing quasi-bound trajectories, see Fig. 4.7, right picture. Most of these electrons remain "bound" only for a few classical orbits and then leave the proton again. Averaged over a long time our simulations are able to reveal the degree of ionization of the plasma. At the same time we observe occasional events of three or more particles being at a short distance for the duration of one or more orbits, reflecting the appearance of hydrogen molecules H_2, molecular ions H_2^+ etc.

If the temperature is lowered below approximately 50 000K (Fig. 4.7, left picture), we observe a strong increase of molecule formation and even a aggregation of many molecules into clusters with an interparticle distance close to one a_B. This turns out to be the reason for the observed very low energy of Fig. 4.6, because Coulomb interaction contributions are becoming dominant in the total energy. Of course, this behavior is not surprising: while all pair interaction pro-

cesses are modeled correctly even at low temperature (which is assured by the fit parameters in the improved Kelbg potentials), as soon as three or more particles are being close together, three particle and higher order correlations are becoming increasingly strong (they, in particular, account for the formation of the large bound state complexes described above).

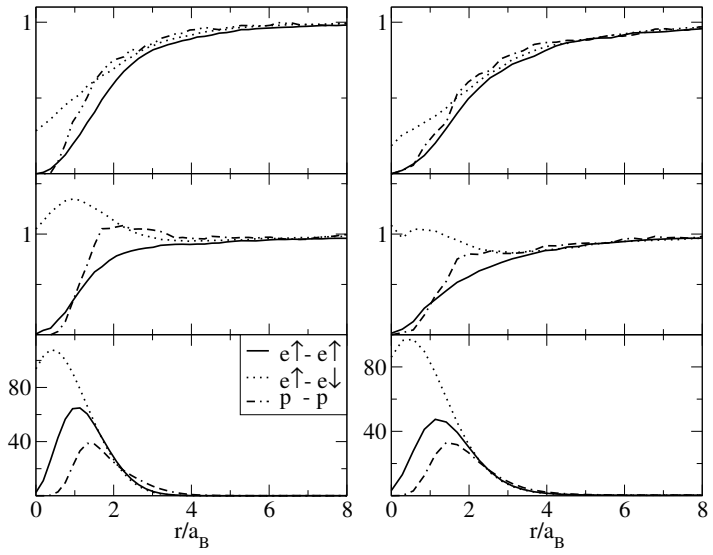

Figure 4.8: Electron-electron and proton-proton radial pair distribution functions for a correlated hydrogen plasma with $r_s = 4$ (left row) and $r_s = 6$ (right row) for $T = 125\ 000$, 61 250 , and 31 250 K (from top to bottom).

However, it was just the approximation used in the derivation of quantum potentials that three-particle and higher correlations can be neglected which was the basis for the use of a quantum potential in modeling the whole N-particle system. While MD includes any level of correlations, the use of the present potentials means that the *quantum corrections to the three-body (and higher order) interactions* are not adequately captured. Therefore, it is not surprising that this approximation breaks down at sufficiently low temperatures, and this break down occurs around the temperature corresponding to the binding energy of hydrogen molecules. From this we can conclude that molecule formation sets the limit of applicability of the present semiclassical MD simulations.

Let us now turn to a more detailed analysis of the spatial configuration of the particles in the MD simulations. In Fig. 4.8 the radial distribution functions between all particle species with the same charge are plotted at two densities.

Consider first the case of $T = 125000$ K (upper panels). For both densities, all functions agree qualitatively, showing the depletion at zero distance due to Coulomb repulsion. Besides, there are differences which arise from the spin properties. Electrons with the same spin show a "Coulomb hole" around $r = 0$. This hole is broader than the one of the protons, because the Pauli principle yields an additional repulsion of the electrons (this effect is much weaker for two protons due to their much smaller De Broglie wavelength). This trend is reversed at low temperatures, see the middle panel, which is due to the formation of hydrogen atoms and molecules. In this case, electrons (their trajectories) are "spread out" around the protons giving rise to an increased probability of close encounters of two electrons belonging to different atoms compared to two protons.

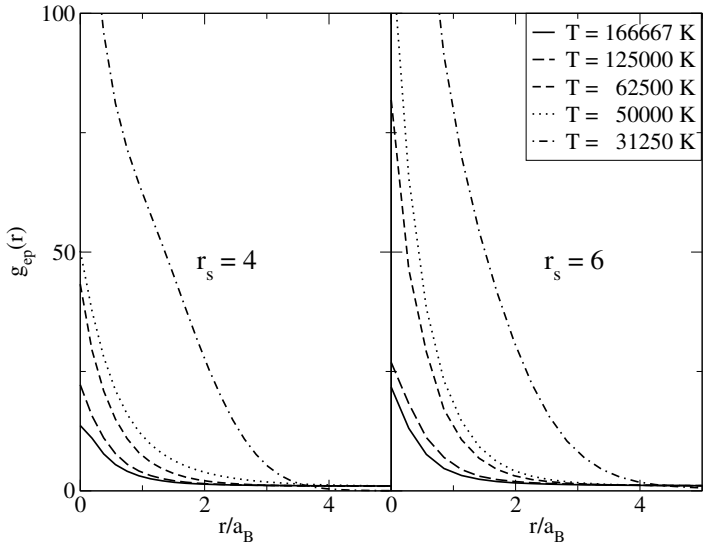

Figure 4.9: Electron-proton radial distribution functions at $r_s = 4$ (left figure) and $r_s = 6$ (right figure) and five temperatures, T =166 667, 125 000, 62 500, 50 000 and 31 250 K.

Now, let us compare electrons with parallel vs. electrons with anti-parallel spins. In all cases, we observe a significantly increased probability to find two electrons with opposite spin at small distances below one Bohr radius which is due to the missing Pauli repulsion in this case. This trend increases with lowering of the temperature due to increasing quantum effects and thus convincingly confirms that spin effects are correctly reproduced in our MD simulations.

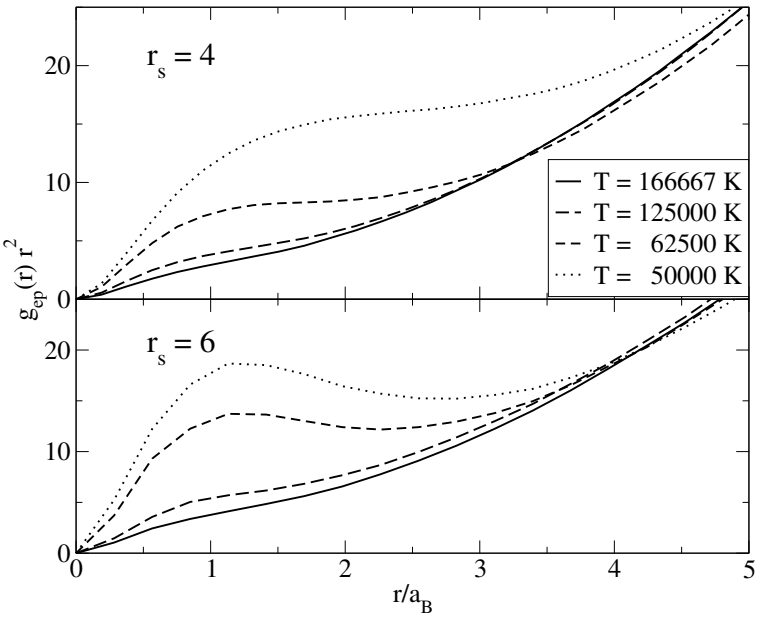

Figure 4.10: Electron-proton radial distribution functions multiplied by r^2. Same data as in Fig. 4.9.

Before analyzing the lowest temperature in Fig. 4.8 let us consider the electron-proton distributions which are shown in Fig. 4.9. With decreasing temperature, we observe a strong increase of the probability to find an electron close to a proton. In contrast to the classical case of collapse (see above), here the probability is finite. Multiplying these functions by r^2 gives essentially the radial probability which is plotted in Fig. 4.10. Here, lowering of the temperature leads towards the formation of a shoulder around $1.4a_B$ for $r_s = 4$ and $1.2a_B$ for $r_s = 6$ which is due to the formation of hydrogen atoms. This conclusion is confirmed by the corresponding quasi-bound electron trajectories as described above. At this temperature, the observed most probable electrons distance is slightly larger than one a_B as in the atom hydrogen ground state. There are two possible reasons. The first is many-body effect, i.e. the bound states are no isolated but influenced by the surrounding plasma. Secondly, the electrons have kinetic energy leading to a larger average radius of the classical quasi-closed orbits. Of course, the presented classical MD cannot yield quantization of the bound electron motion. But it correctly reproduces the statistical properties of the atoms.

Indeed, we can estimate the theoretical most probable electron-proton dis-

tance in a separated hydrogen atom at a given temperature from the partition function,

$$\left\langle r_{ep}^{P}\right\rangle (T)=\frac{1}{Z}\sum_{s}\left\langle r_{ep}^{s}\right\rangle g_{s}\exp(-E_{s}/kT), \tag{4.11}$$

where $\left\langle r_{ep}^{s}\right\rangle$ is the most probable e-p distance of the sth energy level and $Z=\sum_{s}g_{s}\exp(-E_{s}/kT)$ is the statistical sum over all electron states, g_s is the degeneracy factor of sth electron level. Formula (4.11) allow to estimate the temperature effect on the e-p distance. The most probable e-p distance for corresponding electron orbit $\left\langle r_{ep}^{s}\right\rangle$ can be found as a distance where the radial distribution function $r^2\psi_{rs}^2$ has a biggest maximum. Here the radial distribution function is related to the product obtained by multiplying the square of the radial wave function ψ_{rs} by r^2. By definition, it is independent of direction. If we take into account only the ground state and the first excited state (2s, 2p) with $\left\langle r_{ep}^{2s}\right\rangle = 5.237a_B$ and $\left\langle r_{ep}^{2p}\right\rangle = 4a_B$ then we obtain

$$\left\langle r_{ep}^{P}\right\rangle (T)\approx a_{B}\,\frac{1+(<r_{ep}^{2s}>+3<r_{ep}^{2p}>)\,\exp(\frac{-(E_{2s}-E_{1s})}{kT})}{1+(1+3)\,\exp(\frac{-(E_{2s}-E_{1s})}{kT})}. \tag{4.12}$$

Thus, if we take for n-energy levels $E_n=-\mathrm{Ryd}/n^2$ then we can calculate the most probable electron-proton distance in an isolated hydrogen atom. The results of calculation based on the Eq.(4.11) are shown in Fig. 4.11. We expect that at lower temperature the most probable radius would tend toward $1a_B$, but this temperature range is not realistically modeled due to molecule and cluster formation. For the temperatures $T=125\,000$, 62 500 and 50 000K we get $\left\langle r_{ep}^{P}\right\rangle =$ 1.796, 1.492 and $1.357a_B$, correspondingly. The last value is very close to simulation result $\left\langle r_{ep}^{P}\right\rangle_{sim} = 1.2\,a_B$, but is a little bit bigger than in the MD runs. Possible explanation is that "temperature" of the bounded electrons is lower than the average temperature of the whole plasma. From Fig. 4.11 we also observe, that if take into account the next excited electron level (3s, 3p and 3d orbitals) then we get much bigger e-p distances as we have in the MD simulation and in the calculation with the first level. In other words, hydrogen atoms in the simulation do not excite to such high levels but rather ionize into protons and free electrons.

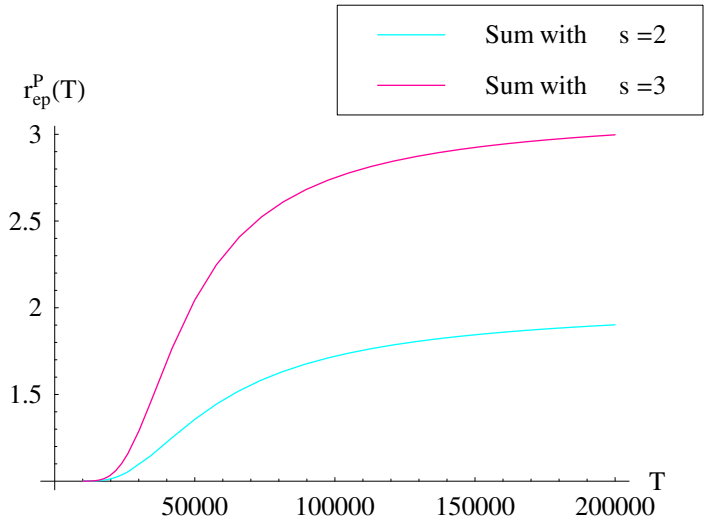

Figure 4.11: The most probable e-p distance depending on temperature. The partition function was calculated with first (s=2) and second (s=3) excited energy levels.

While the description of correlated complexes of more than two particles is certainly beyond the present pair approximation model, nevertheless, several features of partially ionized and partially dissociated hydrogen plasmas are reproduced correctly. At 62 500K and $r_s = 6$ (right center part of Fig. 4.8) the simulations show a first weak signature of molecule formation – see the maximum of the p-p distribution function around $r = 2a_B$ and the maximum of the distribution function of electrons with anti-parallel spins around $r = 1.5a_B$.

A further lowering of the temperature by a factor of two (lower panel of Fig. 4.8) confirms this trend: the p-p functions exhibit a clear peak very close to $r = 1.4a_B$ – the theoretical p-p separation in H_2 molecules. At the same time, also the e-e functions have a clear peak around $r = 0.5a_B$, in the case of opposite spins, and $r = 1.2a_B$, for parallel spin projections. The first case comes close to the true quantum mechanical H-H bound state (singlet) where the electron wave function is predominantly concentrated between two protons. On the other hand, no pronounced peak would be expected for electrons with the same spin, which is the origin of the formation of clusters of more than 2 atoms.

Nevertheless, we may conclude that even the formation and the spatial dimension of hydrogen molecules appear to be captured surprisingly well in these simulations. The main difficulty appears to arise not on the level of four parti-

cle correlations but on the level of six particle correlations: in the simulations nothing prevents two "bound" atoms from binding to a third and more atoms. The overall attractive Coulomb interaction makes it, below 50 000K, energetically favourable to form large clusters consisting of more than two atoms, explaining the strong decrease of the internal energy at $T = 31\ 250$K, cf Fig. 4.6. In reality, complexes of two molecules do exist, but they are very weakly bound due to subtle compensation effects arising from repulsive exchange interaction between the electrons which go far beyond the level of pair interaction.

Another advantage of the MD approach is that it captures many-body effects. In fact, at the parameters of Figs. 4.8-4.10 atoms and molecules are influenced by interaction with the plasma, in particularly screening effects leading to a reduction of the binding energy. Another manifestation of many body effects in Fig. 4.10 is that with increasing density (if r_s is reduced from 6 to 4) at constant temperature atoms vanish. This is caused by pressure ionization (Mott effect). There are two reasons for it: an increasing Coulomb screening and quantum effects. Here the quantum effects are dominated (Debye radius is approximately the same, but quantum parameter $\rho\Lambda^3 =$ 0.93 and 0.28 for r_s =4 and 6 at T =50 000K).

4.4.2 Dynamic properties of hydrogen plasma

4.4.2.1 Density-density correlations in hydrogen plasma

After having analyzed the parameter range of applicability of the improved Kelbg potential in MD simulations of the thermodynamic properties, we will extend the analyst to the dynamic properties of the hydrogen plasma. As was mentioned before, using semiclassical MD simulations gives the possibility of calculating different dynamic properties, diffusion processes, wave propagation, simulation of the response of the plasma to an electro-magnetic excitation, etc. In this section we investigate collective longitudinal modes of the ions and electrons in a hydrogen plasma. It is instructive to compare these results with those for the one component model results discussed in Chap. 3.

Analogously to the definition in Sec. 3.2.2,

$$\rho^{\alpha}(\mathbf{r}, t) = \sum_{i=1}^{N_\alpha} \delta[\mathbf{r} - \mathbf{r}_i^{\alpha}(t)] \tag{4.13}$$

is the time-dependent microscopic density of species α.

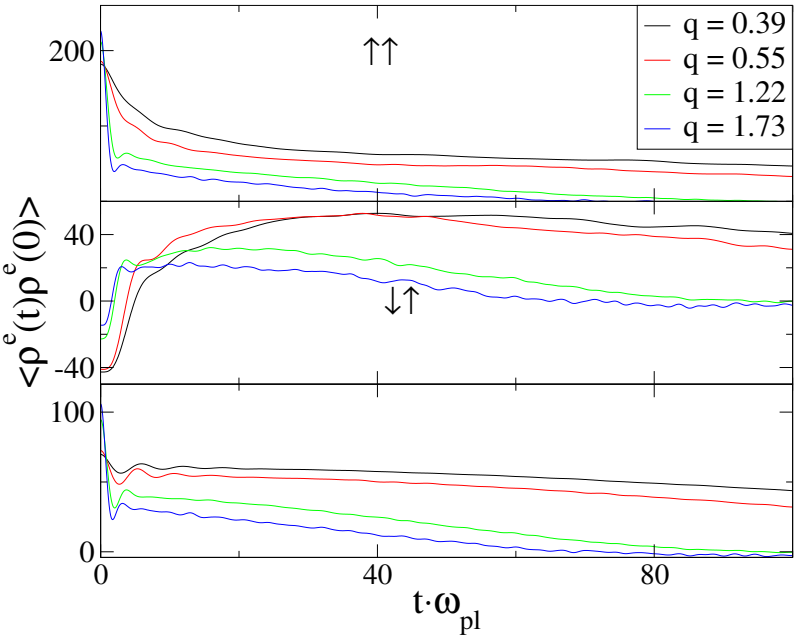

Figure 4.12: Electron density-density correlation functions for $\Gamma = 1$ and $\rho\Lambda^3 = 1$ for four wave vectors. The correlation functions are multiplied by $(N_e^{\uparrow} + N_e^{\downarrow})$. Upper figure: correlation functions for parallel spins, middle: for antiparallel spins, bottom figure: the density correlations averaged over spin.

The Fourier components of the density of species α are

$$\rho^{\alpha}(\mathbf{k}, t) = \sum_{i=1}^{N_\alpha} \exp[i \cdot \mathbf{k}\, \mathbf{r}_i^{\alpha}(t)]. \tag{4.14}$$

We now define the three partial density-density time correlation functions between sorts α and η as

$$A^{\alpha\eta}(\mathbf{k}, t) = \frac{1}{N_\alpha + N_\eta} \left\langle \rho^{\alpha}(\mathbf{k}, t) \rho^{\eta}(-\mathbf{k}, 0) \right\rangle . \tag{4.15}$$

In the case of spatial symmetry of the system the wave vector can be replaced by its length $\mathbf{k} = k$. Note also, that $A^{\alpha\eta}(k, t)$ and $A^{\eta\alpha}(k, t)$ are identical, for all pairs of α and η.

If we have two sorts of electrons (parallel and antiparallel spin) then the correlation function averaged over spin is

$$A^{e}(k, t) = A^{\uparrow\uparrow}(k, t) + A^{\downarrow\uparrow}(k, t). \tag{4.16}$$

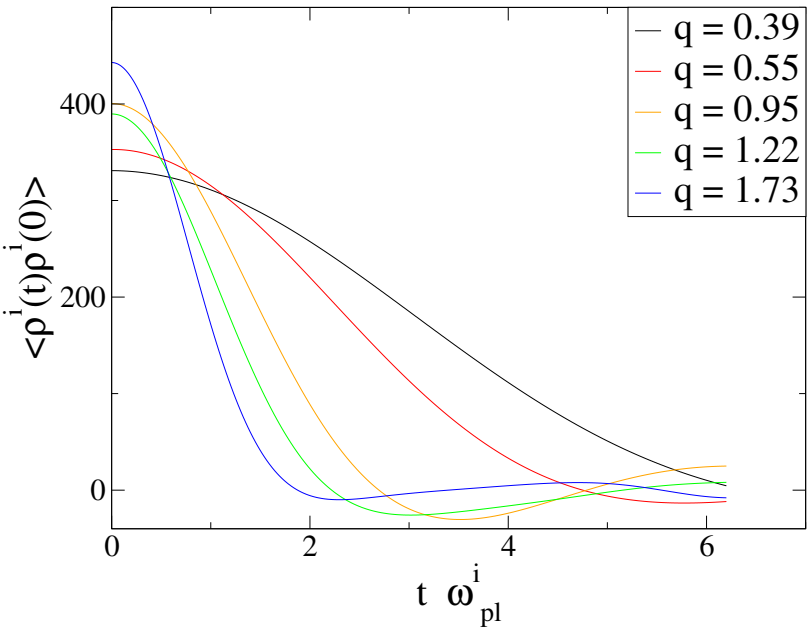

Figure 4.13: Proton density-density correlation functions for $\Gamma = 1$ and $\rho\Lambda^3 = 1$ for five wave vectors, including the smallest ($q = 0.39$) and the biggest ($q = 1.73$).

The electron density-density correlation functions for $\Gamma = 1$ and $\rho_e\Lambda^3 = 1$ are plotted in Fig. 4.12 for two smallest ($q = 0.39$, 0.55), an intermediate ($q = 1.22$) and the biggest wave vectors calculated in the simulation ($q = 1.73$), where the wave vector $q = k\bar{r}$ is given in units of the reciprocal mean inter-electron distance $1/\bar{r}$. As we see, comparing to the electron density correlation in the OCP simulation (Fig. 3.15), in the TCP simulation both correlation functions ($\uparrow\uparrow$ and $\downarrow\uparrow$) and the spin averaged correlation function $A^e(k,t)$ (Eq. (4.16), shown on bottom graph of Fig. 4.12) have two parts – a highly damped, high-frequency part and a weakly damped low-frequency correlation tail. The second part links to the slow ionic motion, and the first one, at frequencies of the electron plasma frequency ω_{pl} , is a clear manifestation of the much faster electronic motion. The time scale of ion motion which is determined by the ion plasma frequency $\omega^i_{pl} = \sqrt{4\pi\rho_i/m_i}$ is due to the big ion-to-electron mass ratio $M = m_i/m_e \simeq 1836$ is 43 times bigger than the electron plasma frequency ω_{pl}.

That can be observed on the proton density-density correlation functions, shown in Fig. 4.13. The bigger timescale of ionic motion causes a numerical limitation in the correlation function, compared to the electron density correlation function.

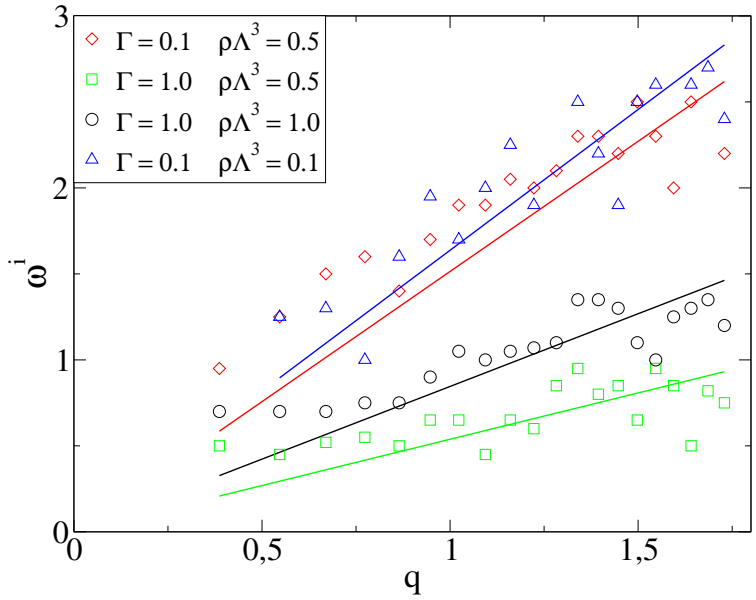

Figure 4.14: Ion-acoustic dispersion curves in hydrogen plasma in the range of wave vectors $q = 0.39..1.73$. Results for the case of weak coupling ($\Gamma = 0.1$) and small degeneracy ($\rho\Lambda^3 = 0.1,\ 0.5$), and strong coupling ($\Gamma = 1$) and high degeneracy ($\rho\Lambda^3 = 0.5,\ 1$) are shown. Also the linear fits are plotted. Frequency in unit of the ion plasma frequency ω_{pl}^i.

Although the timescale of the correlation functions are limited, we can suppose an approximate form of proton-proton density correlation function as a function $a\cos(bt)\exp(-ct)$, where a, b and c are fit parameters. Repeating the procedure determining of the peak of the structure factor of ions $S_{ii}(\omega,\ q)$ (definitions of the ion structure factors are following below, in Eq. (4.22)), as in the OCP case for electrons, we can obtain proton dispersion curves. Fig. 4.14 shows the dispersion of longitudinal ion collective modes. In contrast to electron plasma waves which are optical modes these waves are ion-acoustic waves due to the fact that the dispersion is similar to dispersion of usual sound oscillations with phase velocity

$$\omega = v_s\, q, \tag{4.17}$$

where

$$v_s = \sqrt{\frac{Z_i k_b T_e}{m_i}} \tag{4.18}$$

is the ion sound velocity, Z_i is the charge of ions.

There are two known analytical results for ion sound waves. For a strong non-

isothermal ($T_e \gg T_i$) two-component *ideal* and *nondegenerate* plasma in the limit of small wave vectors $q \ll 1$ spectrum of ion-acoustic oscillations are expressed as in Eq. (4.17) with ion sound velocity [96]:

$$v_s^n = \sqrt{Z_i \frac{k_B T_e}{m_i} \left(1 + \frac{3T_i}{Z_i T_e}\right)}. \tag{4.19}$$

For longitudinal oscillations in an *ideal* and *degenerate* plasma (electrons are degenerate, ions are classical) the spectrum are given by

$$\omega(q) = (1 + \frac{9}{(q\, r_D)^2}). \tag{4.20}$$

In our simulation coupling effects are included and we can expect that our results for the phase velocity will qualitatively agree with Eqs. (4.17-4.20) in the limit of small coupling and small degeneracy. Nevertheless, on Tab. 4.4, where the velocities of the ions sound waves from the MD runs are compared with the analytical approximation Eq. (4.18), we see some deviations.

Γ	$\rho\Lambda^3$	ω/q, [m/s]	v_s, [m/s]
0.1	0.1	$1.33{\cdot}10^5$	$1.52{\cdot}10^5$
0.1	0.5	$2.34{\cdot}10^5$	$2.61{\cdot}10^5$
1.0	0.5	$2.43{\cdot}10^4$	$2.61{\cdot}10^4$
1.0	1.0	$4.80{\cdot}10^4$	$3.29{\cdot}10^4$

Table 4.4: Comparison of phase velocity of ion waves ω/q from MD runs and from Eq. 4.17.

From the data of Fig. 4.14 we see that at small coupling parameters Γ electron degeneracy does not play big role on ion oscillations. On the other hand, at medium coupling ($\Gamma = 1$) and strong degeneracy ($\rho\Lambda^3 = 1$) theory prediction fails. Even an estimation of the velocity based on Eq. (4.20) for degenerate plasma gives a lower value of the velocity ($v_s = 2.34 \cdot 10^4$) than in the MD run.

Despite the different conditions the main results are clear: in the MD simulation the phase velocity of ion acoustic mode is smaller than in the theoretical prediction due to the direct treatment of *collision effects*. At high degeneracy a reason of the divergency of the ion sound velocity with the theoretical value is still not clear.

To investigate the spectrum of electron fluctuations we define the electron dynamic structure factor for the TCP $S_{ee}(k,t)$ in analogy to Sec. 3.2.2 for the OCP

$$S_{ee}(k,\omega) = \frac{1}{2\pi}\int_0^{+\infty} \exp(i\omega t) A^e(k,t) dt. \tag{4.21}$$

Analogous expressions hold for the electron-ion S_{ei} and the proton-proton S_{ii} structure factors. By linear combinations of the partial dynamic structure factors, charge and mass dynamic structure factors are defined [99]:

$$S_{ZZ}(k,\omega) = \frac{1}{2}\left[S_{ii}(k,\omega) - 2S_{ie}(k,\omega) + S_{ee}(k,\omega)\right], \tag{4.22}$$

$$S_{MM}(k,\omega) = \frac{1}{2}\left[M^2\, S_{ii}(k,\omega) + 2M\, S_{ie}(k,\omega) + S_{ee}(k,\omega)\right]. \tag{4.23}$$

As was mentioned by Hansen [99], in the high-frequency range $S_{ZZ}(k,\omega)$ is almost entirely determined by $S_{ee}(k,\omega)$ alone, the contributions from $S_{ii}(k,\omega)$ and $S_{ie}(k,\omega)$ have been practically disappeared (see Fig. 4.13). The main difference between $S_{ZZ}(k,\omega)$ and $S_{ee}(k,\omega)$ is the presence, in the latter, of a high-frequency peak which is considerably more pronounced than in the former. Thus, the spectrum of charge-density and mass-density fluctuations can be explored by the electron component.

Following the procedure of the determination of the plasmon frequency, described in details in Sec. 3.4, we have plotted plasma dispersion curves in the hydrogen TCP for coupling parameters $\Gamma = 0.1\ldots1.0$ and degeneracy parameter $\rho_e\Lambda^3 = 0.1\ldots1.0$. They are demonstrated in Fig. 4.15. The data points in the dispersion curves fluctuate more than in the OCP simulations and the dispersions are not very smooth. It comes from the fact, that in the TCP the damping of density oscillations at the same wave vector is higher than in an OCP(it will be discussed below). It means that peak on dynamics structure functions, which corresponds to plasmons becomes broader and not so pronounced. It leads to increasing uncertainty in the dispersion data. Also the damping gets stronger with decreasing the coupling parameter and simultaneously with increasing degeneracy of electrons. As the result, we have determined only a few points on the dispersion curve at smallest calculated wave vectors in the system with $\Gamma = 0.1$ and degeneracy $\rho\Lambda^3 = 0.5$.

As in the OCP for wave vectors up to value one reciprocal interparticle distance, the dispersion in the TCP in all cases is positive , $d\omega/dq > 0$. Clearly,

an increasing of coupling parameter Γ leads to a decrease of the dispersion slope, which means a decrease of the group velocity of the charge transfer (compare the dispersion curves for $\Gamma = 0.1$, 0.5 and 1.0 and one degeneracy parameter 0.5, Fig. 4.15). This can be easily explained – the higher the coupling parameter, the less free electrons are in the system, that leads to a lowering of the velocity of energy transfer in the plasma. Secondly, main differences between simulations with the same coupling parameter are observed for big wave vectors, as well as differences between the TCP and OCP dispersion curves. That is also clear - the improved Kelbg potential differs from the usual Kelbg potential only at small distances, (in units of the wave vector - on the big q), what we observe in the simulation results.

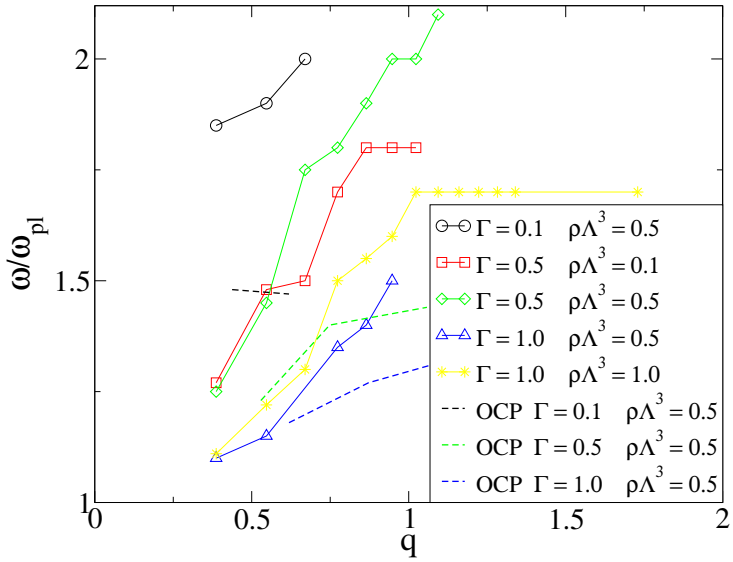

Figure 4.15: Plasma electron dispersion curves as measured from the position of the high-frequency peak in $S_{ee}(q,\omega)$ for $\Gamma = 0.1$, 0.5, 1.0 and degeneracy $\rho\Lambda^3 = 0.1$, 0.5, 1.0. Also, the results for the OCP are included.

Comparing with the OCP dispersion, in the TCP case we have not found a wave vector range where negative dispersion exists, $d\omega/dq < 0$. Moreover, we can conclude that the appearing of negative dispersion in the OCP dispersion curves is connected with limitations of the OCP model, namely an absence of ion motion. Indeed, in the TCP plasma a dependence of frequency on wave vector exists only for $k < 1/\bar{r}$, as we see in Fig. 4.15, for big wave vectors, finding plasmon dispersion is technically impossible. For big wave length $k > 1/\bar{r}$ there is no plasma wave propagation. For example, in the hydrogen plasma with $\Gamma = 1.0$

and degeneracy $\rho\Lambda^3 = 1.0$ for wave vectors $q > 1$ the phase velocity of density oscillation $d\omega/dq \approx 0$, that confirms our statement.

Direct inclusion of ion motion in the simulation affects also the value of damping of Langmuir waves, shown in Fig. 4.16. In the TCP model, electrons have additional collisions with ions which leads to additional increase of the damping. This can be seen, if we compare the damping of Langmuir waves for $\Gamma = 1.0$ from the OCP simulation and the damping in the hydrogen plasma simulation with the improved Kelbg potential. As in the OCP, a decrease of coupling parameter leads to a strong growing of damping.

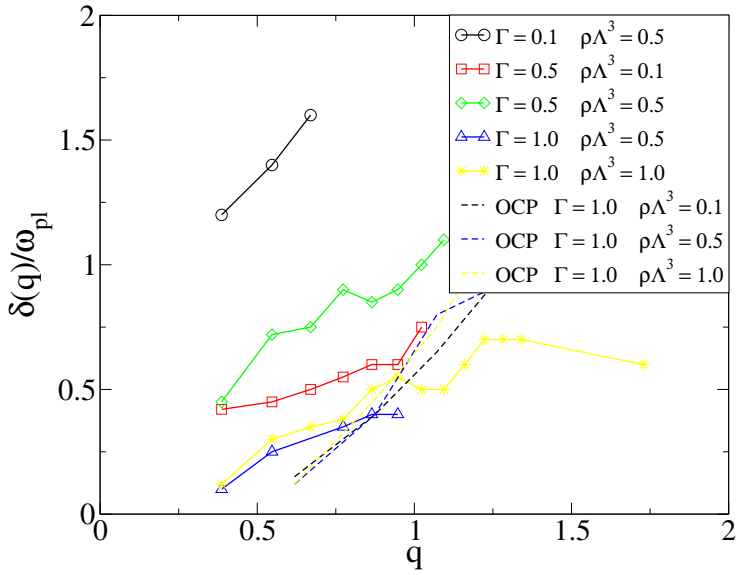

Figure 4.16: Damping of Langmuir waves in the hydrogen plasma from MD simulations with the improved Kelbg potential. Values of Γ and $\rho\Lambda^3$ are the same as in Fig. 4.15.

Another important observation is the dependence of the dispersion on degeneracy parameter, which was difficult to see in the OCP. In the present MD simulation, the damping of plasmon waves grows with increasing degeneracy parameter $\rho\Lambda^3$, but with increasing coupling this dependence becomes weaker (compare data for $\Gamma = 0.5$, $\rho\Lambda^3$ =0.1, 0.5 and $\Gamma = 1$, $\rho\Lambda^3$ =0.5, 1.0).

As we see, applying the improved Kelbg potential in the TCP hydrogen plasma gives us possibilities of a deeper investigation of equilibrium plasma oscillations, as we have demonstrated on the example of density-density correlation functions.

4.4.2.2 Spin density-density correlation functions

Using the improved Kelbg potential in MD simulations with two spin sorts of electrons opens a way to investigate a new kind of properties. As in the preceding section we can apply the mechanism of time correlation functions to electron *spin-spin density correlations.* We define the spin density Fourier component as

$$\rho^s(k,t) = \rho^{\uparrow}(k,t) - \rho^{\downarrow}(k,t), \tag{4.24}$$

and the electron spin correlation function

$$A_{ss}(k,t) = \frac{1}{N^{\uparrow} + N^{\downarrow}} \left\langle \rho^s(k,t)\rho^s(-k,0) \right\rangle . \tag{4.25}$$

Results for $A_{ss}(q,t)$ in the range of wave vectors from $q = 0.39...1.59$ are shown in Fig. 4.17 for the cases $\Gamma = 0.1$, 0.5, 1.0 and $\rho\Lambda^3 = 0.1$, 0.5, 1.0. Examination of spin density correlations reveals a general pattern. The maxima of short-time correlations are almost equal for all coupling parameters and degeneracies.

In case of the smallest coupling parameter $\Gamma = 0.1$, spin effects do not play an important role, they have a short-time character with a memory depth of about one plasma frequency ω_{pl}. Also the equilibrium spin density fluctuations in an almost ideal plasma have a weak dependence on wave vector (Fig. 4.17, top pictures). As the density correlation functions, the spin correlation functions are growing up with increasing coupling parameter for every wave vector. We note an interesting change of spin correlation in the $\Gamma - \rho\Lambda^3$ plane: at intermediate coupling an increase of degeneracy up to $\rho\Lambda^3 = 0.5$ leads to an increase of spin correlations, but in the strong coupling regime ($\Gamma = 1.0$) further increasing the degeneracy up to a value $\rho\Lambda^3 = 1.0$ leads to inverse behavior – spin correlations decay faster. In all cases, increasing of $\rho\Lambda^3$ enhances the oscillation of the spin correlation functions. As in the density-density correlation functions, the most considerable influence of wave vector on the spin density fluctuation we observe up to the wave vector $q = 1$.

It should be noted, finally, that our MD simulations, so far undertaken, do not consider spin-flip processes, as they would be expected in strong magnetic field. But our model should, in principle, be capable to describe related phenomena as well.

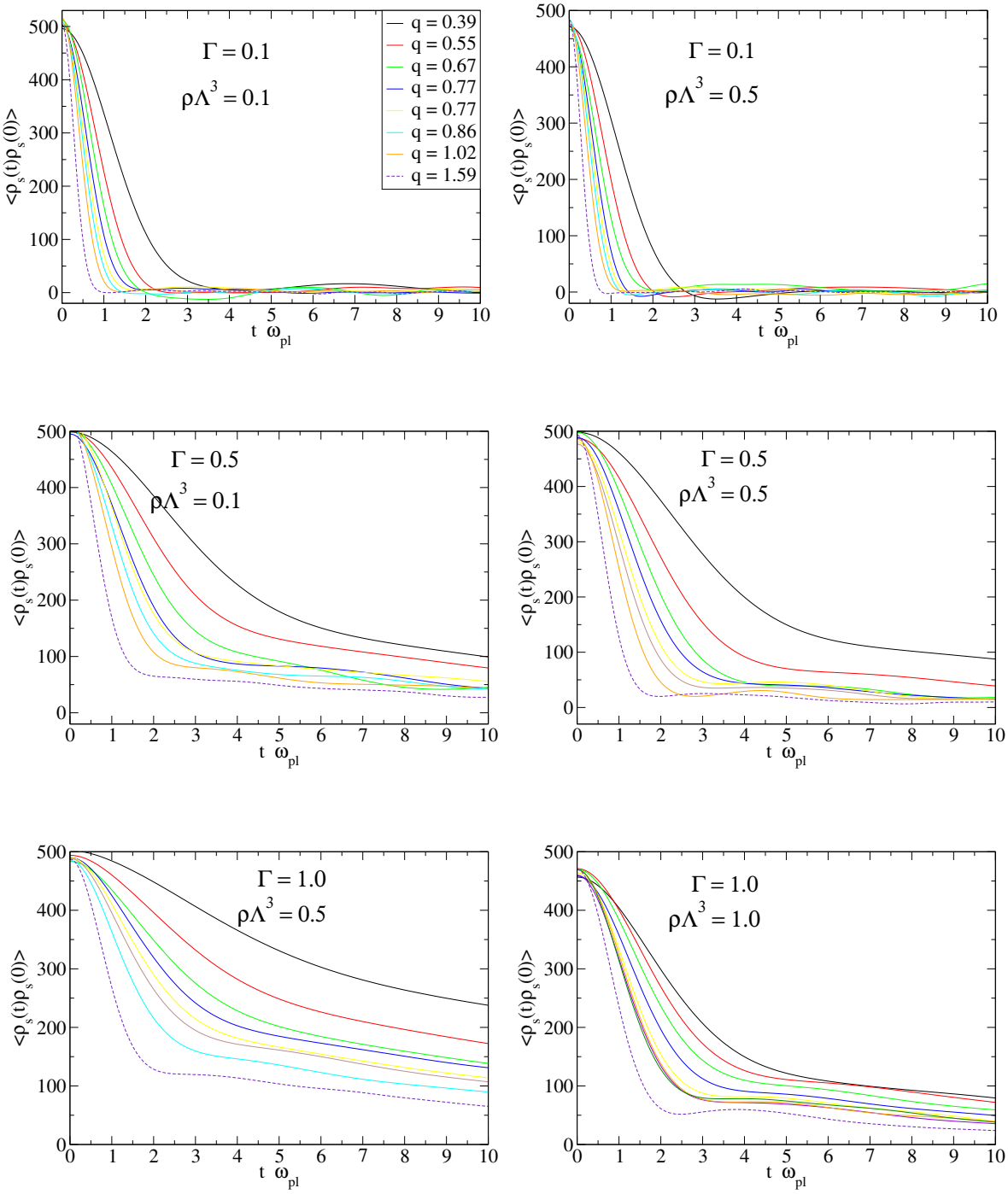

Figure 4.17: Electron spin-spin density correlation functions for different Γ and $\rho\Lambda^3$, multiplied by N_e. The wave numbers, shown on the top left figure are the same in all pictures.

4.4.3 Spin properties of the plasma ground state

Another important question, which is closely related to the subject of our investigation are magnetic property of the ground state of the electron gas. It has have been the subject of theoretical [100, 101], experimental [108] and numerical works [102–106]. Traditionally, it is expected that the electron gas can be either a paramagnetic or ferromagnetic ground state, depending on the electron density ρ_e. In a paramagnetic ground state the spin polarization $\zeta = (\rho^{\uparrow} - \rho^{\downarrow})/\rho_e$ is equal to zero, in ferromagnetic case this value varies from small (low spin polarization) to one (full polarization). Overhauser [101] showed that in the Hartree-Fock (HF) approximation the energy per electron of the ferromagnetic state is lower than in the paramagnetic state when $\rho_e < 9.7 \cdot 10^{21} cm^{-3}$. So, a high-density electron gas would be in a paramagnetic ground state and a low-density one would be ferromagnetic. But, even at relatively high density the paramagnetic state is unstable with respect to formation of spin-density waves, which were considered before. Such instability may cause partially polarized states in plasma with lifetimes which are determined by the values of spin-spin correlations.

Moreover, the HF approach is based on some limitations: it is a mean field theory, it does not include interparticle correlations. These correlations have been included in other approaches. But different improvements of the HF approach lead to the different results. Capella *et al.* [107] have take into account electron-electron correlations in the electron system for a range of densities $r_s = 1...100$ and did not find an evidence for transition of a 3D electron gas into an antiferromagnetic state. They have employed the approximation schemes with the simple Tomas-Fermi screening, the static RPA and RPA including local-field corrections in the Hubbard and Gold forms. Within any of the schemes there was not sign of antiferromagnetism in the entire investigated density interval.

Using Variational and fixed-node Green's-function Monte Carlo calculations was shown [102] that two-dimensional electron gas has the paramagnetic (unpolarized) ground state till Wigner crystallization. This calculation predict a Wigner crystallization at the density $r_s \approx 37 \pm 5$. This GFMC calculation does not predict a transition to the ferromagnetic state.

Simulation with the classical-map hypernetted-chain (CHNC) method performed by different authors [103–105] for 2D and 3D electron system indicated, that the paramagnetic phase stays to be the ground state until the Wigner crys-

tallization density as in the VMC and GFMC calculations, even though the energy separation with ferromagnetic and other partially polarized states become minute.

The ferromagnetic ground state of a dilute, three-dimensional electron gas has not been reported experimentally. Despite most predictions there are evidences that a stable polarized phase exists, for example in electron doped calcium hexaboride CaB_6 [108]. Recent calculation by Ortiz *et al.* [106] treating partially spin-polarized states of the low-density electron gas, in fact, found evidence that near $r_s = 30$ the stable state is one the ferromagnetic polarization of the order of 10%. However, this results most likely is specific for that materials.

Based on the mentioned recent studies a possible picture is the following: the ground state of electron system depends on density. In the high-density limit it is a paramagnetic, a stable ferromagnetic phase may exists near Wigner crystallization.

The range of our MD simulations lies at density region above $r_s = 1$ and at finite temperature much, higher than that of a ground state. In our simulations the polarization is an input parameter and does not change in time. While the simulations show indications of spin density waves, see Fig. 4.17, they are strongly damped. Finally, these are two-component plasma simulations which may be very different from an electron gas. Nevertheless, the presented methods should allow for a qualitative analysis of spin-density waves in dense hydrogen, if the particle number and simulation time are substantially increased.

Chapter 5

Conclusions

In this work, we have applied classical and semiclassical Molecular Dynamics simulations to strongly correlated mesoscopic and macroscopic Coulomb systems, respectively. Our goal was to show how this numerical method can be used to investigate different kinds of nonideal charged particle systems.

In chapter 2 we have started from a relatively simple mesoscopic 2D classical model of charged particles in a parabolic confinement potential. Using MD simulations we have investigated structural changes during the heating of small clusters, on the example of a magic cluster with $N = 19$. It was shown, that phase diagram of the small classical clusters can be divided into three regions: completely ordered solid like phase, a phase with the partial (only radial) order and disordered phase. In the first one, the cluster is like a crystal, in second one the cluster shows intershell rotation (radial melting). If the temperature goes above some critical temperature shells begin to exchange their particles and the shell structure of the cluster starts to disappear.

Using classical MD simulations we have investigated the dynamics of intershell rotation. The value of the intershell barrier for the cluster with $N = 19$ was obtained and compared with data from PIMC simulations using the response of the mesoscopic 2D cluster to an external excitation.

Using the difference of values of the intershell angular barrier in the clusters with $N = 19$ and $N = 20$, a new scheme of a single-electron device with controlled current of the outer shell was suggested. The results of the simulation can be used to realize for example a micro-device where the angular mobility ("conductivity") can be turned on and off .

In chapter 3 we have performed series of MD simulations of one-component plasmas (OCP) to investigate the influence of interparticle potentials, coupling parameter and degeneracy on the static and dynamic properties. We have concluded that increasing of coupling and degeneracy has a similar effect on the plasmon frequency – it leads to a shift of plasmon frequency to smaller values.

An important part of our research was the comparison of the MD simulation results with theoretical predictions for the dynamic structure factor, dispersion relation and damping of Langmuir waves in the OCP.

We developed a new effective two-body quantum potential – (improved Kelbg potential (IKP)) extending the work of Kelbg and others. In our approach to dense, strongly correlated hydrogen plasma we applied the IKP in MD simulations and described bound states, ionization and dissociation processes in the region of moderate coupling. We carefully analyzed these effects and found that the region of applicability of the improved Kelbg potential is limited to temperatures above the molecule binding energy, for hydrogen, $T \geq 50\,000\mathrm{K}$. Applying the IKP below this temperature leads to an unphysical formation of big hydrogen clusters. Further theoretical improvements will be needed to correctly describe the process of molecule formation in hydrogen.

Furthermore in chapter 4 we extended the Molecular Dynamics method with the IKP to investigate dynamic effects in two-component hydrogen plasma (TCP). The direct inclusion of the ions motion affects the dispersion of plasmon waves. In comparison to the OCP model, in the TCP we did not see a plasmon oscillations for wave vectors which exceed one inverse mean interparticle distance. The existence of such dispersion in the OCP model seems to be an artefact of the model.

One of the advantages of the new potential is the direct inclusion of spin effects in the simulation. As a first application to the hydrogen plasma, we could show an influence of the coupling parameter and the degeneracy on electron spin density fluctuations even in the equilibrium plasma without an external magnetic field. In the future work, the present methods can be directly used to investigate spin-flip processes, spin ordering and spin density wave dispersion in correlated partially ionized plasma.

5.1 Zusammenfassung

In der vorliegenden Arbeit werden stark korrelierte, mesoskopische und makroskopische Coulomb-Systeme mit Methoden der klassischen und semiklassischen Molekular-Dynamik (MD) untersucht. Zielstellung war die Anwendung dieser nummerischen Methoden, um verschiedene Arten von nicht idealen Systemen geladener Teilchen zu beschreiben.

Im Kapitel 2 wird von einem einfachen, mesoskopischen, klassischen 2D-Modell geladener Teilchen in einem parabolischen Fallenpotential ausgegangen. Für den magische Cluster mit $N = 19$ Elektonen wurden die strukturellen Änderungen während des Aufheizprozessees mit MD-Simulationen untersucht. Dabei wurde herausgestellt, dass das Phasendiagramm in kleinen klassischen Clustern in drei Bereich untergeteilt werden kann: eine vollständig geordnete Phase, eine Phase mit einer partiellen (nur radialen) Ordnung und eine ungeordnete Phase. In der ersten Phase zeigt der Cluster kristallartiges Verhalten, in der zweiten eine gegelaufige Rotation der Schalen (radiales Schmelzen). Übersteigt die Temperatur einen kritischen Wert, ist ein Teilchenaustausch zwischen den Schalen verbunden mit einer Auflösung der Schalenstrucktur zu beobachten.

Mit der Hilfe der klassischen MD-Simulationen wird die Dynamik der Inter-schalen-Rotation untersucht. Die Größe der Inter-Schalen-Barriere für Cluster mit $N = 19$ wurde aus der Reaktion des mesoskopischen 2D-Clusters auf äußere Anregung bestimmt und mit Daten aus Monte Carlo Simulationen verglichen.

Auf Basis der Differenz der Inter-Schalen-Winkelbarrieren wurde bei den Clustern mit $N = 19$ und $N = 20$ ein neues Schema eines Einzelelektron-Bauelementes mit regelbarem Strom auf der äußeren Schale vorgeschlagen. Die Ergebnisse der Untersuchungen können angewendet werden, um beispielweise hochintegrierte Bauelemente zu verwirklichen, bei denen die "Winkel-Beweglichkeit" (Leitfähigkeit) ein und ausgeschaltet werden können.

Im Kapitel 3 wird eine Reihe von Einkomponenten-Plasmen (EKP) mittels MD-Simulationen untersucht, um den Einfluss des Wechselwirkungpotentials, des Kopplungsparameter und der Entartung auf die statischen und dynamischen Eigenschaften zu bestimmen. Dabei wurde gefunden, dass eine Erhöhung der Kopplung und Entartung eine ähnliche Erwirkung auf die Plasmonfrequenz haben. Sie führen zu einer Frequenzverschiebung in Richtung kleineren Werte.

Ein wichtiger Bestandteil der vorliegender Arbei ist der Vergleich der numeri-

schen Resultate mit den theoretischen Vorhersagen für den dynamischen Strukturfaktor, der Dispersion und Dämpfung von Langmuir Schwingungen in EKP.

Darüber hinaus wurde eine neues effektives Zweiteilchen-Quantenpotential (ein verbessertes Kelbg-Potential (VKP)) eingeführt, das die Arbeit von Kelbg u.a fortsetzt. In unseren Näherungen zum dichten, stark korrelierten Wasserstoffplasma haben wir das VKP in MD- Simulationen angewendet und die gebundenen Zustände, Ionisation- und Dissoziationprozesse im Bereichen schwacher Kopplung beschrieben. Des Weiteren wurden diese Effekte systematisch analysiert und gezeigt, dass der Anwendbarkeitsbereich des verbesserten Kelbg-Potentials auf Temperaturen über der molekularen Bildungsenergie von Wasserstoff $T \geq 50\,000K$, beschränkt ist. Wenn das VKP unter dieser Temperatur verwendet wird, dann führt dies zu der unphysikalischen Formation großer Wasserstoff-Cluster. Um den Prozess der Molekularformation in Wasserstoff korrekt beschreiben zu können, sind jedoch noch weitere theoretische Verbesserungen notwendig.

Weiterhin wird im 4. Kapitel die MD-Methode mit dem VKP erweitert, um die dynamischen Effekte im Zwei-Komponenten-Plasma (ZKP) zu beschreiben. Die direkte Berücksichtigung von Ionbewegungen beeinflusst die Dispersion von Plasmonwellen. Im Vergleich zum EKP-Modell haben wir im ZKP keine Plasmonwellen für Wellevektoren, die größer als der umgekehrte Zwischenteilchenabstand sind, beobachtet. Die Existenz solcher Dispersion in den EKP scheint jedoch ein Artefakt des Modells zu sein.

Einer der Vorteile dieses neuen Potentials ist die unmittelbare Berücksichtigung von Spineffekten in molekulardynamischen Simulationen. Bei der ersten Anwendung zum Wasserstoffplasma konnten wir den Einfluss des Kopplungparameters und die Entartung auf Elektron-Spin-Dichte-Fluktuationen sogar bei den Gleichgewichtsplasmen ohne externes Magnetfeld zeigen. In künftigen Arbeiten kann des entwickelte Verfahren in Untersuchungen zur Spin-Umkehrprozessen, Spinordnung und Spin-Dichte-Wellendispersion in korreliertem, teilweise ionisierten Plasma direkt angewendet werden.

Bibliography

[1] M. Wolverton, Winged atom, in *American History Magazine*, February 2003

[2] W.W. Wood. Early history of computer simulation in statistical mechanics. In G. Ciccotti and W.G. Hoover (editors), *Molecular Dynamics Simulations in Statistical Mechanics Systems*, North Holland (1986)

[3] N. Metropolis, A.W. Rosenbluth, M.N. Rosenbluth, A. N. Teller, and E. Teller, Equation of state calculations by fast computing machines, *J. Chem. Phys.*, **21**, p. 1087-92 (1953)

[4] B.J. Alder and T.E. Wainwright. *J. Chem. Phys.*, **27**, 1208 (1957)

[5] B.J. Alder and T.E. Wainwright. *J. Chem. Phys.*, **31**, 459 (1959)

[6] W.W. Wood and F.R. Parker, *J. Chem. Phys.*, **27**, 720 (1957)

[7] A. Rahman, Correlations in the Motion of Atoms in Liquid Argon, *Phys. Rev.* **316**, A405 (1964)

[8] F.H. Stillinger and A. Rahman, *J. Chem. Phys.* **60**, 1545 (1974)

[9] M.P. Allen and D.J. Tildisley. *Computer simulation of liquids*, Clarendon, Oxford (1987)

[10] K. Binder, and G. Ciccotti, editors, *Monte Carlo and Molecular Dynamics of Condensed Matter Systems,* Italian Physical Society, Bologna (1996)

[11] D.C. Rapaport, *The Art of Molecular Dynamics Simulation*, Cambridge University Press, New York (1995)

[12] D.F. Frenkel, B. Smith, *Understanding Molecular Simulation : from algorithm to application*, Academic Press, San Diego (1996)

[13] J. Barnes, L. Hernquist, Computer models of colliding galaxies, *Physics Today*, March, 54-61 (1993)

[14] L. Hernquist and C. Mihos, Excitation of activity in galaxies by minor merges, *Astrophysics. J.*, **448**, 41-63 (1995)

[15] B. Dünweg, G.S. Grest, and K. Kremer, Molecular dynamics simulations of polymer systems, *Numerical Methods for Polymeric Systems,* editor S. G. Whittington, Springer-Verlag, 159 (1998)

[16] A.K. Adya, O.N. Kalugin, M.N. Volobuev, Y.V. Kolesnik, Microscopic structure of liquid dimethyl sulphoxide and its electrolyte solutions: molecular dynamics simulations, *Mol. Phys.,* **99**, 10, 835-54 (2001)

[17] A.D. MacKerell, Jr.B. Brooks, C.L. Brooks, L. Nilsson, B. Roux, Y. Won, and M. Karplus, CHARMM: The Energy Function and Its Parameterization with an Overview of the Program, in *The Encyclopedia of Computational Chemistry*, P.v.R. Schleyer et al., editors, John Wiley & Sons: Chichester, 271-277 (1998).

[18] B.J. Berne. *"Statistical Mechanics"*, Plenum Press, New York and London (1977)

[19] H. Feldmeier, *Nucl. Phys.* A **515,** 147-172 (1990)

[20] D. Klakow, C. Toepffer, and P.G. Reinhard, *J. Chem. Phys.* **101**, 10766 (1994)

[21] M. Knaup, Die Methode der Wellenpakets-Molekulardynamik (WPMD) mit Anwendungen auf Wasserstoff, PhD thesis, Erlangen (2002)

[22] R. Car, and M. Parrinello, The unified approach for molecular dynamics and density functional theory. In *Simple Molecular Systems and Very High Density,* edited by A. Polian, P. Loubeyre, and N. Boccarra, New York, Plenium Press (1988)

[23] O. Pfaffenzeller, *Hydrogen and Hydrogen-Helium Mixtures under High Pressure. A Density Functional and Molecular Dynamics Study*, PhD thesis, Aachen (1996)

[24] V. Filinov, P. Thomas, I. Vagra, T. Meier, M. Bonitz, V. Fortov, and S.W. Koch, Interacting electrons in a one-dimensional random array of scatterers: A quantum dynamics and Monte Carlo study, *Phys. Rev. B* **65**, 165124 (2002)

[25] D.M. Ceperley, and B.J. Alder, Ground state of solid hydrogen at high pressures, *Phys. Rev B*, **36** 2092-2106 (1987)

[26] B. Militzer, *Path Integral Monte Carlo simulations of hot dense hydrogen*, PhD thesis, University of Illinois (2000)

[27] G. Kelbg, Quantenstatistik der Gase mit Coulomb-Wechselwirkung, *Ann. Physik*, **12**, 354-60 (1964)

[28] W.D. Kraeft, D. Kremp, W. Ebeling, and G. Röpke, *"Quantum statistic of charged particle systems"*, Akademie-Verlag Berlin (1986)

[29] A.V. Filinov, M. Bonitz, and W. Ebeling, Improved Kelbg potential for correlated Coulomb systems, *J. Phys. A*, **36**, 22, 5957-62 (2003)

[30] V.S. Filinov, *J.Mol. Phys.* **88** , 1517 (1996)

[31] P.E. Toschek, in *New Trends in Atomic Physics*, edited by G. Gryndberg and R. Stora, Vol. I, p. 383, North-Holland, Amsterdam (1984)

[32] B.G. Lewi, Phys. Today **41**, 17, (1988); G. Birkl, S. Kassner, and H. Walther, *Europhys. News* **23**, 143 (1992)

[33] C.C. Grimes, G. Adams, Evidence for a liquid-to-crystal phase transition in a classical two-dimensional sheet of electrons. *Phys. Rev. Lett.* **42**, 795-798 (1979)

[34] P. Leiderer, W. Ebner, and V.B. Shikin, *Surf. Sci.* **113**, 405 (1987)

[35] M.A. Reed, and W.P. Kirk, *"Nanostructure Physics and Fabrication"*, Academic press, Boston (1989)

[36] A.V. Filinov, P. Ludvig, V. Golubnychyi, M. Bonitz, and Yu.E. Lozovik, Equilibrium and dynamical properties of few particles systems in bilayers, *phys. stat. sol. (c),* **5**, p. 1518-22 (2003)

[37] R.C. Ashoori, Electrons and artificial atoms, *Nature*, **379**, 413 (1996), N.B. Zhitenev et al., Periodic and aperiodic bunching in the addition spectra of quantum dots, *Phys. Rev. Lett* **79**, 2309 (1997)

[38] M. Bonitz, V. Golubnychiy, A.V. Filinov, and Yu.E. Lozovik, Single-electron control of Wigner crystallization, *Microelectronic Engineering,* **63**, 141-145 (2002)

[39] R. Egger, W. Häusler, C. H. Mak, and H. Grabert, Crossover from Fermi Liquid to Wigner Molecule Behavior in Quantum Dots, *Phys. Rev. Lett.* **82**, 3320 (1999)

[40] A.V. Filinov, M. Bonitz, and Yu.E. Lozovik, Wigner Crystallization in Mesoscopic 2D Electron Systems, *Phys. Rev. Lett.* **86**, 3851 (2001)

[41] V.M. Bedanov, and F.M. Peeters, Ordering and phase transition of charged particles in a classical finite two-dimensional system, *Phys. Rev. B,* **49**, 2667-2676 (1993)

[42] Yu.E. Lozovik, *Usp. Fiz. Nauk* **153**, 356 (1987)

[43] Yu.E. Lozovik, and L.M. Pomirchiy, *Phys Status Solidi B* **161**, K11 (1990)

[44] V.A. Schweigert, and F.M. Peeters, Spectral properties of a classical two-dimensional clusters, *Phys. Rev. B,* **51**, 7700 (1995)

[45] J.P. Schiffer, Melting of Crystalline Confined Plasmas, *Phys. Rev. Lett.* **88**, 205003 (2002)

[46] M. Klindworth, A. Melzer, A. Piel, and V.A. Schweigert, Laser-excited intershell rotation of finite Coulomb clusters in a dusty plasma, *Phys. Rev. B* **61**, 8404-10 (1999)

[47] A. Filinov, PhD thesis, Moscow state Institute of Physics and Technology (2001)

[48] V. Golubnychiy, P. Ludwig, A.V. Filinov, and M. Bonitz, Controlling intershell rotations in mesoscopic electron clusters, accepted for publication in *Superlattices and Microstructures,* (2004)

[49] V. Golubnychiy, A. Filinov, and M. Bonitz, Intershell rotation barriers of mesoscopic 2D Coulomb clusters, in *Progress in Nonequilibrium Green's Functions II*, edited by M. Bonitz and D. Semkat, World Scientific, Singapore, p.338-46, (2003)

[50] L. Verlet, 'Computer experiment' on Classical Fluids, I. Thermodynamical Properties of Lennard-Jones Molecules, *Phys. Rev.* **159**, 98 (1967)

[51] J.M. Haile, *Molecular dynamics simulation: elementary methods*, Wiley-interscience publication, Clemson (1992)

[52] Minghui Kong, B. Partoens, and F.M. Peeters, Transition between ground state and metastable states in classical two-dimensional atoms, *Phys. Rev. E* **65**, 046602 (2002)

[53] A. Melzer, M. Klindworth, and A. Piel, Normal Mode of 2D Finite Clusters in Complex Plasmas, *Phys. Rev. Lett.* **87**, 12 (2001)

[54] Yu.E. Lozovik, and A.M. Popov, Orientational melting of two-shell carbon nanoparticles: molecular dynamics study, *Chem. Phys. Lett.* **328**, 355-362 (2000)

[55] A. Melzer, Mode spectra of thermally excited 2D finite Coulomb clusters, *AIP Conf. Proc.*, 649(1), 180 (2002)

[56] Sh.G. Amiranashvili, N.G. Gusein-zade, and V.N. Tsytovich, Spectral properties of small dusty clusters, *Phys. Rev. E* **64**, 016407 (2001)

[57] I.V. Schweigert, V.A. Schweigert, and F.M. Peeters, Radial-Fluctuation-Induced stabilization of the ordered state in two-dimensional classic clusters, *Phys. Rev. Lett.* **84** (19), 4381-4384, (1999)

[58] J. Baker, and A. G. Rojo, Coulomb drag between one dimensional wigner crystal rings, *J. Phys. C,* **13,** 5313 (2001)

[59] W.F. van Gunsteren, and H.J.C. Berendsen, Algorithms for brownian dynamics, *Mol. Phys.* **45**, 637-647 (1981)

[60] W.C. Swope, H.C. Andersen, P.H. Berens, and K.R. Wilson, *J. Chem. Phys.* **76**, 637 (1982)

[61] M. Bonitz, D. Semkat, A. Filinov, V. Golubnychiy, D. Kremp, D. O. Gericke, M. S. Murillo, V. Filinov, V. Fortov, W. Hoyer, and S.W. Koch, Theory and simulation of strong correlations in quantum Coulomb systems, *J. Phys. A.* **63**, 6, 5921-30 (2003)

[62] M. Bonitz, *Quantum Kinetic Theory*, Teubner, Stuttgart-Leipzig (1998)

[63] M. Bonitz, V. Golubnichiy, N.H. Kwong, D. Semkat, D. Kremp, V. S. Filinov, and M. Schlanges, Dielectric properties of correlated quantum plasmas, *Contrib. Plasma Phys.* **41**, 2-3, 155-158 (2001)

[64] J.P. Hansen, Statistical Mechanics of Dense Ionized Matter. I. Equilibrium Properties of the Classical One-Component Plasma, *Phys. Rev.* A **8**, 3096 (1973)

[65] J.M. Caillol, D. Levesque, J.J. Weis, and J.P. Hansen, *J. Stat. Phys* **28**, 325 (1982)

[66] J. Ortner, F. Schautz, and W. Ebeling, Quasiclassical molecular-dynamics simulations of the electron gas: Dynamic properties, *Phys. Rev.* E **56**, 4665 (1997)

[67] R.K. Moudgil, P.K. Ahluwalia, and K. Tankeshwar, Dynamic structure factor of a two-dimensional electron gas, *Phys. Rev.* B **54**, 8809 (1996)

[68] W. Schülke, K. Höppner, and A. Kaprolat, *Phys. Rev.* B **54**, 17464 (1996)

[69] S.G. Brush, H.L. Sahlin, and E. Teller, *J. Chem. Phys.* **45**, 2102 (1966)

[70] W.L. Slattery, G.D. Doolen, and H.E. DeWitt, N dependence in the classical one-component plasma Monte Carlo calculations, *Phys. Rev.* A **26**, 2255 (1982)

[71] S. Ogata, S. Ichimaru, Critical examination of N dependence in the Monte Carlo calculations for a classical one-component plasma, *Phys. Rev.* A **36**, 5451 (1987)

[72] R.T. Farouki, and S. Hamaguchi, Thermal energy of the crystalline one-component plasma from dynamical simulations, *Phys. Rev.* E **47**, 4330 (1993)

[73] S. Ichimaru, "Statistical Plasma Physics" Vol.**II**, Addison-Wesley Publishing Company, 1994; G.S. Stringfellow, H.E. DeWitt, and W.L. Slattery, *Phys. Rev.* A **41**, 1105 (1990)

[74] M.D. Jones, and D.M. Ceperley, Crystallization of the One-Component Plasma at Finite Temperature, *Phys. Rev. Lett.* **76**, 4572 (1996)

[75] Yu.L. Klimontovich, *"Statisticheskaya fizika"*, Nauka, Moskov (1982)

[76] A. Filinov, Yu. Lozovik, and M. Bonitz, *phys. stat. sol.* (b) **221**, 231 (2000)

[77] D. Pines, and Ph. Nozieres, *The Theory of Quantum Liquids*, Benjamin, New York (1966)

[78] G.D. Mahan, *Many-Particle Physics*, Plenum Press, New York/ London (1990)

[79] W.D. Kraeft, D. Kremp, W. Ebeling, and G. Röpke, *Quantum Statistics of Charged Particle Systems*, Plenum, London, New York (1986)

[80] M. Bonitz et al., *J. Phys.* B: Condensed Matter **8**, 6057 (1996)

[81] Nai-Hang Kwong, and M. Bonitz, Real-Time Kadanoff-Baym Approach to Plasma Oscillations in a Correlated Electron Gas , *Phys. Rev. Lett.* **84**, 1768 (2000)

[82] J.P. Hansen, and I.R. McDonald, *Theory of simple liquids*, Academic Press, London (1976)

[83] D. Klakow, C. Toepffer, and P.-G. Reinhard, *Phys. Lett.* A **192**, 55 (1994); V.S. Filinov, *J. Mol. Phys.* **88**, 1517, 1529 (1996)

[84] G. Kelbg, *Ann. Physik* (Leipzig) **12**, 219 (1963); **14**, 394 (1964)

[85] G. Zwicknagel, PhD thesis, University of Erlangen (1994)

[86] M. Bonitz et al., *Contrib. Plasma Phys.* **41**, 155 (2001)

[87] V.S. Filinov, M. Bonitz, and V.E. Fortov, *JETP Letters* **72**, 245 (2000)

[88] V.S. Filinov, V.E. Fortov, M. Bonitz, and D. Kremp, *Phys. Lett.* A **274**, 228 (2000)

[89] W. Ebeling, H.J. Hoffmann, and G. Kelbg, *Contr. Plasma Phys.* **7**, 233 (1967)

[90] B.R.A. Nijboer, and F.W. De Wette, *Physica* **XXIII**, 309 (1957)

[91] M.J.L. Sangster, and M. Dixon, Advances in Physics **25**, 247 (1976)

[92] C. Deutsch, *Phys. Lett.* A **60**, 317 (1977)

[93] J.P. Hansen, I.R. McDonald, and E.L. Pollock, Statistical mechanics of dense ionized matter. III. Dynamical properties of the classical one-component plasma, *Phys. Rev.* A **11**, 1025 (1975)

[94] A.A. Kugler, *J. Stat. Phys.* **8**, 107 (1973)

[95] M. Bonitz, J.-F. Lampin, F.-X. Camescasse, and A.F. Alexandrou, Nonequilibrium plasmons in optically excited semiconductors, *Phys. Rev.* B **62**, 15724 (2000)

[96] A.F. Aleksandrov, L.S. Bogdankievich, A.A. Rukhadze, *Principles of Plasma Electrodynamics*, Springer (1984)

[97] H. Wagenknecht, W. Ebeling, and A. Förster, *Contrib. Plasma Phys.* **41**, 15 (2001)

[98] A.V. Filinov, V.O. Golubnychiy, M. Bonitz, W. Ebeling, and J.W. Dufty, Improved quantum potentials for correlated Coulomb systems, subm. to *Phys. Rev.* E, (2004)

[99] J.P. Hansen, and I.R. McDonald, Microscopic simulation of a strongly coupled hydrogen plasma, *Phys. Rev.* A **23**, 2041-59 (1981)

[100] A.W. Overhauser, Giant Spin Density Waves, *Phys. Rev. Lett.* **4**, 9 (1960)

[101] A.W. Overhauser, Spin Density Waves in an Electron Gas, *Phys. Rev.* **128**, 3 (1962)

[102] B. Tanatar, and D.M. Ceperley, Ground state of the two-dimensional electron gas, *Phys. Rev.* B **39**, 5005 (1988)

[103] F. Perrot, and M.W.C. Dharma-wardana, Spin-polarized electron liquid at arbitrary temperatures: Exchange-correlation energies, electron-distribution functions, and the static response functions, *Phys. Rev.* B **62**, 16536 (2000)

[104] F. Perrot, and M.W.C. Dharma-wardana, 2D Electron Gas at Arbitrary Spin Polarizations and Coupling Strengths: Exchange-Correlation Energies, Distribution Functions, and Spin-Polarized Phases, *Phys. Rev. Lett.* **87**, 206404 (2001)

[105] C. Bulutay, and B. Tanatar, Spin-dependent analysis of two-dimensional electron liquids, *Phys. Rev.* B **6**5, 195116 (2002)

[106] G. Ortiz, M. Harris, and P. Ballone, subm. to *Phys. Rev. Lett.* arXiv:cond-mat/9810126 v1 (2003)

[107] K. Capelle, and L.N. Oliveira, Search for antiferromagnetism in homogeneous electron systems, *Eur. Phys. J.* B, **12**, 225-234 (1999)

[108] D.P. Young, D. Hall, M.E. Torelli, Z. Fisk, J.L. Sarrao, J.D. Thomson, H.-R. Ottt, S.B. Oseroff, R.G. Goodrich, and R. Zysler, High-temperature weak ferromagnetism in a low-density free-electrons gas, *Nature*, **397**, 412-14 (1999)

Acknowledgments

Prof. Dr. Michael Bonitz is gratefully acknowledged for his professional support on all phases of this project. During numerous discussions, he lead my work toward optimal results and initiated me in the research world of complex plasmas grace to his perfectionist style. This work were never finished without his patience and stimulation of me in the research.

I want to bring special thanks to Prof. Dr. Dietrich Kremp and Prof. Dr. Manfred Schlanges for their useful scientific discussions concerning different and not always evident aspects of plasma physics.

Dr. Valery Bezkrovniy is gratefully acknowledged for fruitful discussions and his always friendly support during my stay in Rostock. But most of all I thank him for his friendship.

I am very thankful to Dr. Oleg Kalugin from Kharkov who helped me in a "chemical" part and gave me a possibility to start a "physics" part of my scientific carrier.

Our perfect secretary Ms. Renata Nareyka is gratefully acknowledged for helping me in the jungle of bureaucratic problems that I had to deal with during all my stay in Germany. Her advises in a friendly way saved a lot of my time and efforts, which I could spend on this research.

My colleagues and friends from the plasma group: Prof. Dr. W. Kreaft, Dr. T. Bornath, Dr. D. Semkat, Prof. Dr. V.S. Filinov and Dr. A.V. Filinov are specially acknowledged for their help and fruit discussions. Patrick Ludwig for his friendly help in managing various programming problems in Mathematica. My special thanks to Albert Zhykhar who showed me a professional way in many aspects of programming. Alan Prouty is acknowledged for editing of english grammatic in the part of the thesis.

The author acknowledges the financial support of this project by Deutsche Forschunggemeinschaft under grant numbers BO-1366/2, 12001393, 12001356, Sonderforschungsbereich under grant number 12001385 and the Rostock linux cluster FERMION.

Finally I want to hearty thank my parents, Maria and Olexiy Golubnyhichiy and my brother Olexiy who have been always the fundamental support, even though, sometimes from far away...